Physik Department

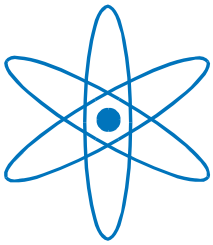

From single molecules to biological interfaces with atomic force microscopy

Dissertation

von

Sandra Kienle

Technische Universität München

TECHNISCHE UNIVERSITÄT MÜNCHEN

Physik-Department

Lehrstuhl für Biophysik E22a

und

Zentralinstitut für Medizintechnik

From single molecules to biological interfaces with atomic force microscopy

Sandra Petra Kienle

Vollständiger Abdruck der von der Fakultät für Physik der Technischen Universität München zur Erlangung des akademischen Grades eines

Doktors der Naturwissenschaften (Dr. rer. nat.)

genehmigten Dissertation.

Vorsitzender: Univ.-Prof. Dr. M. Zacharias

Prüfer der Dissertation:

1. Univ.-Prof. Dr. Th. Hugel
2. Priv.-Doz. Dr. R.H.H. Burgkart

Die Dissertation wurde am 18.02.2014 bei der Technischen Universität München eingereicht und durch die Fakultät für Physik am 31.03.2014 angenommen.

Table of contents

Summary

Current advances in medicine and technology contribute to a continuous aging of the worldwide population. Unfortunately this is accompanied by a more frequent occurrence of age-related diseases. Examples are degenerative ones like Alzheimer's disease or Osteoarthritis. While Alzheimer's disease is caused by misfolding of proteins, Osteoarthritis is associated with a failure of lubrication provided by cartilage. Detailed knowledge about the early pathology as well as an effective therapy, not to mention a cure, are however still missing. The last treatment option for Osteoarthritis for example is a total joint replacement. However until now it was not possible to build an artificial structure with the same astonishing frictional and wear resistant properties as articular cartilage. Additionally, joint implants can lead to various problems due to unwanted adhesion of proteins to the surface. This so called biofouling is attempted to be reduced by coating the implant's surface.

The development of novel methods for detection and treatment of these diseases can be supported by understanding the associated molecular mechanisms behind protein folding, healthy cartilage tissue and also effective polymer coatings. Here atomic force microscopy (AFM) is used to realize experiments with single polymers and additional microscopic friction force microscopy to gather new insights into the underlying molecular mechanisms of these complex processes.

Temperature dependent single polymer desorption experiments are performed with the atomic force microscope and compared to molecular dynamics simulations to delineate the role of hydrophobic attraction in protein folding. Only a weak temperature dependence of the desorption force and free energy is observed. This disagrees with the known free energy dependence of proteins and of small hydrophobic particles, which were previously used as a model system for studying the temperature dependent hydrophobic attraction. Consequently, the desorption of a single polymer from a surface is more complicated than the solvation of small hydrophobic particles and still not sufficient to understand the main driving forces in protein folding. Nevertheless temperature dependent single polymer desorption experiments can be used to study processes dominated by the hydrophobic attraction which means that protein folding can not only be driven by the hydrophobic attraction.

Furthermore, AFM-based adhesion and friction experiments with single polymers with and without side chains of different architectures are analyzed in view of their potential use in surface coatings (Figure 1). For the unspecific interaction of mobile polymers with a surface no effect of side chain architecture is observed whereas for immobile polymers the contact area as well as intra-chain interactions alter the interaction strength. Measurements with polymers containing highly branched side chains do not lead to higher interaction forces than linear chains, as the contact area could even be reduced due to the high branching density. This needs to be kept in mind when designing polymers for surface coatings.
A step towards a better understanding of the underlying molecular mechanisms in biological systems are adhesion and friction experiments with single polymers on articular cartilage. They point towards an enhanced interaction compared to solid surfaces presumably due to

interactions with polymers present on the cartilage surface like for example the formation of entanglements.

The last part of this work focuses on the microscopic lubrication properties of articular cartilage. The friction force is measured with the atomic force microscope in the boundary lubrication regime and also with a tribometer during lubrication facilitated by the interstitial fluid pressurization in the migrating contact regime. A viscosupplement which is used for the treatment of Osteoarthritis is not proven to be more favorable for lubrication than a physiological sodium chloride solution. However, the wear resistance is likely altered. Measurements at extreme conditions after de- and rehydration of articular cartilage in solutions with different salt concentrations allow to gain further insight into the molecular mechanism of cartilage lubrication and reveal a surprisingly small effect on the friction coefficient although the cartilage surface does change.
Neither a different wear protection due to a viscosupplement nor an altered appearance of the network after rehydration are visible in the frictional properties of articular cartilage. Therefore, low friction cannot directly be related to a high wear resistance and a healthy tissue.

In summary, a combination of experiments with single polymers and microscopic lubrication measurements has been utilized to gain insight into the molecular mechanism of adhesion and friction on both synthetic and biological surfaces.

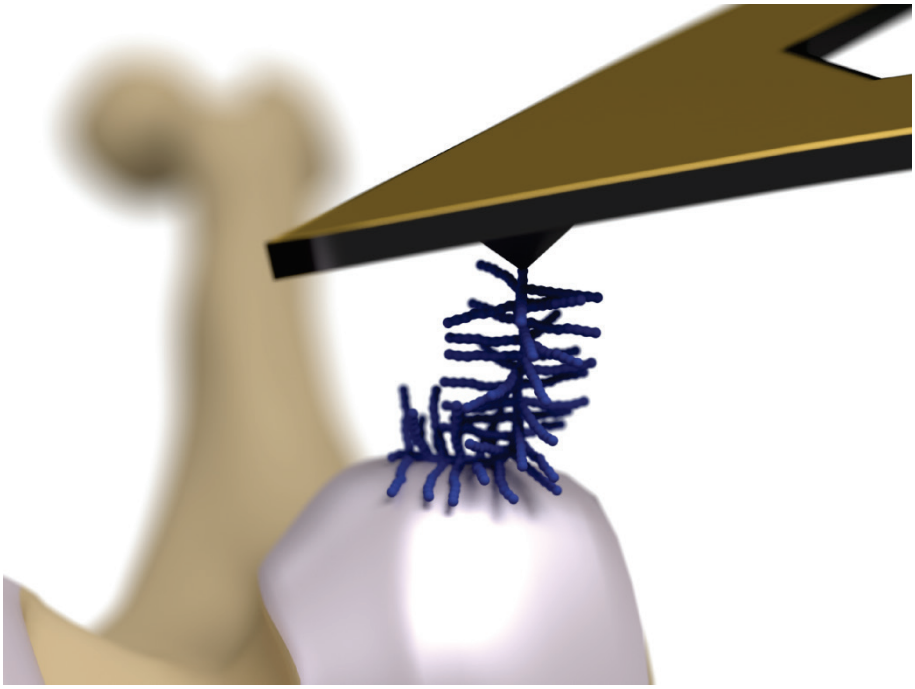

Figure 1. Scheme of a single polymer desorption experiment on top of the cartilage surface of a knee joint.

1. Introduction

The continuously aging population is a worldwide phenomenon as the life expectancy has increased drastically within the last decades. Where in 1900 the life expectancy in the United States was 49 years, it increased to 78 years already in 2007 and is going to increase even further. This is an increase of 29 years in only 107 years [1]. This drastic improvement is attributed mostly to the containment of infectious diseases due to better hygiene and the discovery of antibiotics [2].

A higher life expectancy, however, is not always an advantage as age-related diseases occur more frequently [3]. Examples are degenerative ones like Alzheimer's disease, osteoarthritis and also cardiovascular diseases. Alzheimer's disease is the most common form of dementia. A lot of research is focused on indentifying the early pathology, establishing a therapy or even finding a cure. Symptoms start with memory lapses, are followed by long-term memory loss, mood swings and lead eventually to loss of body functions and death. The cause of Alzheimer's disease, but also of other degenerative diseases is believed to emanate from the misfolding of proteins [3]. Over years, more and more mutations in the amino acid structure occur and proteins do not follow the right pathway during folding. An accumulation of these misfolded proteins can then lead to the onset of the disease. But what forces cause proteins to fold and how do they actually fold?
Osteoarthritis is another very common disease and is associated with cartilage tissue losing the ability to protect against damage and wear [4]. Symptoms are joint pain or constricted movement of the joints. Osteoarthritis can be induced by injuries of the knee joint or wear of the cartilage, but also a genetic cause is possible. Here again knowledge about the early pathology as well as an effective therapy is missing. If osteoarthritis is too advanced then the last treatment option is a total joint replacement. However until now it was not possible to artificially recreate the astonishing frictional and wear resistant properties of articular cartilage. This means that even joint replacements are not a long term solution. Thus the question is: How can cartilage provide such a low friction and at the same time such a high wear resistance?
With implants additional problems arise due to the unwanted adhesion of proteins to the surface. This bio-fouling causes for example the formation of blood clots. But how can the performance of implant coatings be enhanced?

To solve these questions, it is first of all important to understand the underlying molecular mechanisms of protein folding, surface coatings and joint lubrication. In this thesis an approach based on atomic force microscopy (AFM) is applied to conduct experiments with single polymers, but also microscopic friction force microscopy to gain insight into the molecular mechanism of these complex processes.

The thesis is arranged as follows. First, the fundamental principles of intermolecular forces, adhesion and single polymer desorption experiments are explained. Afterwards, friction and lubrication in general and for articular cartilage in particular are summarized. Then the materials and methods used in the experiments are described, before the results are presented:

In chapter 4 the role of hydrophobic attraction in protein folding is determined. It is generally accepted that hydrophobic amino acids cluster together and form a hydrophobic core which is only marginally exposed to the solvent. A lot of work focused on understanding the temperature dependence of protein folding and therefore of this hydrophobic attraction. Often small hydrophobic particles were chosen to experimentally and theoretically describe the temperature dependent hydrophobic attraction, because simulations with complex proteins are not yet possible. In this thesis a combination of atomic force microscopy-based measurements and molecular dynamics simulations was used to gain insight into the desorption force and the free energy change during the desorption of single polymers from solid surfaces at different temperatures and therefore into the hydrophobic attraction. These results were then compared to the free energy change during protein folding and also to the solvation of small hydrophobic particles and lead to the conclusion that small hydrophobic particles are not sufficient to investigate protein folding, but neither is the desorption of single polymers.
Furthermore, in chapter 5 synthetic and naturally occurring single polymers with and without side chains of different architectures were compared in both single polymer desorption and friction experiments to draw conclusions on polymer architecture for coatings. It was found that both, the contact area as well as intra-chain interactions in the polymer bundle are important for enhanced adhesion to a surface.
Not only changing the temperature or using naturally occurring polymers with a more complex architecture allows to take a step towards a better understanding of biological systems, but also changing the surface from a solid to a biological one. Therefore, single molecule experiments were performed on articular cartilage and presented in chapter 6. They point towards enhanced adhesion during both vertical and lateral pulling compared to non-biological surfaces.
The last chapters focus on understanding the microscopic lubrication of articular cartilage by atomic force microscopy-based and tribometer-based friction force microscopy. Here, the lubrication properties of a sodium chloride solution are compared to a viscosupplement which is widely used for the treatment of osteoarthritis. Together with measurements of salt dependence and de- and rehydration of cartilage, this leads to the conclusion that low friction is not always associated with an intact tissue and a high wear resistance.

2. Fundamental principles

2.1. Intermolecular forces

Measuring forces on the single molecule level and on the microscale involves various intermolecular forces. These forces are shortly described in the following. A more detailed description can be found in [5].

2.1.1. Covalent bonds

In covalent bonds, an atom shares its electrons with two or more neighboring atoms whereby the number of possible bonds is defined by the valency. The most important properties of covalent bonds are a strong directionality with well-defined angles and rotational freedom (for single bonds). Covalent bonds are rather short ranged (0.1-0.2nm) and rather strong ($100k_BT$, k_B: Boltzmann constant, T: temperature) [5].

All other bonds described in the following are physical bonds. They do not have a comparable directionality to covalent bonds and also lack the specificity. Nevertheless, physical bonds can be as strong as covalent bonds. Additionally they are long ranged while the molecules are entirely free to move [5].

2.1.2. Electrostatic forces

The strongest physical bond is caused by charge-charge interactions between two bodies. The interaction can be attractive or repulsive and is additive. The force is very long ranged and decays with the square of the distance (r^{-2}). Electrostatic forces can be weakened significantly in a medium dependent on its dielectric constant [5].

2.1.3. Van-der-Waals forces

Although many molecules are not charged, they can carry an electric dipole. This dipole can either be permanent or induced by an electric field. It can also occur spontaneously due to positional fluctuations of electrons. The forces between these dipoles are summarized in the Van-der-Waals forces:

- The Keesom force is the interaction between two permanent dipoles with the permanent dipole moment u, the dielectric constant ε and the distance between the dipoles r.

$$E_{\text{Keesom}} = -\frac{u_1^2 u_2^2}{3(4\pi\varepsilon)^2 k_B T r^6} \tag{1}$$

- The Debye force summarizes the interaction between a permanent and an induced dipole. The induced dipole is caused by a polarization by the electric field of the neighboring permanent dipole. α is the polarization of the molecule.

$$E_{\text{Debye}} = -\frac{u^2 \alpha}{(4\pi\varepsilon)^2 r^6} \tag{2}$$

- Interactions between induced dipoles in nonpolar molecules are called dispersion or London forces [5]. They are responsible for the largest contribution to the Van-der-Waals force. The dispersion force is of quantum mechanical origin and caused by

finite position changes of the electrons. This leads to the formation of a dipole with an electric field, which can induce another dipole in a neighboring molecule. Dispersion forces are responsible for most of the interactions in condensed matter, although they are weaker than electrostatic forces and covalent bonds. ν_i indicates the ionization frequencies of the molecules and ε_0 the dielectric constant in vacuum.

$$E_{\text{Dispersion}} = -\frac{3}{2}\frac{\alpha_1\alpha_2 h\nu_1\nu_2}{(4\pi\varepsilon_0)^2 r^6(\nu_1+\nu_2)} \tag{3}$$

Similar to electrostatic forces, the presence of a medium weakens the Van-der-Waals forces. On average, the Van-der-Waals forces are in the order of $1k_BT$.
At short distances of around a few Angstrom (Å), the electron clouds of atoms can overlap and the interaction becomes repulsive. These repulsive forces together with the Van-der-Waals force are often described by the Lennard-Jones potential:

$$\omega(r) = 4\epsilon\left[\left(\frac{\sigma}{r}\right)^{12} - \left(\frac{\sigma}{r}\right)^{6}\right] \tag{4}$$

where σ is the distance at which the potential is zero and ε is the depth of the potential. The first part of the equation refers to the repulsive forces and the second part to the Van-der-Waals forces [5].

2.1.4. Hydrogen bonds

Hydrogen bonds are inter- and intramolecular bonds and occur between electronegative atoms (e.g. O, N or F) and hydrogen atoms bound to other electronegative atoms. The bonds are of electrostatic origin and with $5\text{-}10k_BT$ stronger than Van-der-Waals bonds but still weaker than covalent bonds. A hydrogen bond is directional, short ranged and tends to decay with the square of the distance (r^{-2}). Hydrogen bonds play a dominant role in water, where each oxygen atom can form two hydrogen bonds and each hydrogen atom one bond. This means that each water molecule can form up to four hydrogen bonds.

2.1.5. Hydrophobic effect

The hydrophobic effect plays an important role when nonpolar molecules, which are incapable of forming hydrogen bonds, are introduced into water. The free energy ΔG of the transfer can be described with the following equation:

$$\Delta G = \Delta H - T\Delta S \tag{5}$$

where ΔH is the enthalpy, ΔS the entropy change and T the temperature. As the nonpolar molecules cannot form hydrogen bonds, they disrupt the hydrogen bond network of the water molecules. The water molecules around the nonpolar molecules have to rearrange in order to form as many hydrogen bonds as possible. The water in this area then differs from the bulk water and forms a structured solvation shell around the nonpolar particle. The formation of a solvation shell is entropically unfavorable as the motion of the water molecules is restricted.
The nonpolar molecules aggregate to reduce the disruption of the hydrogen bond network. The insolubility of nonpolar molecules in water together with the entropic nature of this clustering is called the hydrophobic effect [6]. This gives rise to the hydrophobic attraction: hydrophobic particles in water are stronger attracted to one another, because they aggregate

to keep the disturbance of the water's hydrogen bond network to a minimum. This hydrophobic attraction is believed to be a main driving force in protein folding. Hydrophobic amino acids cluster together and form a hydrophobic core which is only marginally exposed to the solvent. A more detailed description is given in chapter 4.

2.2. Adhesion and interfacial energy

Adhesion is defined as the work ΔW needed to separate two different surfaces from contact [5]. In case of identical surfaces it is called the work of cohesion. This is valid for any length scales [5]. Adhesion can be caused by electrostatic interactions, hydrogen bonds, Van-der-Waals forces, but also hydrophobic attraction can contribute significantly.

One application for the concept of adhesion is the wetting of a surface. A droplet of a liquid is transferred to a surface and settles on the surface. The total work of adhesion W_{LS} is then described by the Young-Dupré-equation (6) and the Young equation (7) [5]:

$$\gamma_L(1 + \cos\theta) = W_{LS} \tag{6}$$

$$\gamma_{LS} + \gamma_L \cos\theta = \gamma_S \tag{7}$$

γ_{LS} is the total surface energy, γ_L the surface energy of the liquid and γ_S the surface energy of the surface. The contact angle θ is the angle between the tangent to the droplet and the surface.

Hence, the contact angle can provide information about the wettability of a surface. The stronger the liquid is attracted to the surface, the more the droplet will spread out and the contact angle will decrease. When the attraction of water to a surface is high and a low contact angle is measured then the surface is rather hydrophilic. A hydrophobic surface repels the water and the contact angle increases. In this thesis the contact angle was chosen as one parameter to characterize the utilized surfaces. See chapter 3.6.5 for experimental details.

2.3. Single polymer desorption

A main part of the work presented here concentrates on single polymer desorption measured with the atomic force microscope. Force-distance curves under varying conditions are obtained, whereby two main motifs are observed during the desorption measurements: rupture events and plateaus of constant force.

2.3.1. Rupture events

Rupture events occur at non-equilibrium conditions when the vertical speed of the pulling experiment is faster than the relaxation time of the polymer on the surface [7, 8]. The polymer gets stretched between the tip of the AFM and the surface until the bonds with the surface abruptly break.
In the experiment these rupture events manifest themselves by rupture peaks. These then allow the determination of the maximal rupture force, which is given by the maximal value of the force peak, but also the elasticity of the polymer. An increase in maximal rupture force with the logarithm of the pulling velocity is characteristic for such an experiment . This was shown amongst others for single DNA molecules [9].

For a more detailed evaluation of rupture events, different polymer models can be applied. The most common ones are the worm-like chain (WLC) and the freely jointed chain (FJC) model. Both models assume that monomers separated by large distances do not interact [10]. In the FJC model it is further assumed that the polymer consists of N rigid elements of length b which are connected by hinges. These hinges are free to rotate while all torsion angles are equally alike. The length b of such an element is called Kuhn length.
The WLC model is more realistic and assumes that the polymer does not consist of rigid elements but is continuously flexible [10]. The characteristic length scale used here is the persistence length p, which is half the Kuhn length b. To apply the WLC model to experimental data, an approximate interpolation formula is used, because the exact solution is only given numerically [11]:

$$f(z) = \frac{k_B T}{p} \cdot \left(\frac{1}{4(1 - z/L)^2} - \frac{1}{4} + \frac{z}{L} \right) \tag{8}$$

f is the measured force, z the measured distance, k_B the Boltzmann constant and T the temperature. All these parameters are known. The persistence length p as well as the contour length L are fit parameters.

2.3.2. Plateaus of constant force

If the bonds between polymer and surface relax faster than the time needed to desorb the polymer from the surface, plateaus of constant force are observed. The plateaus are in quasi-equilibrium and allow to determine the desorption force and the corresponding adhesion free energy [12].

In contrast to rupture events, the height of the plateau (plateau force) as well as the length (detachment length) is independent of the pulling speed. This holds at least true for the regime accessible to the AFM (Figure 2) [13].

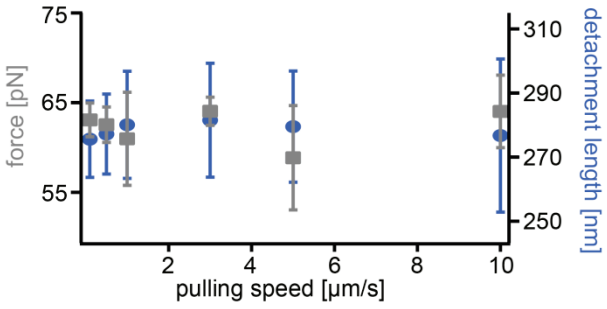

Figure 2. Dependence of the plateau force (grey) and the detachment length (blue) on the pulling velocity for poly-L-lysine on a hydrophobic self-assembled monolayer in water at room temperature. Adapted from [13].

In recent years, a lot of insight was gained in the mechanism and the characteristics of these plateaus of constant force. A few examples will be described in the following.

Adhesion at interfaces and the effect of hydrophobicity of the surface

To delineate the influence of different interfaces on the plateau force (desorption force), poly-D-tyrosine was desorbed from various substrates. Although the interfacial energy changed significantly, the plateau force stayed almost constant (Figure 3) [14]. This even holds true for

measurements on chloroform and on air bubbles. The results are explained by a compensation mechanism of dispersive and hydration forces [14].

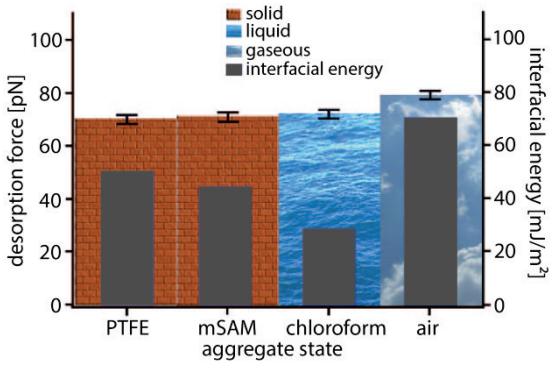

Figure 3. Desorption force for poly-D-tyrosine on different interfaces (color-coded) with varying interfacial energy (grey bars) and aggregate state. Adapted from [14].

A different study used a combined experimental and molecular dynamics simulation approach to investigate the influence of the surface hydrophobicity on polymer adhesion. Force-distance curves were measured on self-assembled monolayers (SAMs) with varying ratios of CH_3 (hydrophobic) and OH (hydrophilic) head groups [15]. The experimental data showed that when the surface was too hydrophilic (contact angle ≈ 50°-60°), no more plateaus of constant force were observed and the polymers did not interact with the surface anymore. The same conclusion was drawn from molecular dynamics simulations. They further revealed that the reason for this resistance was a strongly bound interfacial water layer at the hydrophilic surfaces [15].
To conclude, all measurements did show only a minor influence of the surface on the plateaus of constant force.

Solvents and co-solutes

The next step was to change the solvent or its composition instead of the surface. Measurements in water-ethanol mixtures did result in different interfacial energies. Changing the surface did also influence the interfacial energy, but this had only minor effects on desorption experiments (see above). Here, however, the height of the plateaus of constant force changed significantly (Figure 4A). With increasing ethanol concentration, a decrease in force could be observed [13, 14]. The same behavior was recently shown for the detachment length (Figure 4B) [12]. An increase in ethanol concentration is equivalent to a reduction of interfacial energy. Water took the place of the polymer and the desorption force and the detachment length decreased [14].

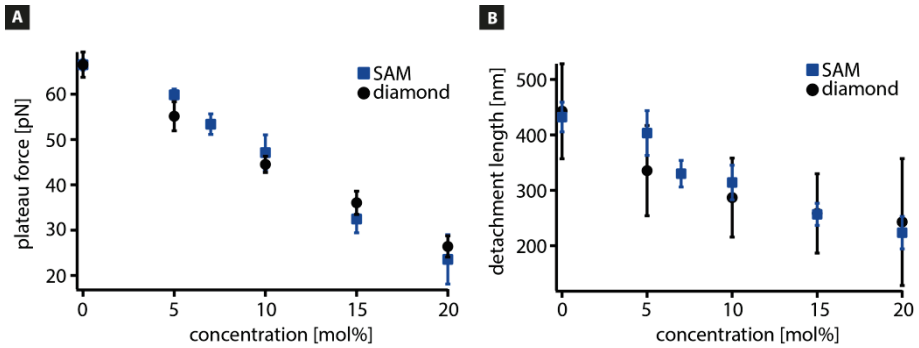

Figure 4. Dependence of (**A**) the plateau force and (**B**) the detachment length on ethanol concentration. The measurements were performed with poly-L-lysine on either a hydrophobic SAM (blue squares) or a hydrogenated diamond (black circles). **A** is adapted from [13].

Ethanol can not only be used to change the interfacial energy, but it can also act as a co-solute. The binding parameters of co-solutes to single polymers were determined by single polymer adhesion measurements [16]. The change in desorption force F_{des} with increasing concentration (activity, a) can be translated in a line tension difference Δτ:

$$F_{\mathrm{des}}(a) = F_0 + \Delta\tau(a) \tag{9}$$

with F_0 being the plateau force measured without co-solutes. Obtaining such data sets on two different surfaces then allows extraction of thermodynamic parameters of the co-solute binding by simultaneous fitting:

$$\frac{\Delta\tau}{k_B T} = d_s^{-1}\ln(1 + aK_s) - d_b^{-1}\ln(1 + aK_b) \tag{10}$$

where d corresponds to the number of adsorbed co-solutes per length and K to the association constant. The index s denotes the state where the polymer is adsorbed to the surface, while b stands for the state when the polymer is in bulk. The bulk state is the same for both surfaces. A major prerequisite for this approach, however, is a different dependence of the plateau force on co-solute concentration (activity, a) on different surfaces [13, 16]. For the above mentioned measurements with poly-L-lysine on a SAM and a hydrogenated diamond (Figure 4) no deviation in force was observed. Therefore the fit parameters described above were not sufficiently defined. In order to determine the thermodynamic parameters for ethanol binding, thus a surface with a different dependence on ethanol concentration needs to be found. Only then it is possible to determine the binding parameters to single polymers reliably.

Ions and the Hofmeister effect

Another topic of interest is the effect of ions on plateau force. This was investigated via the interaction of a spider silk motif with a hydrophobic SAM in the presence of different Hofmeister salts (i.e. salts with different ability to salt out proteins) [17]. The more kosmotropic the anions were, the higher was the plateau force. This was expected as kosmotropic ions cause water molecules to interact favorably with one another. However, the observed differences were surprisingly small. Increasing the concentration in the physiological range changed the plateau force by only 10%.

Contributions to the free energy

An explanation for the rather small differences in plateau force observed in previous studies was provided by Horinek et al. [18]. The authors showed that molecular dynamics simulations of peptide adsorption are comparable to experimental data and suitable to identify the different contributions to the measured plateau force and the free energy respectively. In Figure 5, the different contributions to the enthalpy change ΔH and the free energy change ΔG between the adsorbed and the stretched polymer conformation are plotted for different temperatures. The individual interactions of the polymer (P), the solvent (in this case water, W) and the surface (S) with one another are quite large, but they cancel each other out. The resulting free energy change ΔG is unexpectedly low.

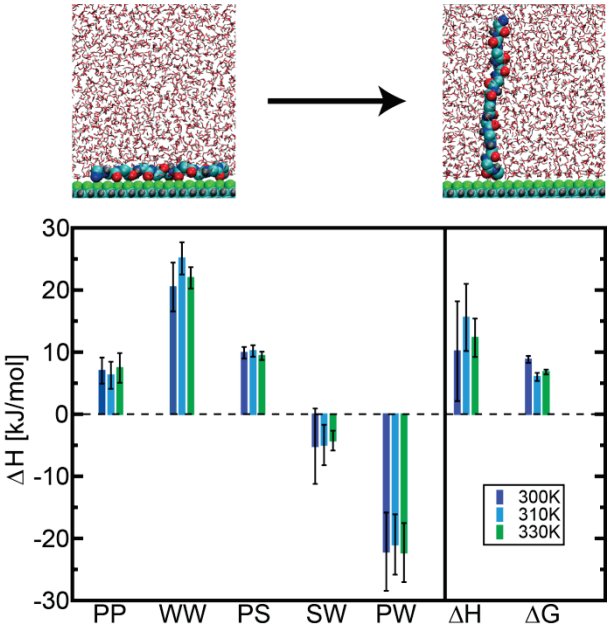

Figure 5. Contributions to the enthalpy change ΔH between the adsorbed and the stretched conformation of polyglycine on a hydrogenated diamond for three different temperatures. The interactions between peptide (P), water (W) and surface (S) contribute to the total enthalpy change ΔH and free energy change ΔG and level each other to some extend off. The figure is adapted from [19].

In summary, a great variety of parameters were altered in single molecule desorption experiments. It has to be noted that most of them had only minor effects (around a factor of two) on the plateau force, most likely because the individual contributions even out.

2.4. Tribology and friction

500 years ago the basic laws of friction were established by Leonardo da Vinci and approximately 200 years later redescribed by Amontons. The friction force is proportional to the applied load, independent of the contact area and of the sliding velocity. However, these laws are only valid for dry friction and in the absence of adhesion between the two opposing surfaces. If additional adhesion occurs, the friction force F_R depends on both the load F_N and the adhesion F_A, with the adhesion further depending on the contact area:

$$F_R = \mu F_N + F_A \tag{11}$$

in which μ is the friction coefficient. The real contact area caused by adhesive interactions depends on the strength of these interactions and on the elasticity of the surface [5].

Not until 1950 a physical description of friction force at interfaces was provided. Then, tribology as a new field of science was established [20] and can be described as the science about energy dissipation associated with friction, lubrication and wear. Still a universal theory combining friction and wear is missing, but is has to be noted that low friction is not always associated with low wear.

2.4.1. Motifs during friction measurements

While two opposing surfaces slide past each other, different motifs can be observed. Before the surfaces start to slide, the adhesion between them has to be overcome. Before sliding can begin the driving force has to be as high as the adhesion force between the two surfaces. This is reflected by an increase in friction force F_R with time and is referred to as stiction (Figure 6).

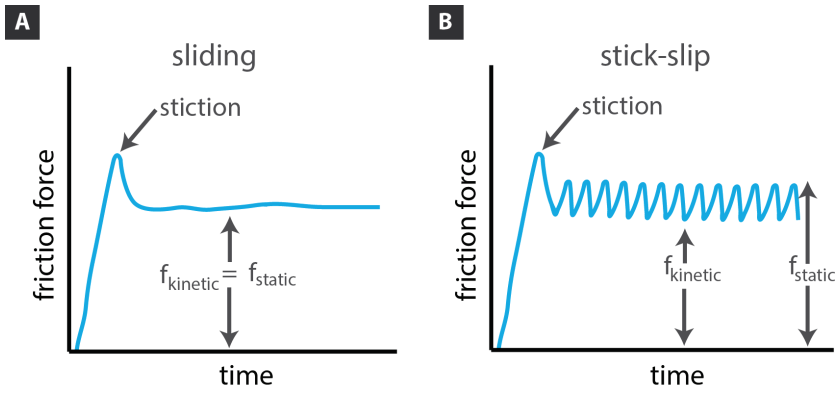

Figure 6. Different motifs can be observed during sliding of two surfaces past each other: (**A**) Stiction followed by sliding, for the case of a similar kinetic $f_{kinetic}$ and static friction force f_{static} and (**B**) stiction followed by stick-slip in case of f_{static} being higher than $f_{kinetic}$. The stick-slip pattern can also be less regular.

After the initial stiction peak two different scenarios can be observed: smooth sliding or stick-slip. Smooth sliding occurs when the kinetic friction force $f_{kinetic}$ equals the static friction force f_{static} (Figure 6A) and stick-slip when the kinetic friction force is lower than the static one (Figure 6B). Here the slider accelerates (after reaching f_{static}) to a velocity higher than the driving velocity and the measured friction force decreases ("slip"). The coupling of the two surfaces decelerates the movement of the slider and the friction force increases until f_{static} is again reached ("stick"). After this the stick-slip cycle starts from the beginning (Figure 6B). Stick-slip motion is one reason for induced damage or wear at surfaces [21]. A transition from stick-slip to sliding can be achieved by increasing the sliding velocity [20].

In the case of dry sliding (without any fluid present) stick-slip can be explained by the surface topography. It occurs due to collision of the asperities of the opposing surfaces. During sliding the slider climbs an asperity on the opposing substrate. After reaching the peak a rapid acceleration occurs ("slip") until the slider crashes into the next asperity ("stick") [22]. During lubricated friction, stick-slip can be caused by another phenomenon namely by shear-melting transitions of the lubricant [23].

2.4.2. Lubrication modes and the Stribeck curve

The focus of this chapter is on friction with a fluid (i.e. the lubricant) between two surfaces.

In the presence of a lubricant, the lubrication regime can change with sliding velocity, load and also viscosity of the lubricant. The different lubrication modes are summarized in the Stribeck curve (Figure 7). During boundary lubrication (high load and low speed), the opposing surfaces are in physical contact with one another due to the fluid film being thinner than the height of the asperities of the surface. Therefore, surface chemistry is of great importance. With increasing speed and/or decreasing load, a thicker fluid film is formed and the change from boundary to mixed lubrication occurs. The fluid film can protect the surface from damage and wear, but in the mixed lubrication regime the roughness of the surface is still important. In the case of hydrodynamic lubrication, the morphology and composition of the surface plays only a minor role as the fluid film gets thicker.

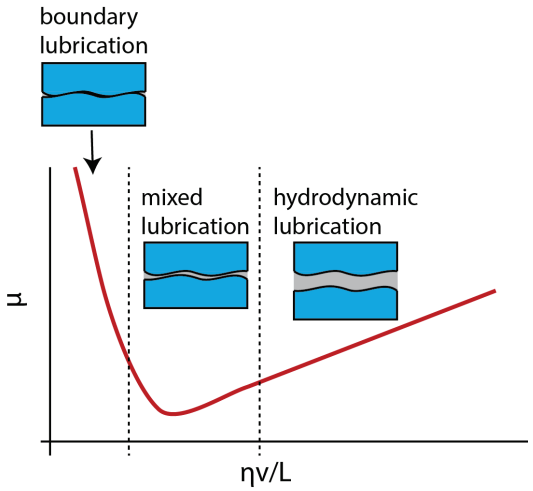

Figure 7. Stribeck Curve showing the dependence of the friction coefficient μ on sliding speed v, load L and viscosity η of the lubricant.

The friction coefficient observed in the boundary lubrication regime is higher than during mixed or hydrodynamic lubrication. With the help of boundary lubricants adsorbed to the surface, however, the friction coefficient can be reduced [24]. Examples are lipids, polysaccharides or even polyelectrolyte brushes.

Another effective boundary lubricant is water. It can form a hydration layer at a hydrophilic surface. When two of these surfaces are brought into close contact, then the repulsive forces caused by the steric interaction of the two hydration layers prevent solid contact. Water can also be used as an effective lubricant, which is intuitively understood from the low friction coefficient of ice that is caused by a thin water film on the surface. Using water has the advantage that most of the biological processes take place in aqueous environment, but drawbacks are the inability to work under high contact pressures [20].

For biological surfaces like articular cartilage, the Stribeck curve can sometimes be misleading. A decrease in the friction coefficient with sliding velocity is not necessarily associated with the formation of a fluid film but with the transition from stick-slip to smooth sliding. This occurs with increased velocity and reduces the overall friction coefficient [20].

2.5. Articular cartilage

2.5.1. Structure and composition

Three different types of cartilage are present in the body: elastic, fibrous and hyaline cartilage [4].
Elastic cartilage is present in the outer ear or in the Eustachian tube. Its unique characteristic are the highly branched elastin fibers, which give rise to the high elasticity of this type of cartilage.
Fibrocartilage, which can be found for example in the menisci, contains type I collagen which can absorb high amounts of load. This is worth noting as cartilage tissue is normally composed of type II collagen.

The focus of this work lies on hyaline or rather articular cartilage. Articular cartilage covers the end of bones in synovial joints. It provides low friction and at the same time is able to bear high loads. The more loading occurs, the thicker the cartilage gets with time. The thickness varies with the location in the joint and is about 1-2mm in adult cartilage [25]. The loads applied to the cartilage tissue reach several times the body weight. For example in the knee joint a load of about 3.5 times the body weight can be present.
Cartilage is a porous network with a pore size of less than 6nm [26] and is filled with fluid. The permeability is low, so the fluid is mostly trapped in the structure. If load is applied, the volume of cartilage decreases because the fluid is squeezed out. During the day, loading and unloading cycles alternate which allows the cartilage to recover. Still a 15-20% compression is present at the end of the day. A longer period of resting and unloading (for example during the night's sleep) is needed to fully recover the initial volume [4].

The main component of cartilage is water (70-80%) containing ions. The solid fraction consist of 50-75% collagen, 15-30% proteoglycans (e.g. aggrecan and hyaluronic acid), chondrocytes and other minor proteins. Cartilage is thus a triphasic material consisting of a solid network, charged proteoglycans and a fluid. Its composition varies with depth (Figure 8) [26].

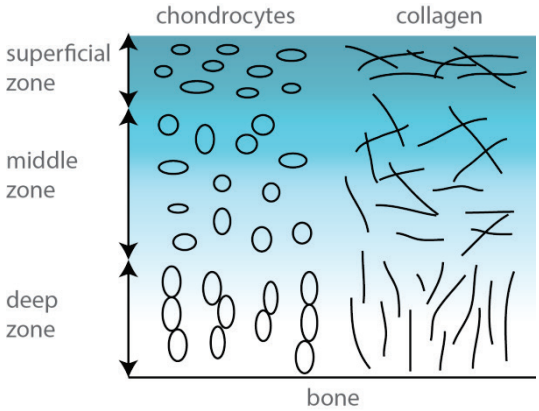

Figure 8. Zonal variation of the shape and orientation of chondrocytes [27] and collagen fibers in the superficial, middle and deep zone of articular cartilage [4].

The upper 10-20% of cartilage (i.e. the part most distant to the bone) are called superficial zone [26]. Here collagen is densely packed and oriented in parallel to the surface. This orientation helps to distribute any compression radially to resist shear and tension. Only a low amount of proteoglycans and a low permeability can be found in this zone. The

chondrocytes are rather flattened and synthesize proteoglycan 4 (PRG 4, also known as lubricin, superficial zone protein (SZP) or megakaryocyte-stimulating factor). PRG4 is oriented along the collagen fibers parallel to the surface and assumed to play a role in lubrication [4].
Below the superficial zone is the middle zone of cartilage (40-60%) [26]. In this area, the collagen fibers are more randomly oriented. The chondrocytes are spherical and posses greater synthetic capability than the cells in the superficial zone. The concentration of proteoglycans reaches its maximum in this zone [4].
Beneath the middle zone lies the deep zone. It is the last zone before the bone [26]. Collagen assembles into large fibers which are oriented perpendicular to the surface and anchored in the bone. This leads to a high resistance against shear, which is important as almost no expansion of the tissue can occur due to its location near the bone. Both the proteoglycan concentration and the cell density are low in this area. The chondrocytes are elongated and organized in columns [4].

Chondrocytes

Only a low amount of cells (chondrocytes) is present in articular cartilage. As cartilage is avascular, the nutrients can reach the cells only through diffusion which is facilitated by the joint movement, therefore chondrocytes show only a very slow to no proliferation at all. As they are responsible for remodeling the matrix and new components need to diffuse to the cells, the matrix turnover is very slow (more than 100 years for collagen, 8-300 days for the proteoglycan aggrecan). Therefore the self-repair of cartilage tissue after for example an injury is problematic [4].
The physical forces present in cartilage like shear stress, loading or hydrostatic pressure are transmitted to the chondrocytes via the extracellular matrix and trigger biochemical signals in the cells. These signals lead to matrix remodeling or proliferation. Thus inappropriate loading can also change the matrix properties. As loading changes with depth [28], this sensitivity to loading is one reason for the zonal variations of the chondrocytes in shape [27] and synthetic capabilities. Mechanical stimuli, however, are as well important during the development of cartilage to maintain the right formation and structure of the network [4, 29].

Collagen

As mentioned before, most of the collagen in articular cartilage (90%) is type II collagen. It is formed by the assembly of three collagen proteins to a right-handed triple-helix [26]. The trimers merge to form fibers with a typical repeat length of 67nm [30]. These fibers form the framework of cartilage. It is able to resist tensile forces from motion and from the swelling pressure caused by the negative charges of the proteoglycans. Not only the appearance of the chondrocytes changes with the location in the tissue, but also the orientation and fibril size of collagen. Like chondrocytes, collagen is adapted to the amount of load present in a particular zone. This leads to an “arcade like” distribution of collagen with an orientation parallel to the surface in the superficial zone, a more random distribution in the middle and finally an orientation perpendicular to the surface in the deep zone [31]. To further increase the tensile resistance of collagen, cross-linking occurs. The amount of cross-linking increases with age and the matrix thus stiffens [4].

Proteoglycans

A proteoglycan is a macromolecule with an extended protein core with glycosaminoglycan (GAG) chains (e.g. chondroitin sulfate) attached to it. Examples are aggrecan or hyaluronic acid (see below). These proteins form large aggregates which are trapped inside the collagen network. Proteoglycans are highly negatively charged. The high density of negative charges drags water into the tissue and causes the tissue to swell. The underlying effect is the "Donnan effect". The swelling is counterbalanced by the collagen network which leads to the formation of a prestrain in cartilage without any load present. The fluid trapped in cartilage by the proteoglycans is called the interstitial fluid. If the tissue is loaded, the load is mainly dissipated in the interstitial fluid. A high interstitial fluid pressure due to the low permeability of cartilage thus develops. As most of the load is supported by the fluid and not by the solid, the measured friction force at the surface is very low. The fluid pressure decreases with time, because the fluid leaves the loaded areas slowly. The solid fraction of cartilage needs to support more and more of the load and the friction force increases. The loss of aggrecan can serve as an early marker for disease, as this leads to a breakdown of the interstitial fluid pressure and a higher loading of the solid matrix. Consequences are mechanical problems in the tissue [4].

Synovial fluid

The fluid in the joint capsule in between the opposing cartilage surfaces is called the synovial fluid. It consists of water containing electrolytes like sodium and chloride, but also of hyaluronic acid (~3mg/ml) and PRG 4. These constituents can adsorb at the cartilage surface and serve as a boundary lubricant during sliding. Synovial fluid itself is viscous and non-Newtonian, which means that its viscosity changes with velocity. Synovial fluid supplies the tissue with nutrients and is also responsible for the removal of waste [32]. Furthermore it fills the asperities on the surface and maintains the high interstitial fluid pressure. A high interstitial fluid pressure is one reason for the persistence of cartilage, because under normal conditions most of the load is supported by the interstitial fluid leading to the solid matrix being only slightly loaded [4].

2.5.2. Lubrication mechanism

Cartilage is generally exposed to large amounts of loading forces which can reach several times the body weight. Additionally, the direction of the movement is changed repeatedly in everyday life. Both are major issues for artificial joints, in natural joints, however, friction and wear are very low. Furthermore, as cartilage has such a low turnover rate it needs to last and function properly over many decades. Up till now it has not been possible to build a material with the same astonishing frictional properties. Low friction and low wear in cartilage are not the result of a single lubrication mechanism, but the lubrication mechanism adapts to changes in normal load, shear stress or sliding rate [33, 34].
One of the most important lubrication mechanisms is the interstitial fluid pressurization. As mentioned before, the negatively charged proteoglycans draw water into the porous cartilage network and cause the network to swell. Together with the low permeability of cartilage, this produces a high interstitial fluid pressure which is counterbalanced by the collagen network. If the tissue is mechanically loaded, most of the load is supported by the fluid [35, 36]. This explains the low friction coefficient in joints as only the fraction of load

supported by the solid accounts for a measurable friction force. This was experimentally verified by the treatment of cartilage with chondroitinase, which led to an increase of the friction coefficient [37, 38].
Studying lubrication mechanisms on cartilage, it is important to understand how motion might influence friction. If a contact continuously migrates over the cartilage surface, the friction force remains low and constant (Figure 9A and B) [39]. Although the fluid is squeezed out of the loaded area, after moving the contact, the fluid can flow back from adjacent areas, restoring the interstitial fluid pressure and the low friction coefficient. In nature this is equivalent to repeated loading and unloading cycles of different areas in the joint during movement.
However, if one region of the cartilage surface is permanently loaded, the fraction of load supported by the fluid decreases with time because water is squeezed out of the loaded area without being able to flow back and more and more load has to be supported by the solid fraction [40, 41]. A static contact thus causes an increase in the friction coefficient from an initial value μ_o to an equilibrium one μ_{eq} (Figure 9A and C). The time t until equilibrium is reached depends on the contact area a and can be estimated using the following equation:

$$t \sim \frac{a^2}{H_A k} \tag{12}$$

H_A is the aggregate modulus of solid matrix and k the hydraulic permeability [42, 43]. Representative values are 13MPa for H_A and $0.6 \cdot 10^{-15} m^4/Ns$ for k [42]. For AFM experiments a is in the order of 5µm (see chapter 3.4.1) with a time t of approximately 3ms. The time needed to scan one line is at least 33ms for the fastest scan speed. Therefore, the interstitial fluid pressure will decrease rapidly and only equilibrium friction can be probed. For tribometer measurements the duration until equilibrium would be reached is much higher than the time needed to scan one line. Therefore, the migrating contact regime and the effect of the interstitial fluid pressurization is probed.

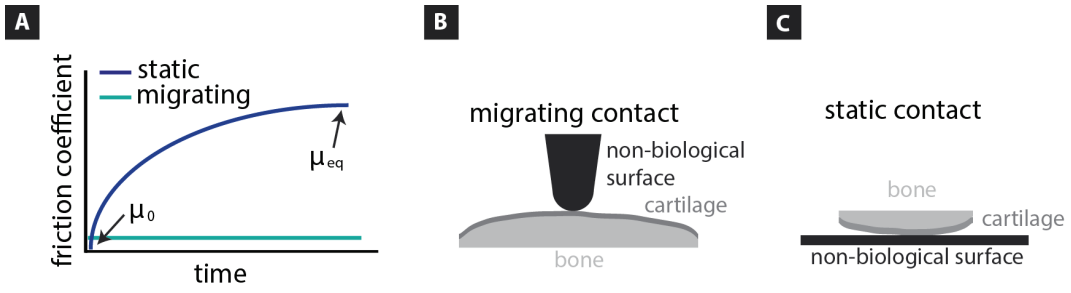

Figure 9. (**A**) Schematic trend for the time dependent friction coefficient for an experiment with a static contact area (blue) and a migrating contact (green). The equilibrium friction coefficient μ_{eq} and the initial friction coefficient μ_0 are indicated with arrows. Examples for a experimental setup with (**B**) a migrating contact and (**C**) a static contact.

In case of equilibrium friction, only the boundary lubrication regime is probed [20] as the two opposing surfaces are only separated by a molecular thin fluid layer. Thus the chemical composition of the upper cartilage layer is of great importance. It consists of different polymers that either reach out of the surface or are adsorbed from the synovial fluid. PRG4, hyaluronic acid and surface-active phospholipids (SAPL) have already been identified as potential boundary lubricants [44]: Knock-out mice without PRG4 showed an increased

friction, which is associated with the lack of repulsion between the opposing surfaces [45]. The repulsion is caused by the negative charges and favors the reduction of friction [5, 46]. Enzymatic digestion of PRG4 also increased the friction coefficient but digesting hyaluronic acid or SAPL has shown to only have a minor effect on friction [38, 44].
Especially for the use of hyaluronic acid as a boundary lubricant different conclusions were drawn: Schmidt et al. did show that using hyaluronic acid and PRG4 as lubricants lowered the friction coefficient. A combination of both even improved the friction coefficient further [47]. Schiavinato et al. however reported that hyaluronic acid did not improve the friction between two opposing cartilage surfaces while measuring with a migrating contact, but the equilibrium friction coefficient of a static contact experiment decreased after the addition of hyaluronic acid [48]. Furthermore it was observed that synovial fluid reduces the friction, but only when sliding cartilage against cartilage and not cartilage against metal [49]. Under certain loading conditions and sliding velocities, the polymers at the opposing surfaces were even shown to interact and entangle with one another. This caused stick-slip motifs during sliding. Such a regime is not favorable, because stick-slip is one reason for induced wear at the surface as already mentioned above. The wear even further increased after enzymatic digestion of hyaluronic acid, while the friction force remained almost unchanged [21].

Due to the porous structure of cartilage, the occurrence of a thick fluid film on the cartilage surface seems unlikely as the fluid will quickly flow back into the cartilage network [36]. Still, synovial fluid is important to supply cartilage with boundary lubricants. A prior wiping of the cartilage surfaces increased the friction coefficient which was probably due to removal of weakly bound boundary lubricants on the surface [50]. In addition, synovial fluid is responsible for the transfer of load across the cartilage-cartilage interface. This is mainly possible due to the high viscosity and elasticity caused by hyaluronic acid [51, 52].

3. Materials and methods

3.1. Setup and tip functionalization for single molecule experiments

For all measurements the atomic force microscope (AFM) MFP-3D SA (Asylum Research, an Oxford Instruments Company, Santa Barbara, CA) is used. It is equipped with an upgrade to guarantee a higher lateral sensitivity and to allow not only the normal, but also the lateral deflection to be set to zero. This is necessary for friction force microscopy (see 3.4.1). Additionally it is possible to control the solution temperature. With an AFM, a force resolution of 10pN with a spatial resolution in the nm-range can be achieved. The AFM consist of a cantilever with a tip attached to it (Figure 10). Forces acting between the tip and a substrate deflect the cantilever. The normal and the lateral deflection is detected by a laser which is reflected from the backside of the cantilever to a photodiode.

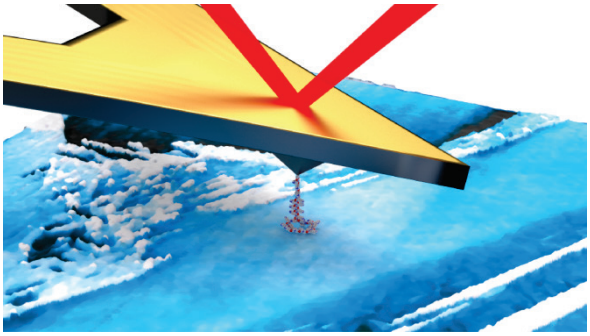

Figure 10. Schematic of an atomic force microscope cantilever with a laser reflected from the backside. The cantilevers used for single molecule force spectroscopy are around 200-300µm in length and 20µm in width with a tip height of 2.5-8µm. A poly-L-lysine chain (several 100nm) is attached to the tip via a poly(ethylene) glycol linker (approximately 30nm).

The first part of this thesis concentrates on the investigation of the desorption behavior of single polypeptides. For this purpose, the polypeptides are covalently coupled to an AFM tip (Figure 10) and the interaction with different substrates in different solutions is measured by performing force-distance curves. This method is called single molecule force spectroscopy (SMFS). A great advantage of this approach is that the interaction of a single polymer with different surfaces in different solvents can be probed with the same cantilever. This is possible because the polymer is covalently coupled to the AFM tip. Therefore, possible deviations caused by the determination of the spring constant can be ruled out and the uncertainty in force is only 2% [14]. Using different cantilevers would increase the error to approximately 12%.

For experiments with single polymers, it is important to achieve a high force resolution in the piconewton (pN) range. Hence, cantilevers (MLCT, Bruker AFM Probes, Camarillo, USA) with a low spring constant are used. The nominal spring constant varies between 10 and 40 pN/nm.

The first step for the covalent attachment of a single polymer to the tip is the activation of the cantilever in a plasma chamber with oxygen. Afterwards, the tip is coated with Vectabond™ to produce a surface completely covered with amino groups. The next steps depend on the functional end group of the polymer used. Figure 11 shows the different functionalization routes schematically.

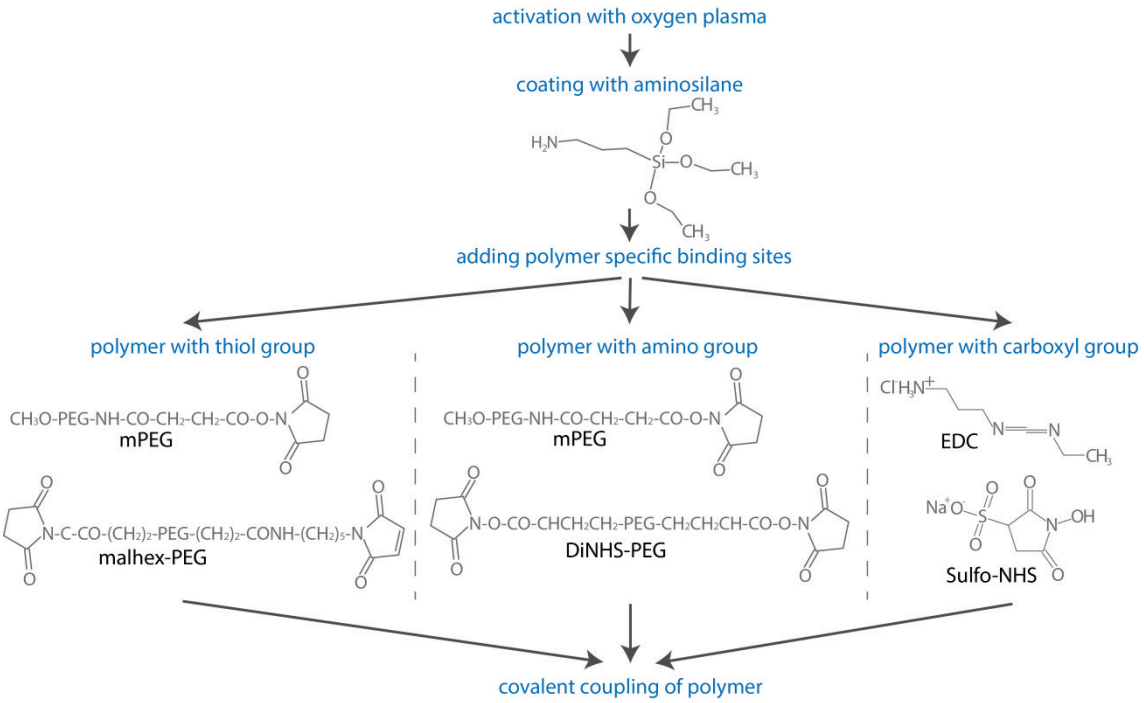

Figure 11. Schematic of the covalent coupling of a polymer via its thiol, amino or carboxyl group.

If the functional end group is an amino group, then a chloroform based 1:1500 mixture of DiNHS-PEG (PEG-α-ω-Di-NHS, 6kDa) and mPEG (CH_3O-PEG-NHS, 5kDa) is prepared. The cantilevers are incubated for 45 min in the solution. mPEG couples via the one NHS-ester to the amino groups on the tip. The free methoxy group now serves as a passivation so no unspecific interactions between the polymer and the tip and the tip and the surface occur. DiNHS-PEG has two NHS-esters. One binds to the tip, while the other one is still available for the coupling of the polymer.
If the functional end group of the polymer of interest is a thiol group, malhex-PEG (α-Maleinimidohexanoic-ω-NHS-PEG, 5kDa) is used instead of DiNHS-PEG. The NHS-ester can bind to the tip while the maleimide group is available for the coupling of the polymer via its thiol group.
The third type of polymer has a carboxyl group as a functional end group. Here, the functionalization protocol has to be adjusted. After the coating of the tip with Vectabond™, the cantilevers are directly incubated in the polymer solution together with EDC (1-Ethyl-3-[3-dimethylaminopropyl]carbodiimide hydrochloride) and Sulfo-NHS (*N*-hydroxysulfosuccinimide) which serve as reagents to convert the carboxyl groups to amine-reactive NHS-esters, so the covalent coupling of the polymer to the tip is possible.
A more detailed protocol is given in the Appendix.

3.2. Adhesion measurements and their evaluation

The normal spring constant of the cantilever has to be calibrated before each measurement. This is done with the thermal noise method [53, 54]. The frequency dependent Brownian motion of the cantilever is recorded and the resonance peak is fitted. Together with the inverse optical lever sensitivity (InvOLS), the spring constant is then determined. The InvOLS is fitted ten times for each cantilever on every surface, in every solution and at every

temperature. The determined spring constants for one and the same cantilever but not the InvOLS are averaged before the evaluation of the data.

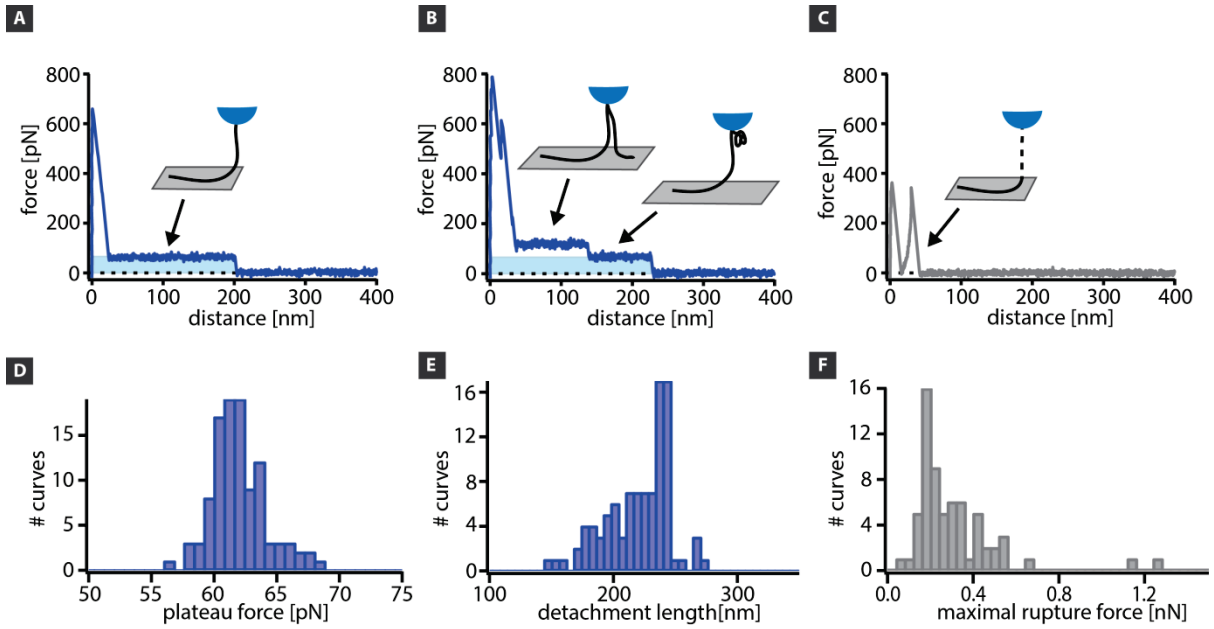

Figure 12. Two motifs were observed in force-distance curves during vertical pulling: plateaus of constant force with either (**A**) one step or (**B**) multiple steps in force or (**C**) rupture events. The insets show schematically the contour of the polymer during the simultaneous desorption of (**A**) just one or (**B**) two polymers from the surface or (**C**) the stretching of the polymer (indicated by the dashed lines). The light blue area corresponds to the free energy. The height (plateau force) and the length (detachment length) of the plateaus of constant force were determined by a sigmoidal fit and plotted in (**D**) and (**E**). In case of rupture events, the maximal rupture force was determined and again plotted in a histogram (**F**). The examples shown here correspond to measurements with polyisoprene in water on hydrogen terminated diamond at room temperature.

For each experimental condition (e.g. temperature, velocity or dwell) at least 100 force-distance curves are performed. During a force-distance curve, the surface is approached with a constant velocity. After a defined waiting time at the surface (to let the polymer adsorb), the cantilever is retracted with the same velocity.

Two different motifs are observed in the force-distance curves: Plateaus of constant force or rupture events.
If the first motif, plateaus of constant force occurs (Figure 12A and B), either one force plateau with a single step to the baseline or several steps in force are observed where the latter indicates the desorption of several individual polymer chains in parallel. In Figure 12B the simultaneous desorption of two chains is illustrated: After measuring the unspecific interaction with the surface (until approximately 30nm), the two polymer chains are desorbed simultaneously. At around 120nm the first, shorter polymer chain detaches from the surface, but the second, longer one is still in contact with the surface. This is reflected in the ongoing plateau of constant force, but now with a lower force [55]. The second polymer is desorbed further until it detaches at 220nm. Consequently the last step in the force-distance curve corresponds to the detachment of a single polymer. If only one step occurs (Figure 12A), then only one polymer is desorbed during the measurement. For the evaluation of plateaus of constant force, only a single step to the baseline is taken into account. The height of the plateau (plateau force, Figure 12D) and the length of the plateau (detachment length, Figure 12E) is fitted with a sigmoidal fit and plotted in a histogram. All average

values shown in this thesis correspond to the maximum of a Gaussian fit to the histogram and the errors to the standard deviation.

The plateaus of constant force further reveal information about the free energy ΔG (light blue area in Figure 12A and B). ΔG corresponds to the area under the plateau of constant force and is always normalized by the number of monomers. Therefore the measured desorption force is multiplied by the length of one monomer (assumed to be 0.36nm) and converted to kJ/mol. With temperature dependent measurements not only information about ΔG are gained, but also about the entropy change ΔS and the enthalpy change ΔH with temperature. Therefore ΔG is plotted versus the temperature T and fitted with a parabola (ΔG_{fit}). ΔS and ΔH are calculated using the following equations (see [19]):

$$\Delta S = -\delta \Delta G_{\text{fit}} / \delta T \tag{13}$$

$$\Delta H = T\,\Delta S + \Delta G \tag{14}$$

The second motif observed in force-distance curves are rupture events (Figure 12C). Rupture events occur when the polymer cannot be desorbed from the surface, but only stretched until the bonds between the surface and the polymer break. In these cases, the maximal rupture force is determined and plotted in a histogram (Figure 12F). The unspecific interaction with the surface at the beginning of the force-distance curves (if present) is neglected. For some experiments the determination of the interaction distance is needed. The interaction distance corresponds to the distance at which the force ultimately drops to zero. In the force-distance curve shown in Figure 12C, this would correspond to a distance of about 40nm.

3.3. Single molecule friction force microscopy

Besides probing the adhesion of single polymers on surfaces with the AFM, one can also study the mobility of these polymers on the surface [56]. This is done by single molecule friction force microscopy (SM-FFM). Like in SMFS, force-distance curves are performed, but with a slightly adjusted protocol (Figure 13).

First, the surface is approached with a constant velocity. After a dwell time at the surface of normally 1s, the cantilever is retracted for a defined z-distance (first grey part, Figure 13). In the example shown here the z-distance is around 178nm. At this point, the polymer is still in contact with the surface which is reflected by the ongoing plateau of constant force. Now, the cantilever is moved laterally, parallel to the surface for a defined x-distance (here: 450nm, blue part, Figure 13). In the example shown here the force decreases continuously until the polymer looses contact with the surface after approximately 0.38s and the force drops to zero. After another short waiting time, the cantilever is moved back in x-distance to its starting point (not shown). Finally the retrace in z-direction is completed (second grey part, Figure 13).
Three different motifs are observed in the measured force during the lateral movement of the polymer (Figure 14A). The first motif is a plateau of constant force, the second one a rupture event and the third one a continuous decrease in force.

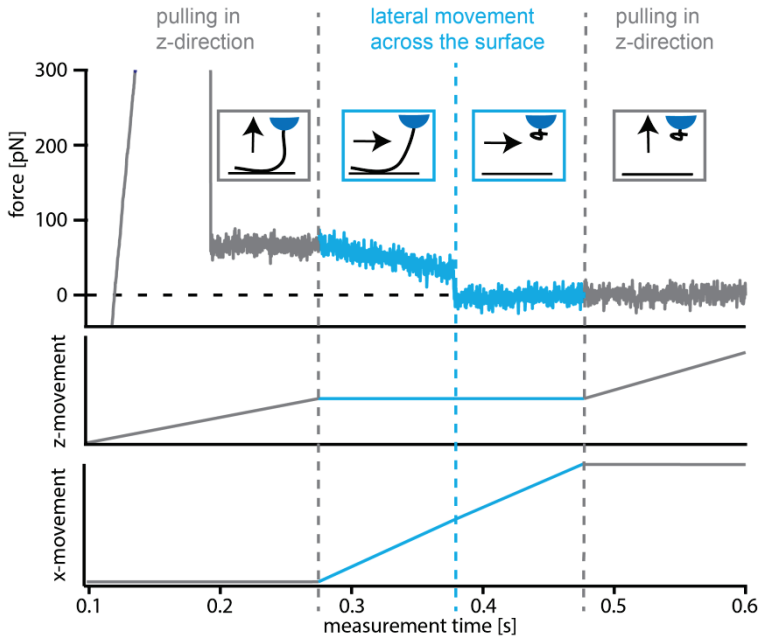

Figure 13. Scheme of a single molecule friction force microscopy experiment performed with a polyisoprene backbone grafted with polystyrene side chains (PI-*g*-PS(88)) on hydrogenated diamond in water. The upper graph corresponds to a measured force-time curve with the two lower ones illustrating the z- and x-movement of the piezos. First, the polymer is pulled up to a certain z-position (first grey part). This z-position is then held constant and the cantilever is moved laterally across the surface (blue part) before the z-movement is completed (second grey part).

For the plateaus of constant force, the polymer is completely mobile on the surface during the lateral movement while no friction can be detected. This behavior is called "sliding".
The second motif is a rupture event. Here, the polymer is not mobile but sticks to the surface with low internal chain dynamics. It is not possible to move the polymer laterally across the surface or to desorb the polymer monomer by monomer from the surface. Instead, the polymer is stretched (indicated with the dashed lines in Figure 14A) during the lateral movement of the cantilever until the bonds between the polymer and the surface break. This is called "cooperative stick".
The third motif, a continuous decrease in force, is called "desorption stick". In this case, the polymer is immobile on the surface (in x-y-direction) and in contrast to cooperative stick, the internal chain dynamics are still very high and it is possible to gradually desorb the polymer in z-direction until the polymer detaches completely and the force drops to zero. The observed continuous decrease in force can be explained geometrically (Figure 14B).
During the lateral movement, the force acting tangential to the polymer F_{tan} remains constant (red solid line triangle, Figure 14B). The angle Φ between the tangent to the polymer and the normal to the surface increases with increasing distance covered in x-direction R_x (grey dotted line triangle, Figure 14B). Due to the similarity of the grey and the red triangle, an increase in Φ with time and a constant force F_{tan} consequently leads to a decreasing force F_z. This is reflected in the measured force-x-distance curves. At the same time, the force acting in x-direction perpendicular to the cantilever axis F_x increases during the measurement.

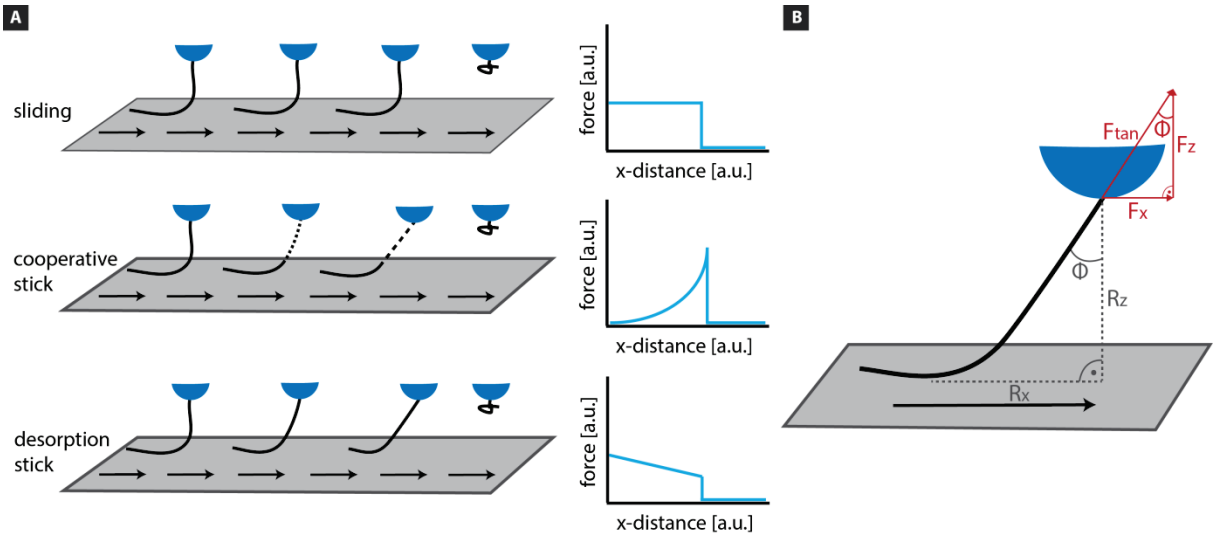

Figure 14. (**A**) Time dependent schematics of the three observed motifs during the lateral movement of a polymer across a surface with schematics of the measured force-x-distance curves: sliding, desorption stick and cooperative stick. The dashed lines indicate a stretching of the polymer. (**B**) Geometry during desorption stick. R_x: covered distance in x-direction, R_z: constant z-distance above the surface, F_x: force acting in x-direction perpendicular to the cantilever's axis, F_z: measured force in z-direction, F_{tan}: force acting along the tangent to the polymer, Φ: angle between the tangent to the polymer and the normal to the surface.

Unfortunately it is not possible to directly measure the force F_x, because the lateral spring constant of the cantilever is too high. Although with the help of geometrical considerations it is possible to calculate F_x from the measured force F_z, the fixed distance in z-direction R_z and the covered distance in x-direction R_x with the following equation:

$$\tan \Phi = \frac{R_x}{R_z} = \frac{F_x}{F_z} \tag{15}$$

Equation (15) is valid because, as pointed out above, the red and the grey triangle are similar. Some measurements also show a mixture of different motifs e.g. desorption stick followed by a sliding event or cooperative stick followed by desorption stick or even a combination of cooperative stick and sliding. This has already been discussed in detail in [57] and is not a topic of the thesis.

3.4. Microscopic friction force microscopy

Besides probing friction with a single polymer, it is also analyzed on the microscale. For this AFM-based friction force microscopy and tribometer-based friction force microscopy are used.

3.4.1. AFM-based friction force microscopy

Setup and measurement procedure

In order to measure frictional forces with the atomic force microscope, rectangular cantilevers with a spherical tip are used (Novascan, USA) (Figure 15). The sphere consists of polystyrene and has a diameter of 10µm. As surfaces, samples from articular cartilage with a diameter of 5mm are prepared as described in 3.6 and anchored in a home-built fluid cell. The fluid cell is filled with the lubricant of interest.

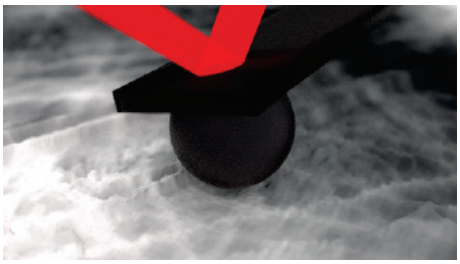

Figure 15. Rectangular cantilever with a spherical tip. The friction force between the sphere and the surface is derived from the lateral deflection with an optical lever system. The cantilevers used for friction force microscopy are 250µm in length and 35µm in width. The diameter of the sphere is 10µm.

During the measurement, the AFM is operated in contact mode. The cantilever is lowered until the sphere is in contact with the surface and the cantilever deflects vertically with a defined normal load F_N. Then it is moved laterally with a constant sliding velocity. The normal loads F_N range from 30 to 110nN and the sliding velocities from 9 to 113µm/s. The normal load is held constant (constant force mode) while the lateral deflection, caused by friction between the sphere and the surface is recorded. For one image, a line with a length of 15µm is scanned back and forth (retrace and trace) for at least 64 times. The scanning axis is chosen perpendicular to the cantilever's long axis so the cantilever deflects symmetrically during retrace and trace.
A typical example for the lateral deflection recorded during trace (grey) and retrace (blue) of one scan line is shown in Figure 16A. This is called a "friction loop". The data is collected while measuring on articular cartilage in a sodium chloride solution. The lateral deflection Δ at the beginning of the measurement before lateral movement (which is typically zero) is plotted as a dotted line as a guide to the eye. During the trace, the cantilever deflects in the positive direction and during retrace in the negative direction but ideally the offset to Δ should be the same for both traces.

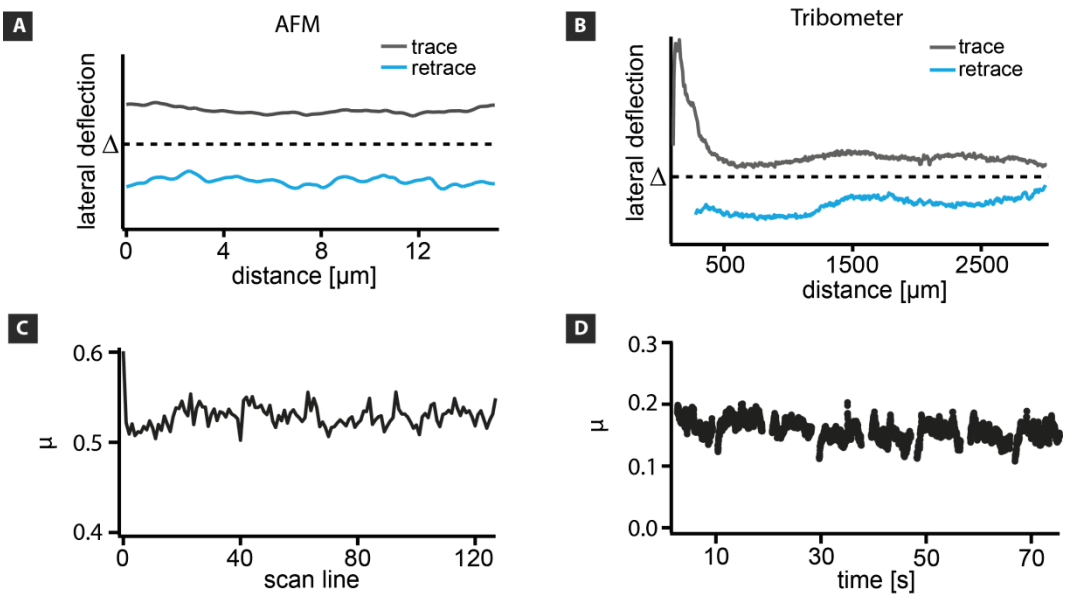

Figure 16. (**A**) Trace and retrace of the lateral deflection of the cantilever during the scan of one line with the AFM. (**B**) Trace and retrace of the lateral deflection of the cantilever during the scan of one line with the tribometer. The peak at the beginning of the trace corresponds to stiction which needs to be overcome before sliding can occur. (**C**) Dependence of the friction coefficient on scan line number for an AFM measurement. (**D**) Dependence of the friction coefficient on time during a tribometer scan. The measurements were performed in 154mM NaCl on articular cartilage.

To determine the average friction force F_R for one scan, the following equation is evaluated for each scan line:

$$F_R = \alpha \cdot \frac{\text{Trace} - \text{Retrace}}{2} \tag{16}$$

α is the lateral sensitivity which is needed to convert the signals from volts to the force unit Newton. Afterwards the average of all scan lines is taken. This is valid because the scan shows no dependence on scan line number and therefore on time (Figure 16C). The procedure is repeated for different normal loads and sliding velocities. To obtain the friction coefficient μ, F_R is plotted versus F_N for each velocity. The data is then fitted with a straight line, with the slope of the line corresponding to μ.

Calibration of the lateral spring constant

Prior to the measurements both the normal and the lateral spring constant of the cantilever are calibrated. The normal calibration of the cantilever is performed as described in chapter 3.2. on a solid surface like glass. Using a solid surface is important to get a correct value for the InvOLS. Consequently calibration on soft cartilage is not feasible.
The lateral sensitivity α is determined with the Diamagnetic-levitation-force-calibrator (DLFC) [58]. Therefore a diamagnetic pyrolytic graphite disk is put on top of four neodymium (NdFeB) magnets. The magnetic field of the magnets induces a magnetic moment in the graphite disk of opposing direction. The graphite disk is thus repelled from the magnets and floats. Graphite is chosen for its rather strong diamagnetism. The combination of the magnets and the graphite disk acts as a weak spring. To determine the spring constant, the free vibrations of the disk are recorded by a laser displacement tracer [58]. From the damped oscillations, the resonance frequency ω is determined and with this the spring constant k_s of the system:

$$k_s = m_g \cdot \omega^2 \tag{17}$$

m_g is the mass of the graphite platelet, which is determined by weighing. After k_s is known, the lateral sensitivity of the cantilever can be calibrated. Therefore the spring system is mounted together with the cantilever in the AFM. The cantilever is brought in contact with the graphite. The magnets, and hence the graphite disk, are moved a defined distance laterally, causing the cantilever to deflect laterally. The lateral distance of motion is chosen in a way that the cantilever is deflected only and the sphere does not slide over the surface (i.e. stiction is not overcome). During the movement of the piezo stage, the normal force (vertical deflection of the cantilever) is held constant and the lateral signal (lateral deflection of the cantilever) is recorded. With the assumption that the lateral displacement of the AFM piezo stage is similar to the lateral deflection of the spring, the lateral displacement can be converted with the know spring constant k_s to a lateral force. The inverse slope of a line fit to the lateral signal over the lateral displacement of the spring corresponds to the lateral sensitivity α of the cantilever.
It is observed that α depends on the intensity of the laser signal on the photodiode. The intensity typically decreases when transferring the cantilever into solution. Therefore the calibration of the lateral sensitivity is performed at different laser intensities in air to correct for the changed intensity in solution. α is in the range of 1-4μN/V. A more detailed

description of the calibration setup is given in the bachelor thesis of Lorenz Wiegleb supervised by the author of this work [59].

3.4.2. Tribometer-based friction force microscopy

The measurements are performed with a linear Nano Tribometer NTR from CSM Instruments (Peseux, Switzerland) at the Institute of Evolution and Ecology in Tübingen. The lateral and the normal deflection of the cylindrical probes are not measured with an optical lever system, like in an AFM, but with two capacitive sensors. Either a sphere (polystyrene, diameter 750µm) or a cylindrical platform is attached to the end of the probe. A cartilage sample with a diameter of 10mm is used as a surface. It is glued with the bony side first to the sample holder with an instant adhesive, while ensuring that the cartilage is not dehydrated during measurement. It is possible to compare the friction coefficient obtained with the tribometer to the results of the AFM measurements by using a polystyrene sphere in both setups. By gluing a second cartilage sample (diameter 5mm) with the bony side to the cylindrical platform on the probe it is furthermore feasible to directly measure the friction force of cartilage on cartilage. The normal loads range between 2-6mN with velocities from 50 to 600µm/s, both being held constant during each individual scan. For each parameter combination, one scan line (distance from 300-1500µm) is probed three to four times and the friction coefficient µ is determined for each point. The friction coefficients for trace and retrace vary in sign. Plotting the values for trace and retrace (without the reversal points) for one scan line results in a typical friction loop (Figure 16B). At the beginning of each scan, stiction is observed. This is not visible in AFM measurements, where the first scan line is not recorded.
For data evaluation, the friction coefficients µ are averaged for each scan but without the reversal points and the stiction part. Like in the AFM measurements, the averaging is valid because no dependence of µ on scan time is observed (Figure 16D). Stiction is evaluated separately by determining the maximum value of the friction coefficient at the beginning of each scan.

3.5. Polymers

The functionalization protocol allows to covalently bind a large variety of different polypeptides to the AFM tip. Different synthetic and natural polymers with different geometries are used in this thesis for single molecule force spectroscopy experiments.

3.5.1. Linear polymers

- Poly-L-lysine (PLL)
  Lysine (Figure 17) is one of the essential amino acids in humans. Due to a pk_a of 10.7 of the amino group, poly-L-lysine is positively charged under physiological conditions which makes it a hydrophilic polymer. The molecular weight varies from 70-150kDa (Sigma-Aldrich, Germany).

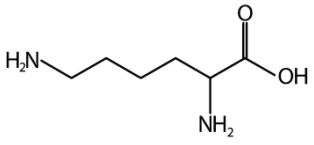

Figure 17. Chemical structure of a lysine monomer.

- Poly-D-tyrosine (PDT)
  Tyrosine (Figure 18) is also a proteinogenic amino acid, but a non-essential one. Poly-D-tyrosine is a hydrophobic polymer and cannot be dissolved in water. Again the molecular weight distribution is quite large (40-100kDa, Sigma-Aldrich, Germany).

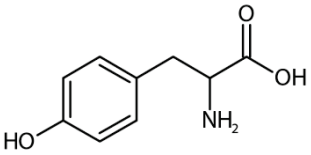

Figure 18. Chemical structure of a tyrosine monomer.

- Polyisoprene (PI)
  Isoprene (Figure 19) occurs naturally as an organic compound (for example in trees) and is also produced in large amounts in industry. Here, polyisoprene was synthesized to obtain a molecular weight of 119kDa with a thiol group at the end of the chain, to allow coupling to the AFM tip (Appendix). It is soluble in chloroform.

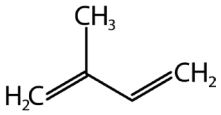

Figure 19. Chemical structure of isoprene.

- Chondroitin sulfate
  Chondroitin sulfate is an unbranched glycosaminoglycan (GAG) chain which occurs naturally in cartilage. It is composed of the alternating sugars N-acetylgalactosamine and D-glucuronate (Figure 20, over 100 units possible). Each sugar can be sulfated up to two times. Chondroitin sulfate is negatively charged at physiological conditions. Due to its high charge density (charge spacing of 1-2nm) and the resulting electrostatic repulsion, it has the ability to hold large amounts of water and to function as a compression resistant in cartilage [26].

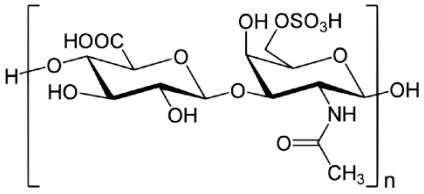

Figure 20. Chemical structure of one chondroitin sulfate unit.

3.5.2. Bottle-brush polymer - Aggrecan

Aggrecan is a proteoglycan with an average length of 400nm resembling a bottle-brush (Figure 21). It occurs naturally in cartilage. The core is composed of three globular domains (G1, G2 and G3) [60, 61]. In the region between G2 and G3 large amounts of GAG chains radiate from the protein core. They consist mainly of chondroitin sulfate. Up to 100 chondroitin sulfate chains can be attached to the core of aggrecan with a spacing of about 2-4nm. As pointed out above, chrondroitin sulfate is negatively charged and so is consequently aggrecan. In cartilage, aggrecan only occurs as an aggregate. About 100 aggrecan chains are attached non-covalently via the G1 domain to hyaluronic acid [52]. Each interaction is additionally stabilized

by the binding of a link protein both to hyaluronic acid and the G1 domain of aggrecan [61]. These large, negatively charged aggregates are trapped in the collagen network of cartilage. As mentioned above, this leads to a high osmotic pressure which draws water into the tissue and causes the cartilage to swell [60].

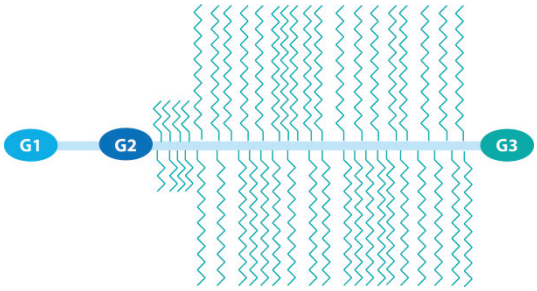

Figure 21. Aggrecan with free globular domains (G1, G2 and G3) and GAG chains radiating from the protein core between G2 and G3.

3.5.3. Graft polymers

A polyisoprene (PI) backbone was grafted with polystyrene (PS) side chains of different molecular weight (PI-*g*-PS, Figure 22):

- PI-*g*-PS(3)
- PI-*g*-PS(14)
- PI-*g*-PS(88)

The values in parentheses corresponds to the molecular weight in kDa of PS side chains. PI-*g*-PS(3) is on average grafted with 270 side chains with a spacing of 2nm, PI-*g*-PS(14) with 60 side chains with a spacing of 11nm and PI-*g*-PS(88) with 10 side chains which are separated by approximately 60nm. The graft polymers are like polyisoprene soluble in chloroform and can be coupled via a thiol group to the AFM tip. The synthesis is described in the Appendix.

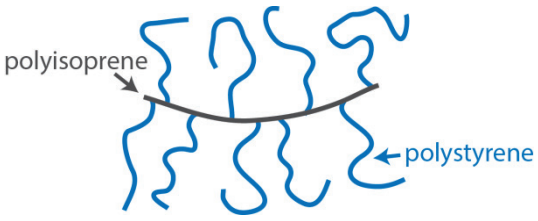

Figure 22. Scheme of the structure of a graft polymer (PI-*g*-PS(88))

3.5.4. Branched polymer – Dendronized polymer

The dendronized polymer consists of several wedge-shaped dendrons of generation four with carboxyl end groups (Figure 23, left). They are linked together at the dendrons starting point to form a linear chain (Figure 23, right). The dendronized polymer is then almost of cylindrical shape [62]. One great advantage of these dendritic structures is the high density of functional end groups due to the highly branched side chains. The synthesis is described in the Appendix.

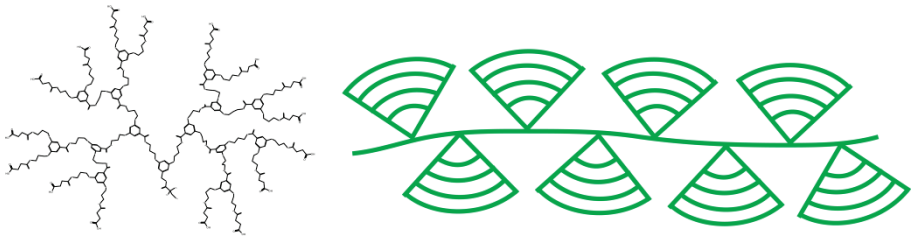

Figure 23. Left: A dendron, which reflects the monomeric unit of a dendronized polymer. **Right**: Illustration of a dendronized polymer of generation four.

3.6. Surface preparation and characterization

The surfaces used in this thesis vary from very "simple" and well defined surfaces like hydrogenated diamond to biological and very complex cartilage samples.

3.6.1. Hydrogenated diamond

A polycrystalline diamond (size: 5mm x 5mm, Element-Six, Advancing Diamond Ltd, UK) is hydrogenated by following the previously published protocol [19, 63]:

- Heating up in a vacuum chamber to 700°C
- Hydrogen flow (100sccm) started with a pressure of 10mbar and was activated by a plasma reactor (Astex)
- 15 min at a pressure of 50mbar
- Soft shut down and cooling under hydrogen atmosphere (10mbar, 100sccm)

Before the measurement the diamond is cleaned for 1h in an ultrasonic bath in acetone and isopropyl alcohol, respectively.

3.6.2. Glass slide coated with Vectabond™

The following protocol is used for the preparation of glass slides (Glaswarenfabrik Karl Hecht KG, Sondheim, Germany).

- Cleaning of the glass slide in RCA (v:v:v: 5:1:1 mixture of water, 35% H_2O_2, 32% NH_3) at 70°C for 20 min
- Rinsing in acetone (anhydrous, ≥ 99.8%, VWR)
- Incubation for 10 min in a mixture of 5ml acetone and 100µl Vectabond™ (Axxora, Lörrach, Germany)
- Rinsing in acetone
- After drying the slides in the oven, they are immediately ready for measurements

3.6.3. Gold slides and self-assembled monolayers

First, glass slides are coated with gold:

- Sonicating the glass slides for 1h in ultrapure water (Biochrom, Germany)
- Sonicating the glass slides twice for 1h in a 2% Hellmanex solution (Hellma GmbH und Co. KG, Germany)

- Cleaning of the glass slide in RCA (5:1:1 v|v|v|% mixture of H_2O, H_2O_2, NH_3) at 70°C for 15 min
- Coating with 10nm chrom-nickel and 100nm gold in a vacuum coater (Edwards GmbH, Germany)
- Storing in a refrigerator

The gold slides are either directly used for measurements or a hydrophobic self-assembled monolayer is additionally applied:

- Cleaning of the gold slide in RCA (v:v:v: 5:1:1 mixture of H_2O, H_2O_2, NH_3) at 70°C for 15 min
- Rinsing with ethanol (>99.9%, Merck, Germany)
- Rinsing with water
- Incubation of the gold slides in a mixture of 20ml ethanol and 1-dodecanthiol (Sigma Aldrich, Germany) with a final concentration of 2mM for 12h
- Rinsing with water
- After drying the slides under a nitrogen stream, they are immediately ready for measurements

3.6.4. Cartilage samples

The cartilage samples are harvested from the knee joint of the hind legs of either lambs (3-6 months old) or elderly sheep.
The lamb joints are obtained from the local butcher and stored in a freezer for at least one day. It is important to note that it is always made sure that the joint capsule is still intact, so no fluid can leave the capsule and drying of the cartilage is avoided. At the day before the measurements, the lamb joints are put in a refrigerator to allow slow defrosting. Prior to the experiments, the joint capsule is opened and the cartilage samples are prepared.
The samples from elderly sheep are prepared from freshly slaughtered animals and frozen afterwards in PBS solution.
The preparation procedure used for both lamb and sheep is illustrated in Figure 24:

First, the joint is fixed at the bench with a bench vice and the capsule is opened with the help of a scalpel. Here, it is always ensured that the cartilage appeared as a glossy, whitish and smooth surface, which indicates healthy tissue. Especially for sheep, the cartilage often appears yellowish and blunt. Afterwards cylinders are drilled and sawed out of the patellar groove region of the joint. The diameter of the cylinders is 5mm for AFM measurements and 10mm for the tribometer experiments. One reason for choosing the patella is the relatively smooth surface. This is important for the friction measurements, so no artifacts occur due to a curved surface or high edges which interfere with the cantilever. The cartilage samples are then stored in a refrigerator and wrapped in meat to keep them hydrated. Right before the experiment, the cylinders are cut to the right height so they fit in the home-built fluid cell (for AFM measurements) or in the tribometer.

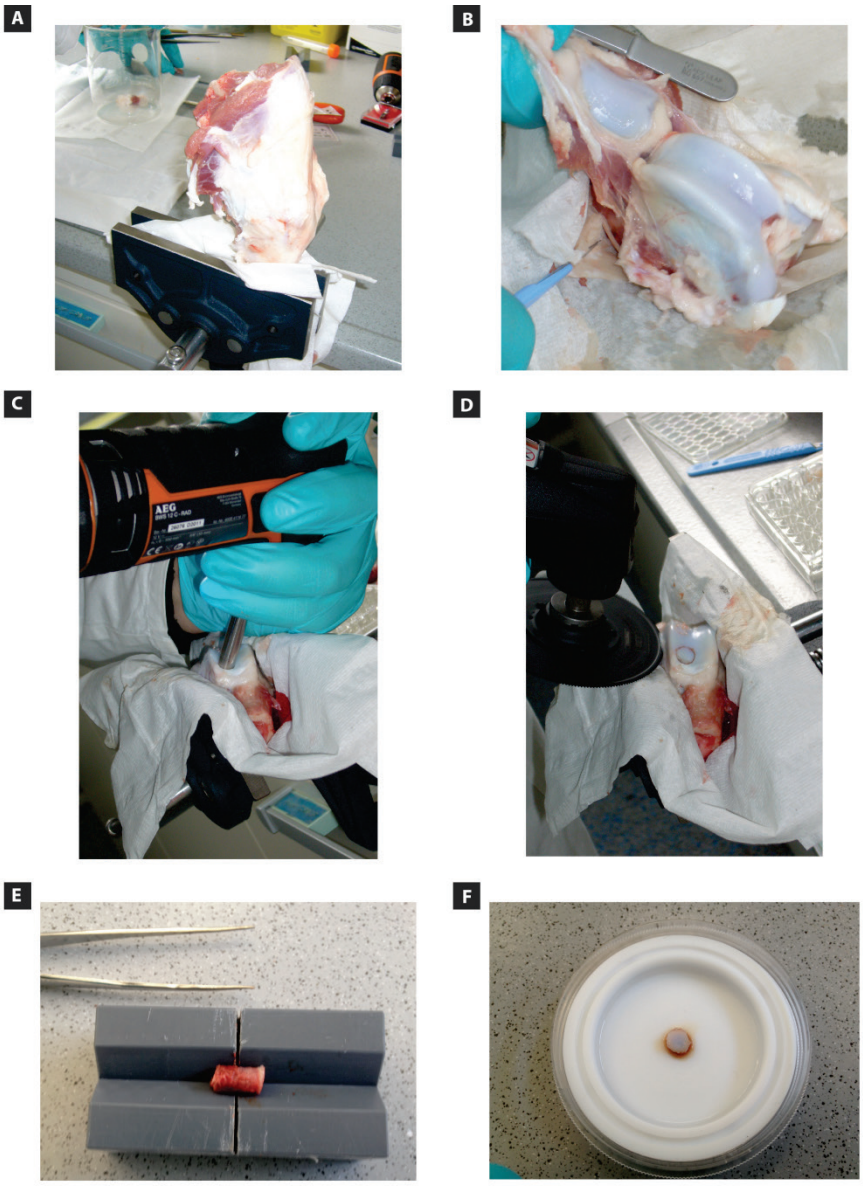

Figure 24. Preparation of cartilage samples from the hind leg of a lamb. (**A**) The leg is fixed in a bench vice and (**B**) opened with a scalpel. (**C**) Cylinders with a diameter of 5mm are drilled out of the patella groove and (**D**) sawed. (**E**) The cylinders are cut to the right height and (**F**) put into a hole in the middle of a home-built fluid cell. The pictures are courtesy of Lorenz Wiegleb.

3.6.5. Characterization of solid surfaces

Before each measurement, the solid surfaces have to be characterized with respect to their hydrophobicity. Therefore, the contact angle Θ between a tangent to a water droplet and the surface is determined. For every surface, the contact angle between a 1.5µl water droplet and the surface is measured five times and averaged. The evaluation is done with a home-built goniometer which is equipped with a CCD camera. The images are analyzed with the drop-analysis plug-in for ImageJ [64]. First, the boundary of the droplet is marked with a polynomial and then the contact angle is determined from the tangent to the droplet. The average contact angles are 75° for diamond, 83° for glass slides coated with Vectabond™ and

112° for the self-assembled monolayer. This means that all surfaces are rather hydrophobic with the SAM being the most hydrophobic one. The main reason for choosing hydrophobic surfaces over hydrophilic ones is the higher attraction of the polymers used in this work to hydrophobic surfaces. The more hydrophilic the surfaces, the fewer events can be observed in single molecule adhesion and friction experiments [61].

3.6.6. AFM imaging of surfaces and determination of their roughness

To further characterize the surfaces, contact mode AFM images are obtained. The tip is brought into contact with the surface until a defined normal force is applied to the surface. Then the surface is scanned with 1Hz while keeping the normal force constant. Both, trace and retrace are recorded. Afterwards the root mean square roughness of the images is determined.

For fresh and rehydrated cartilage samples, cantilevers with a low spring constant are chosen (MLCT, Bruker AFM Probes, Camarillo, USA) to not destroy the structure. The measurements are performed in liquid. For the solid surfaces, the glass slide coated with Vectabond™ , the diamond surface and the dehydrated cartilage stiffer cantilevers are used (CSC37 cantilever, Mikromasch, Wetzlar, Germany) and all images are recorded in air.

4. Temperature dependent single molecule desorption

This chapter is based on the following two publications of the author:

Kienle et al. "*The Effect of Temperature on Single-Polypeptide Adsorption*" ChemPhysChem 2012 [19]
Kienle et al. "*Measuring the interaction between ions, biopolymers and interfaces – one polymer at a time*" Faraday Discussions 2013 [13]

In each biological system proteins are one of the major functional constituents. Therefore it is essential that these proteins work properly. One basic requirement is the correct fold. Failure to fold or misfolding of proteins leads for example to the formation of amyloids, which can cause degenerative diseases like Alzheimer's disease. Each protein consists of a unique amino acid sequence. Anfinsen showed by folding and unfolding proteins with urea that the sequence of the amino acids determines the correct fold. They interact with one another and fold spontaneously into the protein's native form [65].
The fold of a protein can be altered by changing external factors like temperature [66-70]. High (heat denaturation) [6] and low temperatures (cold denaturation) [71] cause unfolding of a protein. This induces a maximum in the free energy which can be rationalized by the interplay of different contributions to the solvation of hydrophobic residues during unfolding: With increasing temperature, the entropic cost decreases while the enthalpic cost increases. Much effort was made to investigate the temperature dependence of protein folding not only experimentally, but also on a theoretical level. Up to now the folding process and its temperature dependence are not completely understood and predictable. One limitation is the inability to perform simulations with reasonably sized complex proteins. Another problem is that not all forces driving the folding process are known. However hydrophobic attraction was identified as one of the main forces in the process of protein folding [72]. Therefore, a lot of effort was made to understand the temperature dependence of hydrophobic attraction to gain more insight into protein folding, but the knowledge is still incomplete. Most experimental data sets were obtained by studying the hydration of small hydrophobic particles. They follow the same temperature dependent behavior as proteins, namely a maximum in free energy [73, 74]. In 1974, Privalov believed that with the experimental discovery of entropy convergence, the proof was found for the hydrophobic collapse being the main driving force in the folding process [75]. Although it was recently shown, that the hydrophobic attraction alone could not be sufficient to explain protein structure and stability, it is without doubt an important contribution to the folding process [74].

As pointed out above, it is not yet possible to perform simulations with reasonable sized proteins. Therefore a different approach was chosen in this work to investigate hydrophobic attraction. Results from AFM-based single molecule force spectroscopy experiments were compared to molecular dynamics simulations. With both approaches, the temperature dependence of the free energy needed to pull single polymers off of different surfaces into solution can be probed. Horinek et al. showed that peptide adsorption can indeed be studied using molecular dynamics simulations and the results are comparable to experimental data

[18]. The simulations allow further to gain additional insight into the details of the desorption process. The setup for both, AFM measurements and simulations was chosen in a way, that the only force acting between the single polymer and the surface was hydrophobic attraction. The surfaces are neither able to from hydrogen bonds nor are they charged. This approach allows to close the gap between the solvation of small hydrophobic particles and larger folded proteins and link insights from temperature dependent desorption measurements to hydrophobic attraction.

4.1. Dependence on polymer and surface characteristics

First AFM-based single molecule force spectroscopy experiments were performed. Either a hydrophilic (poly-L-lysine) or a hydrophobic polymer (poly-D-tyrosine) was coupled covalently to the AFM tip. Force-distance curves were performed in water at temperatures ranging from 299K (25°C) to 348K (74°C). A hydrogenated diamond was used as a surface. The interaction between the polymers and the surface were only caused by hydrophobic attraction as e.g. no formation of hydrogen bonds could occur. For poly-L-lysine, furthermore measurements on a glass slide coated with the aminosilane Vectabond™ were performed. For each temperature at least 100 force-distance curves were recorded with a constant velocity of 1µm/s and a dwell time of 1s on the surface. The same cantilever was used for all temperatures to avoid uncertainties due to the calibration of the spring constant. The deviations caused by the determination of the spring constant are then only around 2%.

The height of the plateaus of constant force (plateau force) and also the length (detachment length) were determined by a fit with an s-curve. The free energy ΔG was calculated by multiplying the measured plateau force with the length of one monomer (0.36nm). Only interactions of a single polymer with the surface were taken into account. This was associated with a single step detachment to the baseline in the measured force (see Figure 12 and chapter 3.2 for details). The obtained values were plotted in a histogram and fitted with a Gaussian. The maximum of the Gaussian together with the standard deviations are then plotted together with ΔG in dependence of the temperature. The results obtained for poly-D-tyrosine (red) and for poly-L-lysine on diamond (light blue) and on glass coated with Vectabond™ (dark blue) are shown in dependence of the temperature in Figure 25A.

Measurements with poly-D-tyrosine did not show a significant effect of temperature on the free energy, neither a maximum nor a minimum can be observed. The results obtained with poly-L-lysine on diamond reveal only a very weak temperature dependence with a slight minimum in the free energy. On the glass slide coated with Vectabond™, again only a weak temperature dependence of the plateau force could be found, but in this case with a slight maximum in free energy. The comparatively large deviations at low temperatures are still within the error of the measurements.

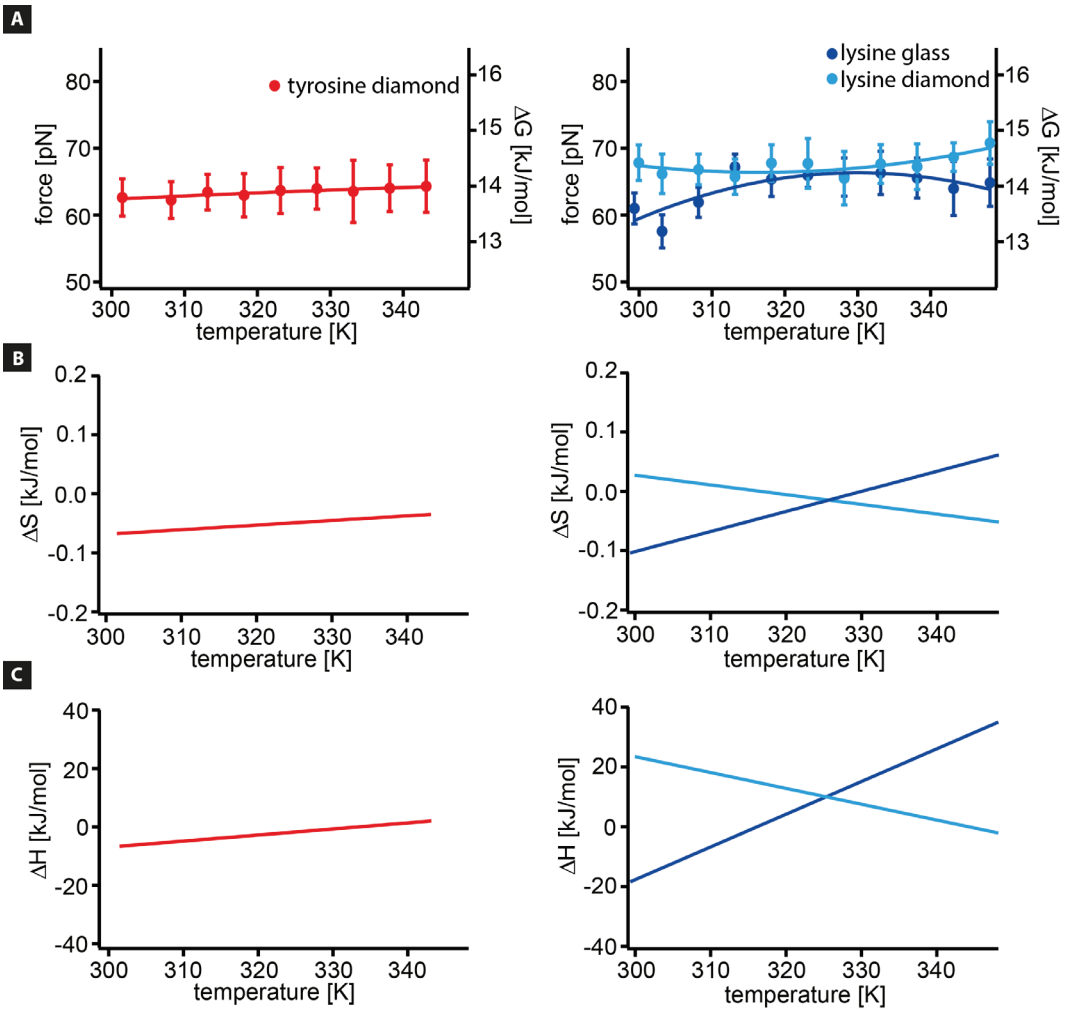

Figure 25. (**A**) Plateau force and free energy per monomer ΔG for poly-D-tyrosine on hydrogenated diamond (red), for poly-L-lysine on hydrogenated diamond (light blue) and on a glass coated with Vectabond™ (dark blue). Furthermore changes of (**B**) entropy ΔS and (**C**) enthalpy ΔH with temperature are shown. All measurements were performed in water.

It is also possible to gain further information about other thermodynamic parameters like the entropy change ΔS and the enthalpy change ΔH per amino acid. Therefore ΔG was fitted with a parabola. Many different analytical fit functions could be chosen to fit the results, but using the parabola allows best to compare the results to the solvation free energy of nonpolar particles. The parabolic fit of the results obtained with poly-D-tyrosine on hydrogenated diamond resulted in almost no curvature. For poly-L-lysine either a slight minimum for measurements on diamond (Figure 25A, light blue) or a maximum for measurements on the glass slide (Figure 25A, dark blue) were observed. ΔS was then determined by differentiating ΔG using equation (13) (Figure 25B). Both an increase in entropy with increasing temperature (poly-D-tyrosine on diamond and poly-L-lysine on glass) and a decrease (poly-L-lysine on diamond) was observed. The same holds true for the enthalpy change ΔH, which was calculated with equation (14) (Figure 25C). The changes in entropy and enthalpy, however, are small and for poly-D-tyrosine even negligible.
A possible explanation for the different curvertures measured with poly-L-lysine on the two surfaces could be the surface roughness (Figure 26).

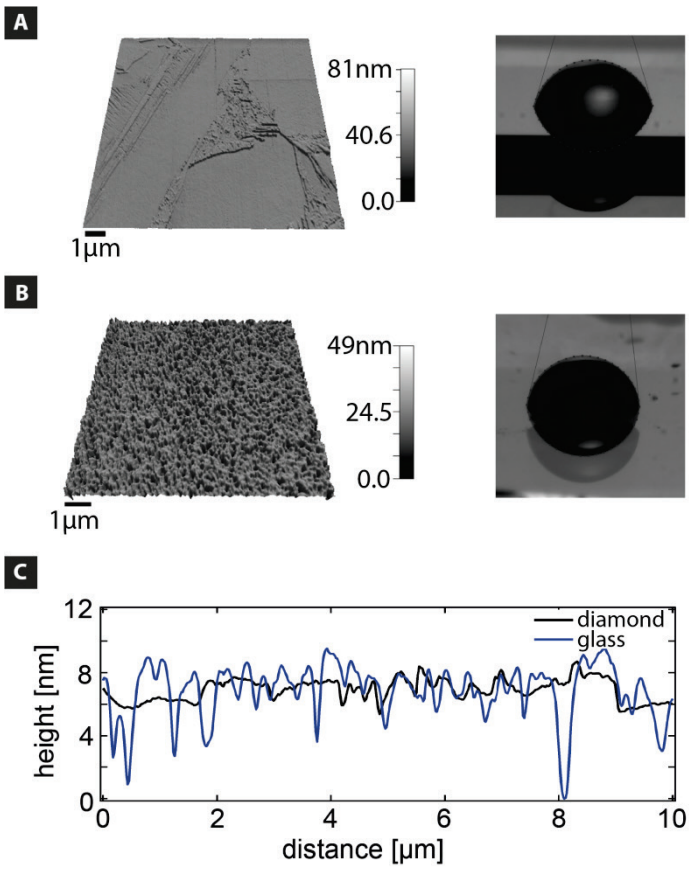

Figure 26. Contact mode image with the corresponding contact angle measurement for (**A**) hydrogenated diamond and (**B**) glass coated with Vectabond™. (**C**) Sections obtained from the contact mode images for diamond (black) and glass (blue). Adapted from [19].

Both surfaces were hydrophobic with an average contact angle of 75° and 83° for diamond and the glass slide, respectivly. Additionally, contact mode images were recorded (Figure 26). The average surface roughness obtained from those images, did show a mean roughness of 0.6nm for diamond and 1.6nm for the glass slide. A section of both surfaces is shown in Figure 26C for reference. The surfaces were similar in terms of hydrophobicity, but differed in the chemical composition and slightly in the roughness. Measurements with poly-L-lysine on the surface with the higher roughness (the glass slide) led to a maximum in free energy, while measuring on the surface with lower roughness (diamond) to a minimum.

As pointed out above not only the height of the plateaus, but also the detachment length was determined. Although one and the same cantilever was used for the whole experimental set, the distribution of the measured detachment lengths was very broad. This means that during the measurements not only one polymer could interact with the surface, but several in an alternate manner. For this reason, the influence of temperature on the detachment length could not be determined for the whole temperature range, but only for two individual temperatures for which the interactions of the polymers with the surface resulted in discrete peaks (Figure 27). These results show that there is, similar to the plateau force, no dependence of the detachment length on temperature.

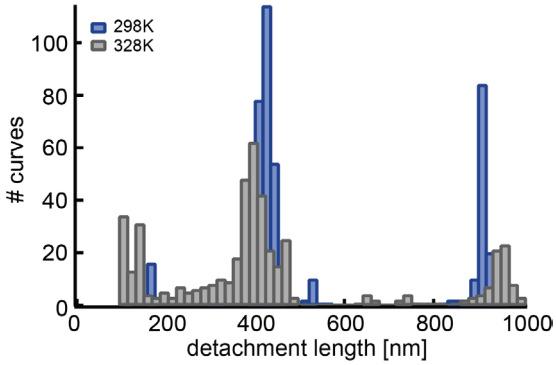

Figure 27. Temperature dependence of the detachment length for poly-L-lysine on hydrogenated diamond in water. Adapted from [19].

4.2. MD simulations and contributions to the temperature dependent desorption

The experimental results were compared to molecular dynamics (MD) simulations to gain further insight into the details of the temperature dependent desorption process. The simulations were performed by Susanne Liese in the group of Roland Netz. Two different surfaces were simulated: A self-assembled monolayer (SAM) and, like in the experiments, a hydrogenated diamond. The SAM had a contact angle of 117° and the hydrogenated diamond 121°. Here again the roughness of the surfaces was determined. Therefore, the spatial variation of water density parallel to the surface was plotted (Figure 28) by dividing the simulation box in 200 slices parallel to the y-z plane. The density profile on the SAM (black curve) is rough, but with a regular pattern. The profile found on the hydrogenated diamond surface (grey curve) is smoother with narrower peaks. The peak position indicates the position of the outermost surface atoms.

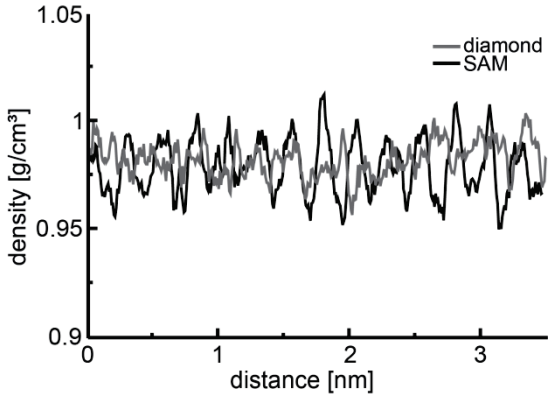

Figure 28. Density profile at the surface of a hydrophobic SAM (black) and a hydrogenated diamond (grey) (from MD simulations performed by Susanne Liese). Adapted from [19].

The standard deviation of the mean density was calculated for both surfaces and was used as a measure for the roughness. For the SAM a value of 15 mg/cm³ and for diamond 13mg/cm³ were determined. Consequently similar to the experimental setup, surfaces with a similar hydrophobicity, but different chemical composition and roughness were used.

Ideally the same polymers as in the AFM measurements, namely poly-L-lysine and poly-D-tyrosine, would be used for the simulations. These systems, however, were not ideal for simulations. With poly-D-tyrosine aggregation effects were observed. Substrates with different roughness resulted in different adsorption behaviors for poly-L-lysine. This together with the complicated charge-regulation effects of charged polypeptides on surfaces [76] made poly-L-lysine and poly-D-tyrosine not an ideal system to study the hydrophobic attraction in simulations. Therefore, the simplest polypeptide, polyglycine, was chosen for the MD simulations. This approach then allowed to test the universality of the experimental results.
Both dynamic and static simulations were performed with the dynamic ones being similar to AFM experiments: First, the polymer was pushed to the surface. Then, the polymer was moved away from the surface with a constant velocity by applying a harmonic potential to the first monomer. If the force was strong enough, the polymer was desorbed. The force-distance curves resulted in a plateau of constant force with a sudden drop to zero after the detachment of the polymer. The main difference compared to AFM measurements was, that the constant pulling velocity was five orders of magnitude higher (0.1m/s). To further study a desorption process close to equilibrium, additional static simulations were performed. Here, the origin of the potential was held at a fixed position above the surface with a grid of 0.2nm. The system configurations were extracted from the dynamic simulations.

The results of the MD simulations are summarized in Figure 29. On both surfaces the dependence of the plateau force on temperature was only weak (except for a temperature of 300K). Although the absolute values for force and free energy were lower as compared to the AFM measurements, the qualitative observations agree. On the slightly rougher surface (SAM), the parabolic fit resulted in a slight maximum and on the smoother surface (diamond) in a minimum, which led to both an increasing and a decreasing entropy ΔS and enthalpy ΔH. The same behavior was observed experimentally.

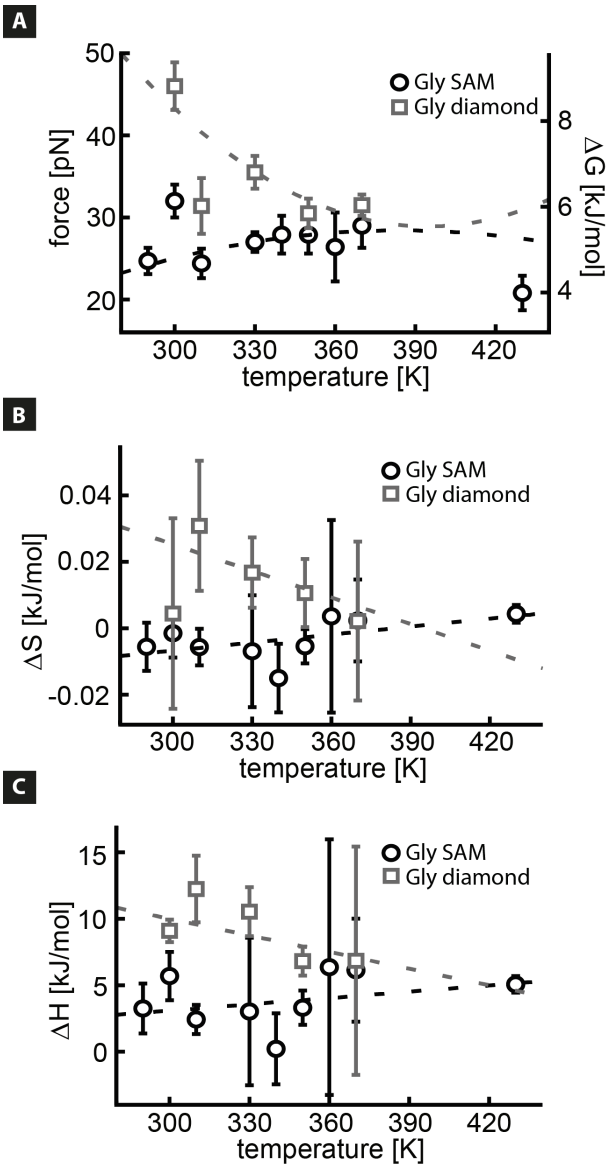

Figure 29. (**A**) Dependence of the plateau force and free energy on the temperature for polyglycine on hydrogenated diamond (grey) and on a hydrophobic SAM (black). (**B**) Corresponding entropy ΔS and (**C**) enthalpy change ΔH with temperature. The results were obtained from molecular dynamics simulations with polyglycine and performed by Susanna Liese in the group of Roland Netz. Adapted from [19].

The great advantage of simulations was that not only the different thermodynamic parameters (ΔG, ΔS and ΔH) could be extracted, but also the different contributions to the desorption process. Therefore the difference in enthalpy ΔH between the state where the polymer was completely adsorbed to the surface and the state where the polymer was completely stretched, but not yet detached, was determined (inset in Figure 30A). The resulting enthalpy change ΔH and the free energy change ΔG arose from interactions of the polypeptide (P), water (W) and the surface (S) with one another. The results are shown for simulations with polyglycine on both diamond (Figure 30A) and SAM (Figure 30B) for different temperatures (bars with different colors). Although individual interactions like water-water and polypeptide-water were quite large, the total change in free energy was much lower. This was due to a cancelling out of the different interactions.

Altogether the MD simulations supported the results drawn from experiments that no universal temperature dependence could be observed and that the detailed contributions to the peptide-surface interaction are important.

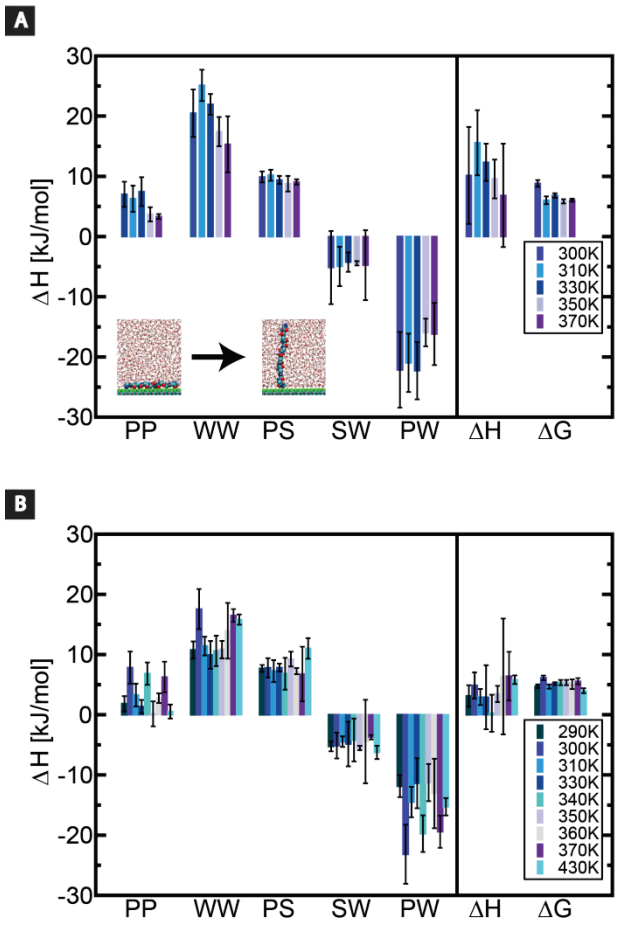

Figure 30. Enthalpy difference ΔH between the adsorbed and the stretched configuration of the polymer (see inset in (**A**)) for different temperatures on (**A**) diamond and (**B**) SAM. The total enthalpy ΔH and the free energy ΔG arose from the sum of the interactions of polypeptide (P), water (W) and the surface (S) with one another. The results were gained from molecular dynamics simulations of polyglycin and performed by Susanne Liese in the group of Roland Netz. Adapted from [19].

4.3. Solvent effect

To further probe the temperature dependence experimentally, measurements were performed after the addition of solvents to the solution. With this approach solvent specific effects could be tested. Figure 31A again shows results for poly-D-tyrosine in water on hydrogenated diamond (red). Furthermore the black squares represent the results for measurements in 7% ethanol instead of water. The measurements were performed with the same cantilever. What is immediately obvious is a lower absolute desorption force for measurements in ethanol. This could be rationalized by the change in interfacial energy (see chapter 2.3.2). Despite the lower desorption force, only minor changes in force and free energy were observed with increasing temperature. The same holds true for measurements in 50mM NaCl (Figure 31B).

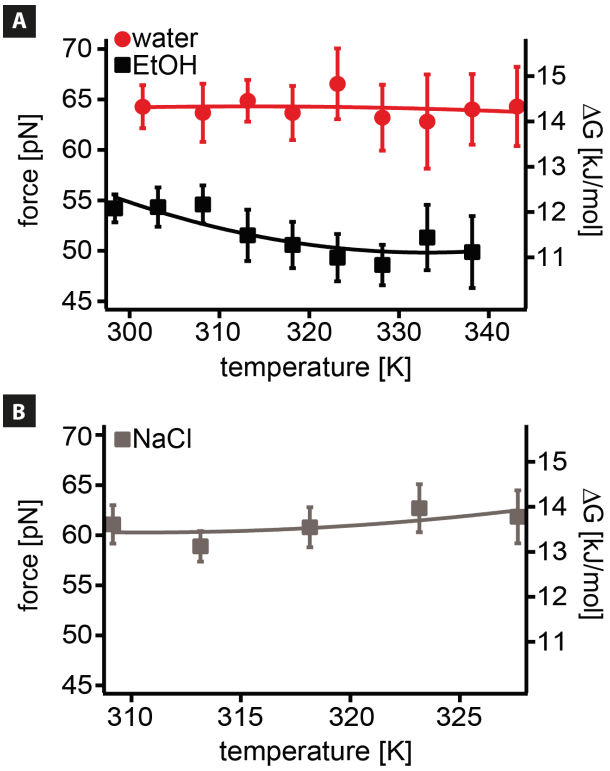

Figure 31. Temperature dependence of the plateau force and the free energy ΔG measured with poly-D-tyrosine on hydrogenated diamond in (**A**) water (red) and 7% EtOH (black) and in (**B**) 50mM NaCl. Adapted from [13].

This is another indicator that the desorption of polypeptides is not sufficient to understand the dominating forces in protein folding, because folding of proteins depends largely on solvents and their concentration.

4.4. Conclusion

Both proteins and small hydrophobic particles show a maximum in the temperature dependent free energy. Therefore, the hydrophobic attraction, which dominates the solvation of small hydrophobic particles, was believed to be the main driving force in protein folding. Here, a new combined experimental and simulation approach was used to study the temperature dependence of hydrophobic attraction. The experimental and simulation setup was chosen in a way that the interaction between the polymers and the surfaces can only be associated with hydrophobic attraction. Only a very weak temperature dependence was observed. Furthermore, on the rougher surface a weak maximum and on the smoother surface even a minimum in free energy was observed experimentally and in MD simulations. This is in contradiction to the known temperature dependent free energy of proteins and also of small hydrophobic particles. The results suggest that the hydrophobic interaction between a single polymer and a surface is governed by a mechanism that differs from the solvation of small hydrophobic particles and that protein folding is not only dominated by the hydrophobic attraction.
The small variations observed here can be explained by a mutual compensation of different contributions to the total interaction (Figure 30). Consequently, the desorption process of a single polypeptide can be considered much more complicated than the solvation of simple

particles as it depends on the peptide-surface interactions, but also on the structure of the interfacial water.
In protein folding processes, large entropic and enthalpic contributions compensate each other, but still a strong dependence of the free energy on temperature is observed. Together with the results presented above, this indicates that neither the solvation of small hydrophobic particles nor the desorption of polypeptides from surfaces is sufficient to understand the driving forces in protein folding.

5. Effect of single polymer architecture on single polymer adhesion and friction

This chapter is based on the following publication of the author:

Kienle et al. "*Effect of Molecular Architecture on Single Polymer Adhesion*" Langmuir 2014 [77]

A lot of effort was and is still made to develop coatings with well-defined properties [78], for example to prevent biological material to adhere to different surfaces. This process is called biofouling and has a huge impact on the shipping industry [79], but also on the development of medical implants [80].
The main goal is to avoid adhesion of proteins. Therefore the coating must be stable, homogenous and well connected with the surface. Additionally the layer must be thick enough to shield any attraction arising from the surface [81, 82].
One approach is to use linear polymers with different functionalities. As poly(ethylene) glycol (PEG) is well known for its protein resistant behavior, surfaces were coated with linear PEG chains [83]. Not only linear chains or block copolymers are used, with other polymer architectures promising results were also achieved. One possibility to further improve protein resistance is to use a graft polymer based on the anti-fouling properties of PEG. Therefore, linear PEG chains were grafted to a linear poly-L-lysine (PLL) backbone [84]. PLL enables physisorption of the graft polymer to charged surfaces. The attachment to surfaces like metallic oxides can be realized by using for example biomimetic groups like 3,4-dihydroxyphenylalanine (DOPA) [85]. Recently other more sophisticated architectures were developed to further improve these coatings. Prominent examples are dendritic structures like dendrimers [86-88] and dendronized polymers [89]. The great advantage of these polymers is the high density of functional end groups due to the branched nature of their side chains, potentially leading to stronger adsorption due to the larger number of possible interaction sites with the surface as compared to just linear chains.

As has been just described, changing the polymer architecture affects the properties of coatings. The underlying molecular mechanisms of the interaction of single polymers with different architectures to a surface, however, have not yet been studied. Here single molecule force spectroscopy and single molecule friction force microscopy were used to compare adhesion and mobility of linear chains to graft, bottle-brush and branched polymers (Figure 32).
Linear polymer chains have already been the subject of extensive studies. Their interaction with as well as their mobility on various substrates was probed. Examples are hydrophilic and hydrophobic polymers [13, 19, 82], a spider silk motif [90] and polystyrene [82]. The adhesion properties on surfaces with varying hydrophobicity [15, 91] or on surfaces covered with polymer films were analyzed [82]. The effect of temperature (as described in chapter 4) [13, 19], salt concentration, pH and co-solutes were investigated [17]. It is noteworthy that if an effect was observed, the changes were only small (around a factor of two).

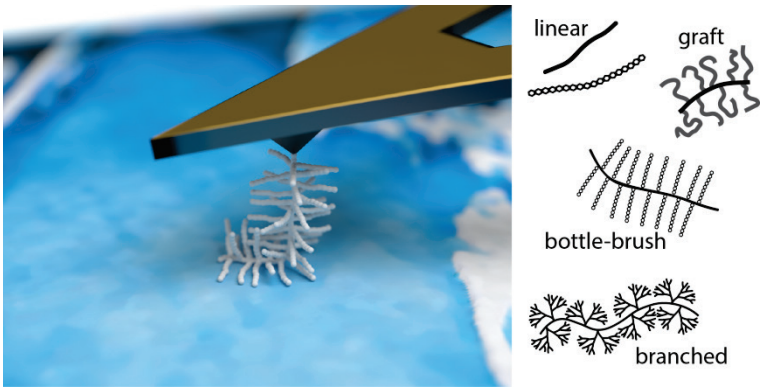

Figure 32. Left: Tip of an AFM cantilever with a single polymer attached to it. **Right**: Schematics of the different polymer architectures used.

All measurements shown in the following were performed on one surface, namely a hydrophobic, hydrogenated diamond. None of the polymers investigated in this study can interact specifically with the diamond substrate. The formation of hydrogen bonds and ionic interactions are not possible, thus only unspecific interactions were probed. This allows to separate the influence of the polymer architecture from e.g. the chemical composition of the polymers.

5.1. Polyisoprene based graft polymers

First, single molecule force spectroscopy experiments with a linear polyisoprene chain (PI) were performed and compared to results obtained with graft polymers (see schematics in Figure 32 on the right). For the graft polymers, polystyrene (PS) side chains of different molecular weight (3kDa, 14kDa and 88kDa) were attached to a polyisoprene backbone (119kDa). This results in three different graft polymers: PI-*g*-PS(3) with approximately 270 PS side chains per PI backbone, PI-*g*-PS(14) with 60 PS side chains and PI-*g*-PS(88) with 10 PS side chains per PI backbone. The entanglement length for PS is on the order of 18kDa [92]. Therefore it was possible to compare side chains which should not entangle with one another (3kDa), side chains which are in the region of the entanglement length (14kDa) and side chains that could form entanglements (88kDa).
For all the experiments water was used as a solvent. As water is a non-solvent for PI and for PS, the adhesion to the surface should be enhanced. Experiments with a good solvent, namely chloroform, were also performed, but no significant difference in the characteristics of the force-distance curves was observed as compared to water.

In Figure 33 typical force-distance curves for PI and the graft polymers PI-*g*-PS are shown. Both, plateaus of constant force and rupture events were observed with all polymers. As shown before, plateaus of constant force occur if the polymer is mobile on the surface or can at least be desorbed from the surface, while rupture events indicate that the polymers are immobile. If a constant force plateau appeared, an s-curve fit was used to determine the height of the plateau (plateau force) and the length of the plateau (detachment length). In the case of rupture events, the maximal rupture force was determined. In all measurements, the first peak in the force-distance curves, which corresponds to the unspecific interaction of the AFM tip with the surface, was (if present) neglected.

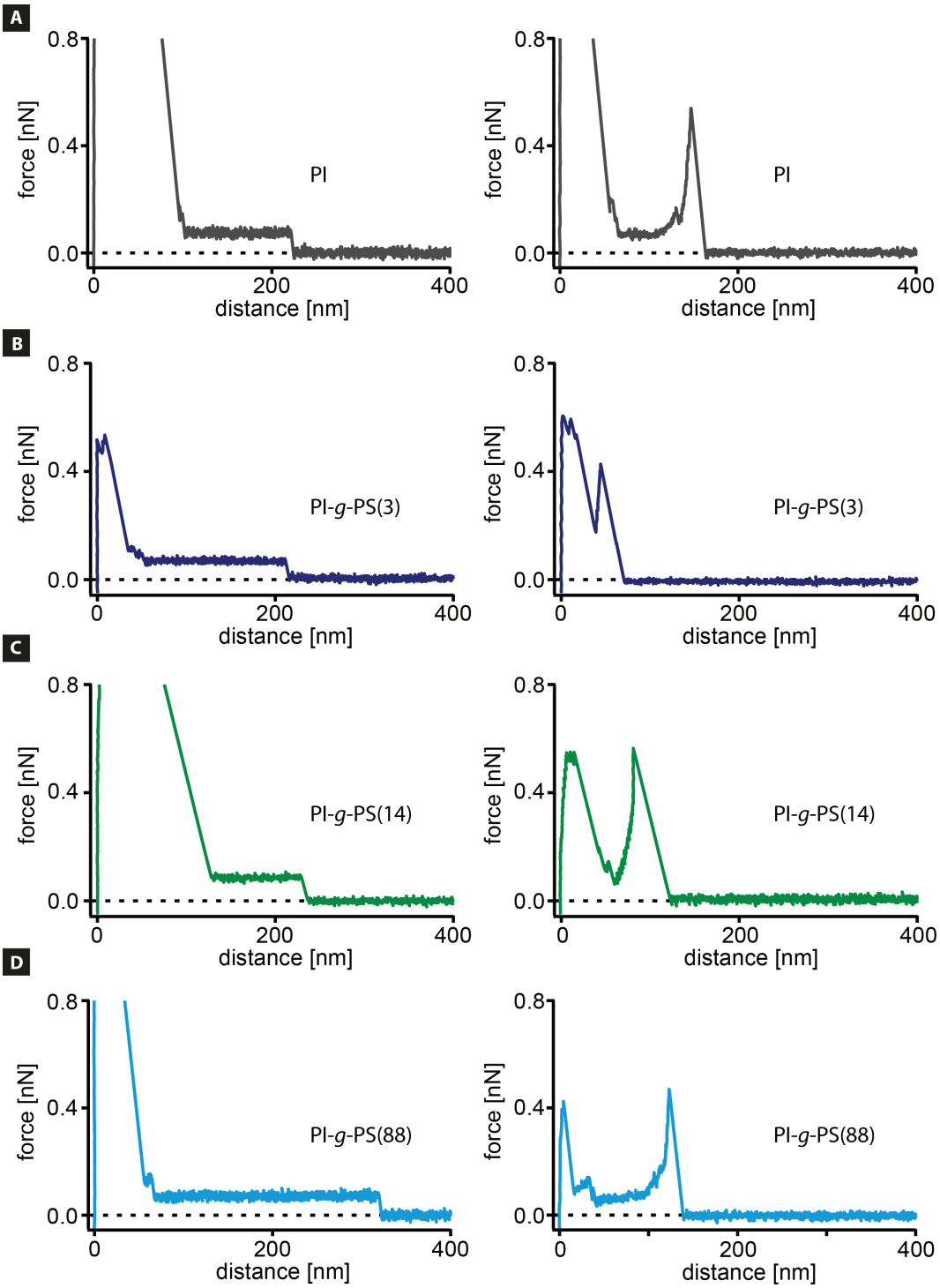

Figure 33. Exemplary force-distance curves for (**A**) PI, (**B**) PI-*g*-PS(3), (**C**) PI-*g*-PS(14) and (**D**) PI-*g*-PS(88) in water on hydrogenated diamond at room temperature showing plateaus of constant force (left) and rupture events (right).

For all polymers plateaus of constant force occurred more frequently (Table 1). In Figure 33 only force-distance curves with a single step in force are shown. This corresponds to the desorption of a single polymer from the surface. Multiple steps would correspond to the simultaneous desorption of several strands (see 3.2 for details). During the desorption of graft polymers, an accumulation of this step wise desorption process was expected compared to PI, because the backbone and the side chains could interact simultaneously with the surface. This, however, was not observed. Furthermore the plateau forces and the

detachment lengths were also not affected by the presence of side chains (Figure 34A and B). In one experiment with PI-*g*-PS(88) detachment lengths above 1000nm were observed, but this was the exception. The variations between the different types of polymers are on the same order as the variations for a single sort of polymer.

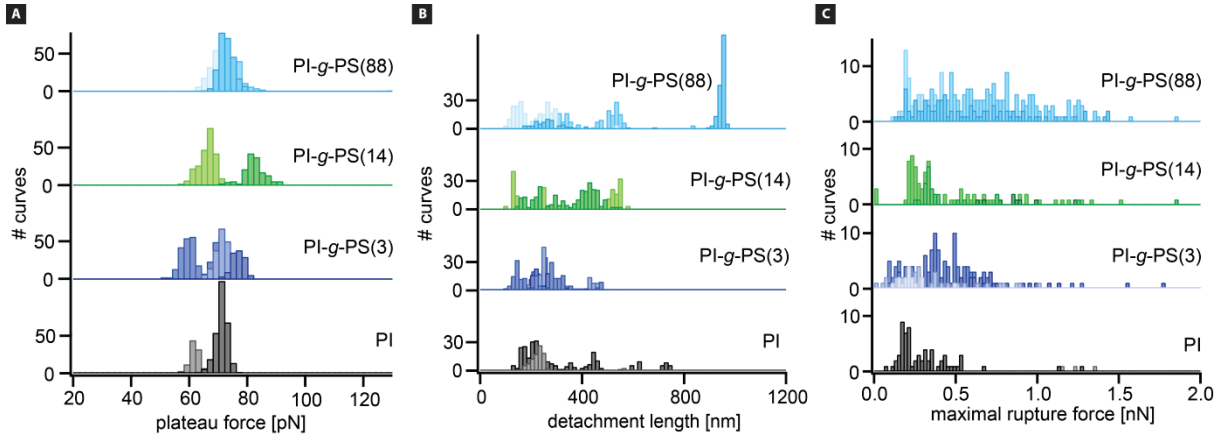

Figure 34. (**A**) Plateau force, (**B**) detachment length and (**C**) maximal rupture force for measurements with polyisoprene and polyisoprene grafted with polystyrene side chains of different molecular weight. **A** and **C** adapted from [77].

The velocity of the force-distance curves, the dwell time at the surface and the temperature of the solution were varied while measuring with PI-*g*-PS(14), but like observed with linear chains, the parameters did not influence the plateau force (Figure 35).

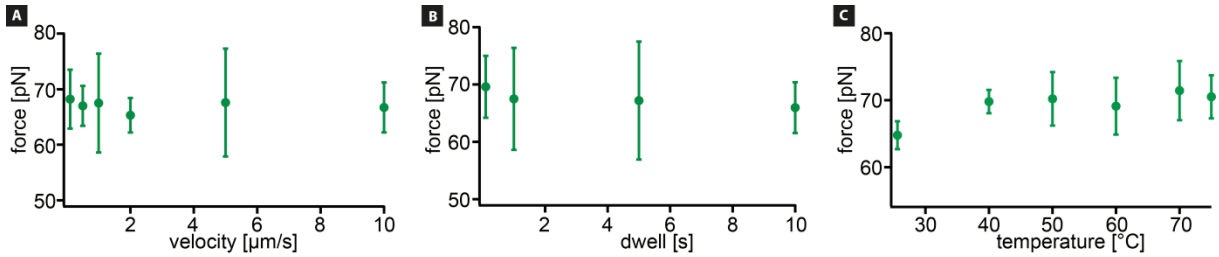

Figure 35. (**A**) Velocity, (**B**) dwell time and (**C**) temperature dependence of the plateau force for measurements with PI-*g*-PS(14) in water on hydrogenated diamond.

The characteristics of plateaus of constant force like the occurrence of a step wise desorption process and the dependence on velocity, dwell and temperature remain completely unchanged when measuring with graft polymers instead of linear ones.
Like pointed out above, not all curves showed plateaus of constant force, but in 12-34% of the curves rupture events or a combination of the plateaus of constant force and rupture events were observed (Table 1).

	plateaus	rupture events	# curves
PI	79%	21%	789
PI-*g*-PS(3)	88%	12%	1528
PI-*g*-PS(14)	87%	13%	1676
PI-*g*-PS(88)	66%	34%	1803

Table 1. Occurrence of plateaus and rupture events in force-distance curves, together with the total number of curves, performed with PI and PI-*g*-PS on hydrogenated diamond.

The maximal rupture force increased slightly with increasing molecular weight of the side chains (Figure 34C). The same holds true for the occurrence of rupture events (Table 1). An explanation for this could be the entanglement length. 88kDa is much higher than the entanglement length of PS (18kDa). Therefore, the side chains can interact and entangle with one another. This leads to the formation of a self-entangled polymer bundle. Such a bundle, with high intra-chain interactions, is not as mobile on the surface as a polymer bundle without entanglements. The reduced mobility could lead to a stronger interaction with the surface, which consequently increases the occurrence of rupture events and causes higher rupture forces.
Altogether the results suggest that the adhesion is not significantly enhanced until many polymers interact not only with the surface, but also with one another for example in the form of entanglements. Such cohesion might then result in stronger adhesion to the surface. This might explain why cross-linking helps to improve polymer films [93].

To sum up, one can say that the characteristics of plateaus of constant force are completely unaffected by the addition of side chains. Only measurements with a graft polymer with side chains above the entanglement length (PI-*g*-PS(88)) increase the occurrence of rupture events and lead to a higher maximal rupture force. The formation of a polymer bundle with strong intra-chain interactions caused by entanglements is thus one way to enhance the interaction with a surface.

5.2. A naturally occurring bottle-brush polymer

After investigating graft polymers, a natural occurring linear sugar chain (chondroitin sulfate) is compared to a bottle-brush polymer (aggrecan) (see schematics in Figure 32 on the right). Chondroitin sulfate is a linear sulfated glycosaminoglycan chain composed of alternating sugars and is highly negatively charged at physiological conditions. The side chains of aggrecan are mostly chondroitin sulfate chains with a length of about 40nm and a spacing of 2-3nm. Like chondroitin sulfate, aggrecan is negatively charged [61]. Both polymers occur naturally in cartilage and are responsible for the interstitial fluid pressurization. For more details see 3.5.

Again, force-distance curves were performed on hydrogenated diamond in a water based solution (here: PBS). Typical curves are shown in Figure 36A and B. In contrast to PI and PI based graft polymers, the main motif was not a plateau of constant force, but rupture events. In less than 8% of the curves, plateaus of constant force were observed, which is a first indication for a low mobility of the polymers on the surface.

The maximal rupture forces were determined for aggrecan and chondroitin sulfate in dependence of the velocity (Figure 36C). With increasing velocity the maximal rupture force increases. This is consistent with literature on the velocity dependent rupture force for e.g. DNA [9]. Especially at high velocities, the maximal rupture force for aggrecan is higher compared to chondroitin sulfate. Measurements with aggrecan also resulted in considerably more evaluable events (85%) in contrast to chondroitin sulfate, where only 64% of the curves showed events.

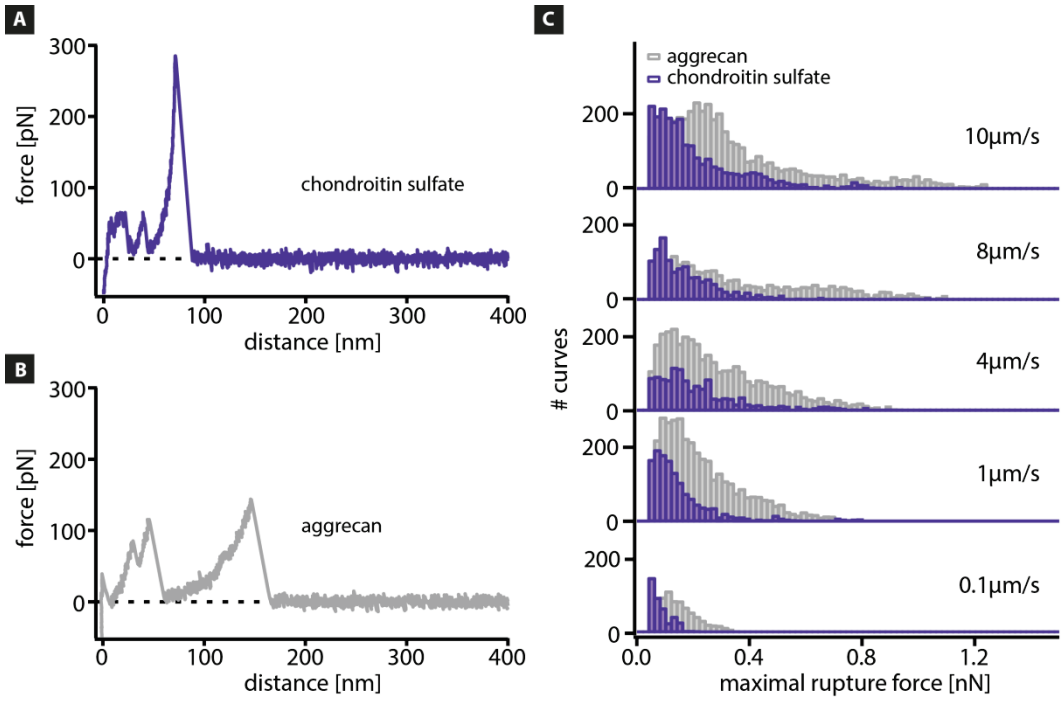

Figure 36. Exemplary force-distance curve for (**A**) chondroitin sulfate and (**B**) aggrecan. (**C**) Velocity dependence of the maximal rupture force on hydrogenated diamond in PBS. For chondroitin sulfate (purple) 4201 data points were evaluated and for aggrecan (grey) 1927. Adapted from [77].

It is of note, however, that although the maximal rupture forces are higher for aggrecan, they differ on average only by a factor of 1.5-2 as compared to chondroitin sulfate. Considering the theory of the rupture of parallel bonds, this result can be used to determine the additional number of bonds that are ruptured simultaneously for measurements with aggrecan compared to chondroitin sulfate. Rupturing N parallel bonds does not lead to a linear increase in rupture force f with the number of bonds, but to a logarithmic one [94].

$$f \sim \ln(N) \tag{18}$$

This means that only 5-8 additional bonds were ruptured in parallel when measuring with aggrecan as compared to chondroitin sulfate. This seems reasonable, because during the desorption of aggrecan not all side chains will desorb simultaneously and therefore not all bonds between the polymer and the surface were loaded at the same time to the exact same amount. It is also likely that not all possible interaction sites of the polymer really formed bonds with the surface.

Both chondroitin sulfate and aggrecan are highly negatively charged at physiological conditions. Therefore, the salt content in the solution was varied. No clear influence on the maximal rupture force for measurements on a hydrogenated diamond (Appendix and Figure 57) was observed. Changing the surface to for example a positively charged one, however, might lead to different results.

In summary, measurements with the bottle-brush polymer aggrecan lead to more evaluable events and a higher interaction force with the surface than measurements with a linear sugar chain. For aggrecan not all side chains will desorb simultaneously and the difference in

maximal rupture force is rather small which can be rationalized by the theory of the rupture of parallel bonds.

5.3. Branched polymer - A dendronized polymer

Finally single molecule force spectroscopy experiments with a dendronized polymer were performed (see schematics in Figure 32 on the right). A dendronized polymer consists of wedge shaped, highly branched dendrons which are linked together at the starting point. Its great advantage is the high density of functional end groups compared to just linear side chains. In this case, the dendronized polymer consists of around 500 dendrons of generation 4 with carboxyl end groups. This leads to the formation of a linear chain with highly branched side chains and approximately 8000 functional end groups.
Again force-distance curves were obtained on hydrogenated diamond in water. Two typical curves are shown in Figure 37A and B. Both rupture events and plateaus of constant force were observed with rupture events being more likely (88% of the evaluable events: rupture events; 12% plateaus of constant force).

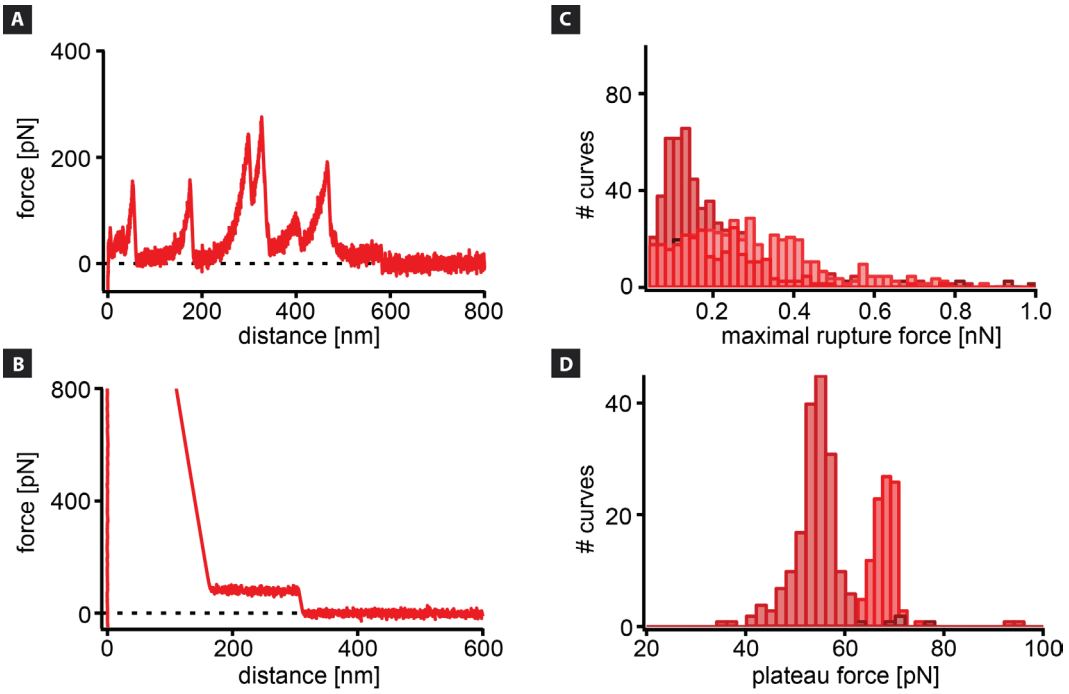

Figure 37. Typical force-distance curves for measurements with a dendronized polymer. In 88% of the curves (**A**) rupture events and (**B**) in 12% plateaus of constant force occurred. (**C**) The maximal rupture force and (**D**) the plateau force were determined and plotted in histograms. Each color represents the results from another experimental set. Adapted from [77].

It is somewhat surprising that a polymer with highly branched side chains can also be very mobile on the surface (i.e. shows plateaus of constant force). The height of the plateaus of constant force was again determined with an s-curve fit and plotted in a histogram (Figure 37D). The forces were in the same range as for PI and for PI-based graft polymers (~60pN). This means that the characteristics of plateaus of constant force are not changed by the addition of side chains and the architecture of these chains.

However as most of the events were rupture events, a low mobility of the dendronized polymer on the surface can be assumed. The maximal rupture forces measured with the

dendronized polymer (Figure 37C) are in the same range as for the bottle-brush aggrecan, but on average by a factor of two lower than for the graft polymer PI-*g*-PS(88). This means that although the side chains are highly branched, the interaction strength with the surface is not increased. One possible explanation is based on the geometry of the dendronized polymer. Due to the high grafting density, the polymer adapts an almost cylindrical shape [62]. The contact area of this cylinder with the surface could in the extreme case simply be a line contact with a low interaction strength. The rather small contact area might explain the low maximal rupture forces compared to just linear chains. Stronger molecular interactions, which were not a topic of this study, might be necessary to further increase the contact area of the dendronized polymer with the surface and consequently enhance the interaction.

In contrast, AFM images of aggrecan did show that the side chains were, despite of the small spacing between them (2-3nm), in contact with the surface [95]. But here the low magnitude of the maximal rupture forces can be explained with the theory of the rupture of parallel bonds [94] and that during desorption not all bonds were loaded at the same time. Again, the contact area and therefore the interaction force might be further enhanced by stronger molecular interactions. As aggrecan is negatively charged, one could for example take advantage of electrostatic interactions by using a positively charged surface.
Also intra-chain interactions can alter the adhesion. Although PI-*g*-PS(88) has a rather low grafting density with only 10 side chains per PI backbone and a spacing of around 60nm, the adhesion to the surface is stronger than for bottle-brushes or branched chains. These higher interaction forces are possibly caused by the formation of entanglements and a polymer bundle with strong intra-chain interactions.

To sum up, the contact area is an important parameter for designing polymer architectures for coatings but also intra-chain interactions can determine the adhesion strength.

5.4. Single polymer friction with different polymer architectures

After investigating the influence of side chains and their architecture on adhesion, the mobility of the polymers on the hydrogenated diamond surface was evaluated in more detail. To this end, single molecule friction force microscopy was used. In chapter 3.3 a more detailed description of the measurement process is given. In short, force-distance curves were obtained, but with a slightly modified protocol. The surface is approached until the cantilever is in contact with the surface. During a short waiting time (here: 1s) the polymer can adsorb to the surface. Then, the cantilever is retracted, but the retrace is interrupted at a point where the polymer is still in contact with the surface. The z-position of the cantilever is held constant and the cantilever is moved parallel to the surface perpendicular to its long axis. After a defined x-distance is covered and short waiting time, the same x-distance is moved back and the retrace in z-direction is completed.
This approach allows to gain information about the friction between the polymer and the surface and therefore about the mobility of the polymer on the surface.

First, the behavior of PI was compared to the graft polymers PI-*g*-PS. Sliding (a plateau of constant force), desorption stick (a continuous decrease in force) and cooperative stick

(rupture events) were observed. In Figure 38 typical force-x-distance curves for PI and PI-*g*-PS(88) are shown.

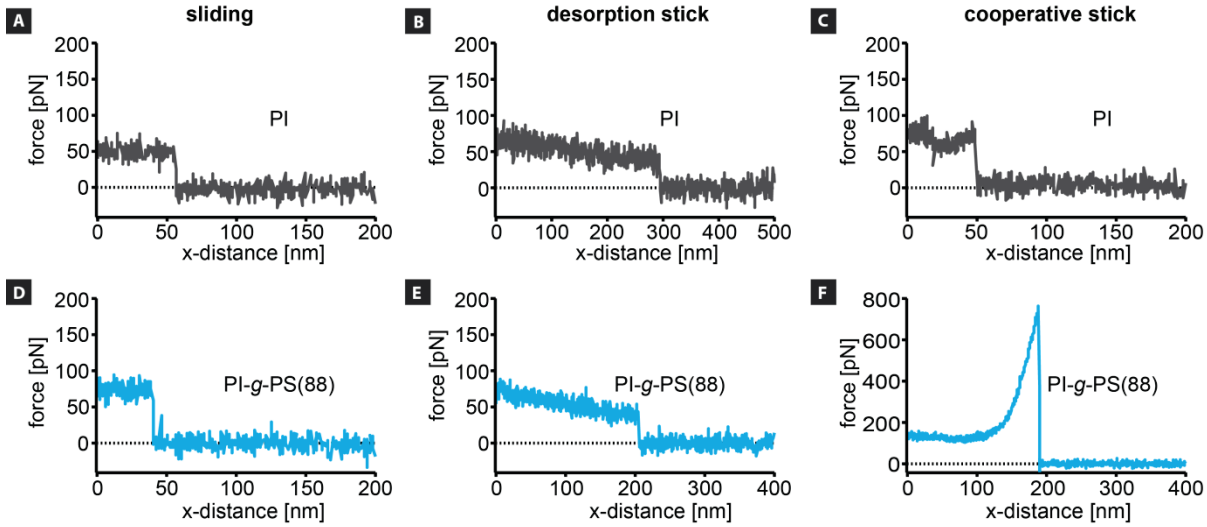

Figure 38. Three different motifs were observed during the lateral movement of PI and PI-*g*-PS(88), namely (**A** and **D**) sliding, (**B** and **E**) desorption stick and (**C** and **F**) cooperative stick.

If sliding occurs then the polymers were highly mobile and slid with undetectable friction force over the surface. In the case of desorption stick, the polymer cannot move laterally, but it is possible to desorb it from the surface in z-direction. The polymer is immobile on the surface, but with high internal chain dynamics. See chapter 3.3 for a geometrical explanation of the decreasing force.
The last motif, cooperative stick, represents the case where the polymers are not only laterally immobile, but also confined in z-direction due to low internal chain dynamics. The polymers can only be desorbed by stretching until the bonds between the polymer and the surface break, resulting in characteristic rupture events.

For linear chains like PI, sliding and desorption stick are the two main motifs observed during lateral movement (Table 2). This means that these polymers are either highly mobile on the surface or could at least be desorbed in z-direction with high internal chain dynamics.

	sliding	desorption stick	cooperative stick	# curves	events
PI	36%	61%	3%	124	67%
PI-*g*-PS(3)	16%	76%	8%	312	84%
PI-*g*-PS(14)	12%	85%	3%	199	79%
PI-*g*-PS(88)	9%	76%	15%	273	86%

Table 2. The occurrence of sliding, desorption stick and cooperative stick together with the total number of measured force-distance curves and the occurrence of any kind of events in these curves for PI, PI-*g*-PS(3), PI-*g*-PS(14) and PI-*g*-PS(88) on hydrogenated diamond in water.

The same holds true for the graft polymers PI-*g*-PS(3) and PI-*g*-PS(14): desorption stick is the main motif observed. In some curves cooperative stick occurred, but these were only present in less than 8% of the evaluable events (Table 2).

Measurements with PI-*g*-PS(88) revealed a shift away from sliding (8%) to desorption stick (74%) and cooperative stick (15%). This means, that PI-*g*-PS(88) was less mobile on the

surface with decreased internal chain dynamics. These findings support the theory derived from adhesion measurements that due to stronger intra-chain interactions (caused by entanglements) in the polymer bundle, the bundle has a decreased mobility on the surface. A reduced mobility and stronger intra-chain interactions lead to a stronger interaction with the surface and therefore a higher occurrence of rupture events with a higher maximal rupture force.

In the following the behavior of chondroitin sulfate (a linear sugar chain) and aggrecan (a bottle-brush polymer) were compared during single molecule friction force microscopy. A completely different behavior than for PI and PI-*g*-PS was observed. No sliding or desorption stick was observed, but only cooperative stick (Figure 39).

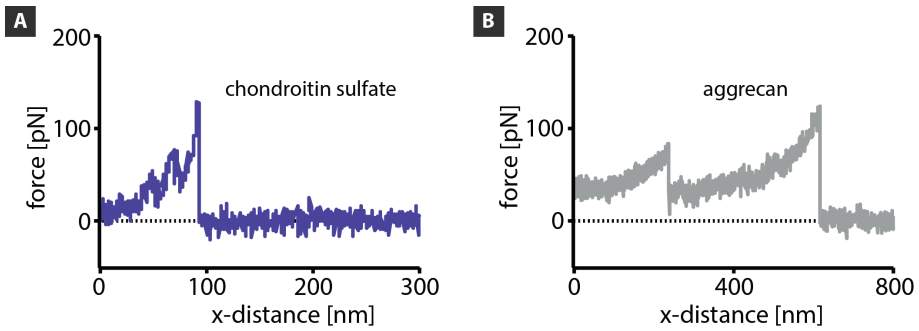

Figure 39. (**A**) Pulling chondroitin sulfate and (**B**) aggrecan laterally across a hydrogenated diamond surface in PBS revealed only cooperative stick.

This means that both polymers were highly immobile on the surface with low internal chain dynamics. They could only be detached by stretching until the bonds between the polymer and the surface break. This behavior is consistent with adhesion measurements, where force-distance curves resulted mostly in rupture events and no change in mobility after the addition of side chains was observed.

5.5. Conclusion

Changing the architecture of polymers is one way to improve the properties of coatings. However the molecular mechanisms of the interaction of the polymers themselves with a surface and the dependence of this interaction on the addition and architecture of side chains is not yet resolved. Here, it was shown with linear, graft, bottle-brush and branched polymers that the adhesion is unaffected by the addition of side chains and their architecture as long as the polymers are mobile on the surface. For less mobile polymers, the contact area with the surface together with the intra-chain interactions in the polymer bundle (e.g. in form of entanglements) are responsible for the adhesion strength. Polymers with branched side chains did not exhibit a higher interaction force with the surface compared to linear chains. The high branching density could lead to a reduced contact area with the surface and therefore a reduced interaction force. Considerable stronger and more specific bonds with the surface, that were not investigated in this work, could increase the contact area and thus increase the number of interactions and the adhesion strength. These findings can help designing and selecting polymers for various surface coatings.

6. Single molecule adhesion and friction on biological surfaces

Prior to the present work various aspects of the interaction of single linear polymers with solid surfaces were already well studied. Examples are the dependence of the hydrophobicity of polymers and surfaces [15, 90], co-solutes [16], salt and pH [17] on adhesion. Here the temperature dependent behavior of linear chains with varying hydrophobicity on different substrates was investigated in water, but also in the presence of solvents [13, 19]. Furthermore not only linear polymers were used, but polymers with side chains with different architectures. Both synthetic and naturally occurring polymers were compared. Changing the architecture, the temperature and adding solvents to the solution are first steps towards the understanding of more complex biological systems. The next step is to use not only naturally occurring polymers, but also biological surfaces. At biological surfaces a complex interplay of different constituents is responsible for the correct functioning. One of these constituents can be coupled covalently to the AFM tip and the interaction with the biological surface in terms of adhesion and mobility can be probed on the single polymer level.
An example for such a biological interface is articular cartilage. Cartilage covers the end of the joints and can bear high loads, but at the same time provides very low friction (for more details see chapter 2.5). Many different constituents act synergistically to maintain its correct functioning: aggrecan, hyaluronic acid, collagen and PRG4 to name only a few examples. Up to now the underlying molecular mechanisms are not completely understood thus a single molecule force spectroscopy approach might help to answer some of the open questions.

The interaction of one constituent of cartilage, namely the bottle-brush polymer aggrecan, with solid surfaces was already investigated in this work. Aggrecan was covalently bound to the AFM tip and vertical as well as lateral pulling experiments were performed on hydrogenated diamond. The results are discussed in chapter 5. Aggrecan was highly immobile on the diamond surface, which led to rupture events in force-distance curves. Surprisingly, the maximal rupture forces were only marginally higher than for a linear polysaccharide chain.
Therefore aggrecan was chosen for a first set of further experiments, now with a biological surface. The same cantilever, which was used for experiments on hydrogenated diamond, was used to obtain force-distance curves on articular cartilage. This allows to reduce deviations caused by the calibration of the spring constant in order to allow a better comparison of both surfaces. Cartilage samples were obtained from the knee joints of the hind legs of lambs. The preparation of the samples is explained in chapter 3.6. The results are shown together with the results obtained on hydrogenated diamond in Figure 40.

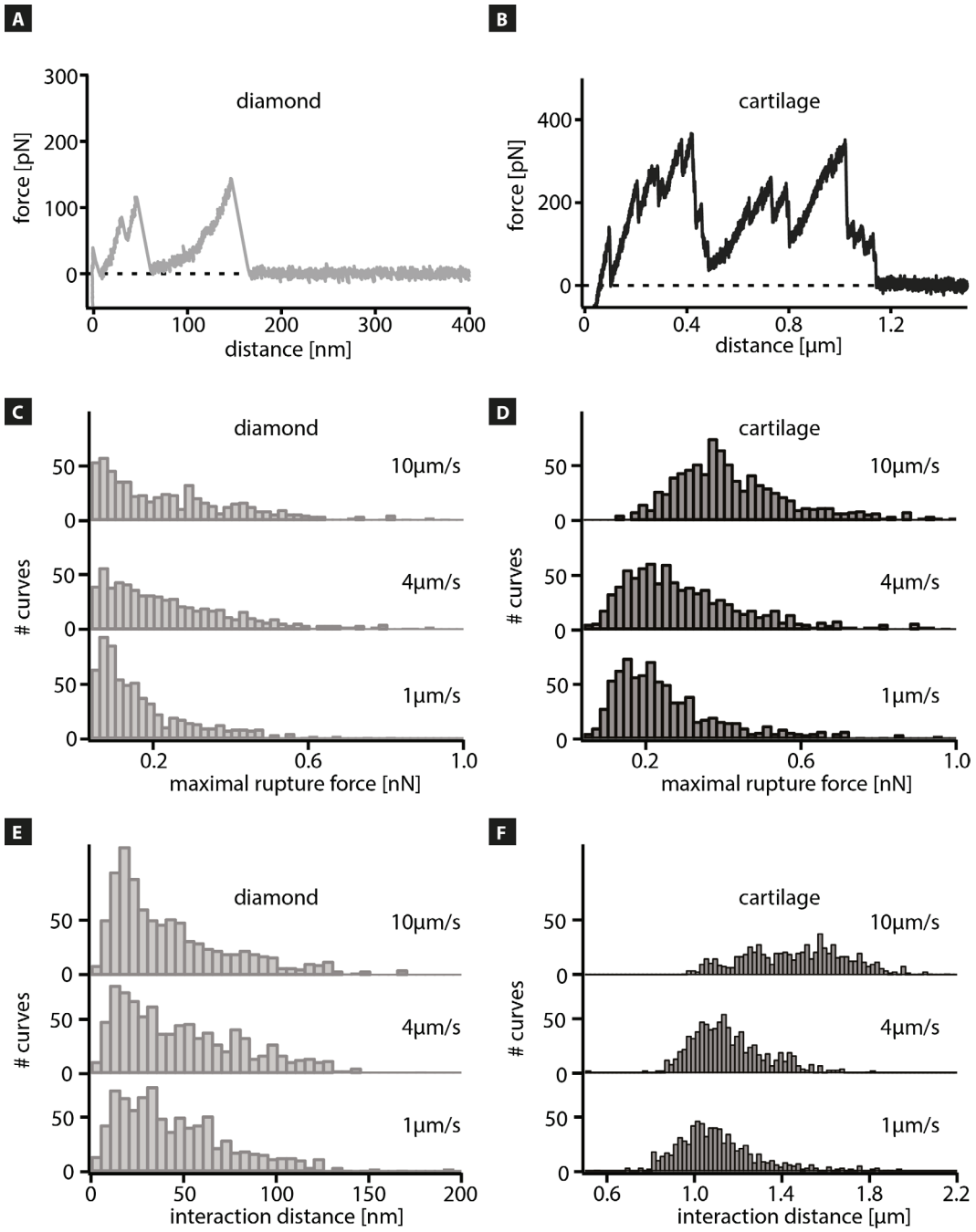

Figure 40. Typical force-distance curves measured with aggrecan in PBS (**A**) on diamond and (**B**) on cartilage with the corresponding velocity dependent maximal rupture forces (**C** and **D**) and interaction distances (**E** and **F**). Note the different scaling in the y-axis of force-distance curves and in the x-axis of interaction distance plots.

Similar to measurements on hydrogenated diamond (Figure 40A), the only motif visible in force-distance curves on cartilage were rupture events (Figure 40B). The maximal rupture force measured on articular cartilage is higher compared to diamond, but only by a factor of 2-3. With increasing velocity the maximal rupture force increases. The increase is more pronounced than on diamond. Additionally, the interaction distance was determined. It corresponds to the distance at which the force ultimately drops to zero. For the example shown in Figure 40A, the interaction distance is around 170nm, while for the force-distance curve performed on cartilage (Figure 40B) the interaction distance is almost 1200nm. On average, the interaction distances on cartilage increased by a factor of 20 compared to measurements on diamond. This distance is then even larger than the contour length of

aggrecan (400nm).
One possible explanation is the following: During the dwell time on the cartilage surface aggrecan adsorbs to the surface and interacts with other polymers on the surface. Likely candidates for interactions with aggrecan are for example hyaluronic acid and PRG4 as they are located at the cartilage surface. Furthermore, hyaluronic acid is known to form complexes with aggrecan. These interactions can for example manifest themselves in the form of entanglements. During the retrace, aggrecan is pulled, together with the entangled polymers, away from the surface and the measured force does not drop to zero until the entanglements loosen. Therefore the interaction length is longer than the contour length of aggrecan.

To further investigate the interaction of aggrecan with the cartilage surface, single molecule friction force microscopy was used. Therefore, aggrecan was pulled laterally across the surface. A typical curve is shown together with one obtained on hydrogenated diamond in Figure 41.

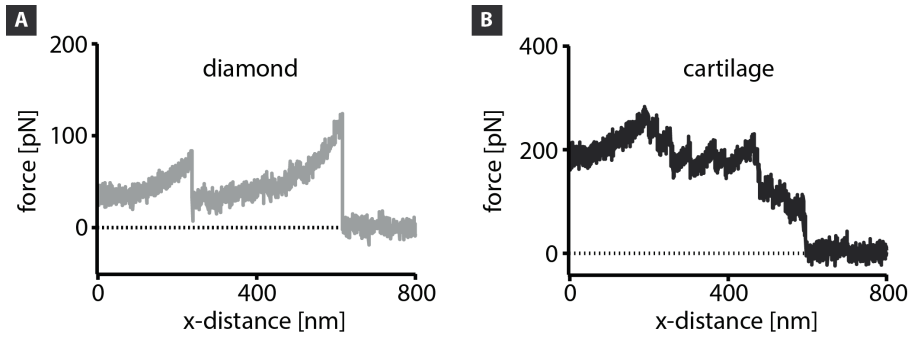

Figure 41. Typical force-x-distance curve for aggrecan (**A**) on diamond and (**B**) on cartilage in PBS. Please note the different force scales.

Like observed during vertical pulling, the only motif visible were rupture events. Aggrecan is not only highly immobile on hydrogenated diamond with low internal chain dynamics, but also on cartilage. The internal chain dynamics might even be further lowered by the strong interaction of aggrecan with other polymers present at the cartilage surface.

These are promising first results on the interaction of a single biological polysaccharide with a biological surface. As both aggrecan and cartilage are highly negatively charged, it would also be interesting to see if changing the salt concentration in the solution changes the interaction with the surface. Preliminary data on the influence of salt on the maximal rupture force and on the interaction length was already obtained, but no clear dependence on salt concentration was observed (A7 and Figure 57). A closer investigation is thus needed. Moreover, not only the interaction of aggrecan with the cartilage surface should be investigated, but also of other components of articular cartilage. It is also conceivable to couple not a single polymer to the tip, but to cover the whole tip with a layer of polymers or a mixture of different polymers. This is feasible, because with the functionalization protocols used in this thesis a large variety of different polymers with different functional end groups can be coupled to the AFM tip. This could then be used as a "bottom-up" approach where the composition of the polymers on the tip is tuned to get closer to the real composition of cartilage. A related approach was used by Han et al. [96], where both the surface and the tip

were completely covered with aggrecan and the adhesion was probed. This would help to further understand the complex interactions of two opposing cartilage surfaces in a joint.

As not only adhesion can be probed with this setup, but also friction, these results can be used to close the gap between the friction measured between a single polymer and articular cartilage and the friction between two opposing articular cartilage surfaces in a joint. Therefore the requirement, however, is not only to understand the mechanisms behind the friction of single polymers on a cartilage surface, but also to understand micro- and macroscopic friction. This is the goal of the next chapters.

7. Articular cartilage – Lubrication by viscosupplementation

Articular cartilage can be found in joints at the end of the bones. It provides exceptionally low friction, can withstand forces of several times the body weight and tolerates permanent changes of moving direction. This is enabled by a triphasic structure and the complex interplay of its constituents (see chapter 2.5). With advanced age, the exceptional properties of cartilage deteriorate and many people suffer from the most common type of arthritis called Osteoarthritis.

Its exact causes and the early pathology are, despite of a lot of research, not yet resolved. Osteoarthritis can be genetic, but also induced by previous injuries of the joint or by wear of cartilage due to age or malalignment [4, 97]. Amongst other things, osteoarthritis is associated with the loss of the ability of proteoglycans to aggregate and consequently a decrease in proteoglycan content [98]. They lose their ability to maintain interstitial fluid pressure and thus the friction increases (see chapter 2.5). Furthermore, this leads to an increased fraction of water in the cartilage due to more interstitial space. The interstitial space then grows further by a loosening of the collagen network. Important matrix components are degraded and the tissue compression properties and the tensile strength are reduced [99]. Additionally the load distribution in the cartilage tissue is changed. As chondrocytes are very load sensitive, they change after the onset of osteoarthritis in terms of proliferation, catabolism and enhanced cell death [100]. During the progression of osteoarthritis the molecular weight and the concentration of hyaluronic acid in the synovial fluid decreases, which causes a reduced viscosity and elasticity [101]. These changes and the altered mechanical properties lead to further damage also under normal loading conditions and eventually a complete loss of cartilage.

Knowledge about the early pathology of osteoarthritis as well as an effective clinical therapy is still missing. If the disease is too advanced then the last treatment option is a total joint replacement. However until now it was not possible to artificially recreate the properties of cartilage. Low wear in combination with low friction and also the insensibility to permanent changes in load and direction of motion are challenging to mimic. Thus even a total joint replacement is not a long-term solution and can fail due to various reasons. Therefore the different treatments focus on pain relief and the maintenance of joint movement in order to delay the need for a total joint replacement [4]. As osteoarthritis is often associated with inflammation, anti-inflammatory drugs are applied orally [102]. Also a change in life-style can be favorable and reduce the pain. Examples are loss of body weight, physical therapy and a change in activities [103].
Intra-articular hyaluronic acid injections are another treatment option termed viscosupplementation. These injections are believed to again increase the viscosity and elasticity of the synovial fluid. This should then improve the joint function and reduce pain [104]. Further, the catabolism of the chondrocytes and therefore the synthesis of matrix components should be stimulated.
Different meta-analysis of trials that investigated the effect of viscosupplements on patients were published. The validity of these trials, however, can potentially be questioned due to financial support by the industry and thus negative results are often not reported [105]. Most

of the meta-analysis concluded that intra-articular hyaluronic acid injections can lead to a pain reduction, also compared to placebos like saline [106]. The observed effect, however, was mostly small. One meta-study even showed that almost 80% of the pain relief is accounted for by the placebo effect [105]. It was controversially discussed if a higher molecular weight of hyaluronic acid can further improve the joint function due to the higher viscosity of those solutions, but proof for that is still missing [105].

One commercially available product for viscosupplementation is Sinovial®. It consist of 0.8% hyaluronic acid (16mg/2ml) in a physiological sodium chloride solution. The molecular weight varies from 800 to 1200kDa [104]. This is a low molecular weight compared to the weight of hyaluronic acid naturally present in cartilage, which can reach 20 MDa [4]. Clinical studies showed that the injection of Sinovial® leads to a reduction of pain [104].
Therefore, it was evaluated here if the pain relief can be attributed to an altered lubrication. Atomic force microscope (AFM)- and tribometer-based friction force microscopy were used to compare the friction coefficient measured on articular cartilage in a physiological sodium chloride solution (154mM) to measurements in Sinovial®. In previous *in vitro* experiments favorable effect of hyaluronic acid on the frictional properties, but also an increasing friction force were reported [47-49] (see chapter 2.5).

7.1. Viscosupplementation and aging during boundary lubrication

First, AFM-based friction force microscopy was used. With the AFM the boundary lubrication regime (i.e. the equilibrium friction coefficient) was probed (chapter 2.5.2).
A polystyrene sphere (diameter 10µm) was chosen as a probe and cartilage samples were taken from the patella groove of the hind leg of sheep or lambs. The samples were prepared as described in chapter 3.6. Animals of different age were chosen to investigate if aging is reflected in friction measurements and if the viscosupplement, which was developed for the treatment of osteoarthritis, which occurs more often with advanced years, acts different on sheep cartilage than on lamb cartilage.
The AFM was operated in contact mode. The cantilever was lowered until the polystyrene sphere was in contact with the surface and a defined normal load was applied. For one image, trace and retrace of a line (15µm) were scanned for at least 64 times with a constant normal load F_N and constant scan velocity. Normal loads ranged from 30 to 110nN and velocities from 9 to 113µm/s. The lateral deflection was recorded and converted into the friction force F_R (see chapter 3.4.1). A typical lateral deflection signal during trace and retrace is plotted in Figure 16A. F_R did not change with measurement time (Figure 16C). Therefore, the values obtained within one scan were averaged and the standard deviation was used as the error.

Typical results for the dependence of F_R on F_N for different velocities are plotted for an experiment with cartilage from sheep in 154mM NaCl in Figure 42A. The data was fitted with a straight line, with the slope of the line corresponding to the friction coefficient µ. The resulting friction coefficients were plotted for both NaCl (grey circles) and Sinovial® (blue circles) in dependence of the scan velocity in Figure 42B. For each experimental set a new cartilage sample was used. Consequently the samples were only exposed to either NaCl or Sinovial®, but not to both solutions. What can clearly be seen is, that no significant dependence on scan velocity and also no significant dependence on the lubricant could be

observed.
The same holds true for measurements on cartilage samples obtained from lambs. Here again, no difference between NaCl and Sinovial® was observed (triangles in Figure 42C and D). Additionally, the friction coefficients obtained on cartilage samples for lambs and sheep did not differ from one another. Aging was therefore not reflected in friction measurements on healthy tissue.

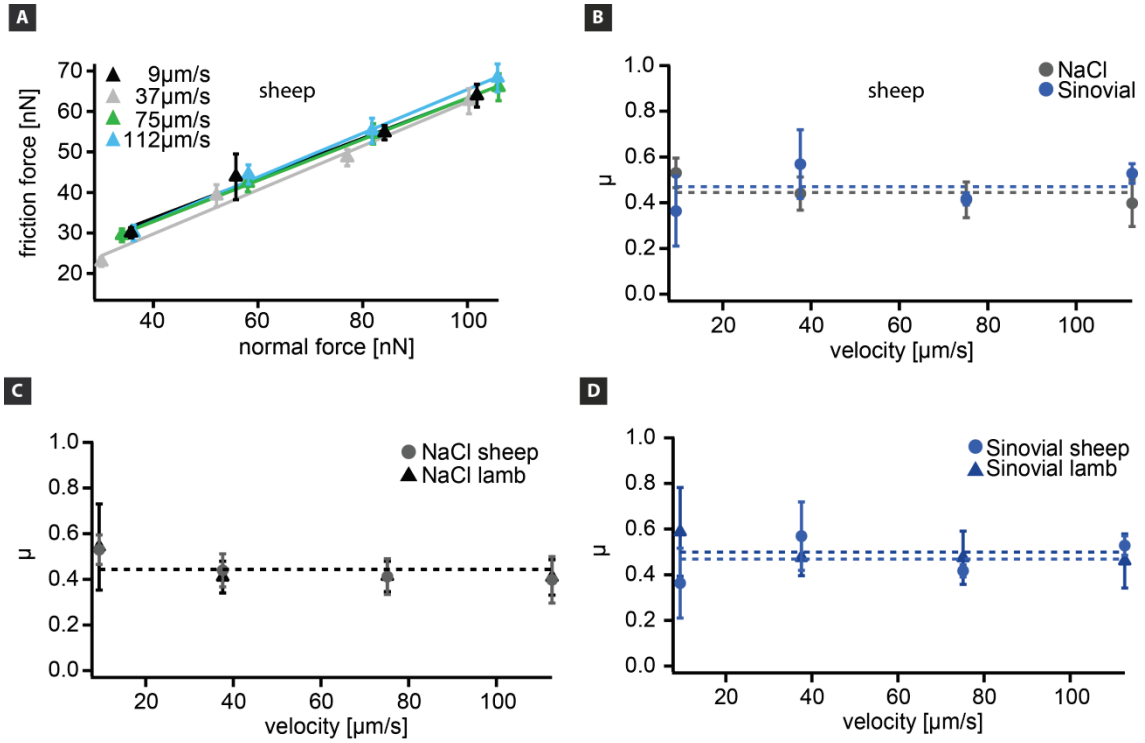

Figure 42. AFM-based friction force microscopy on cartilage samples from elderly sheep and young lambs. (**A**) Dependence of the friction force on normal force for different scan speeds in 154mM NaCl on sheep. For each velocity, the data was fitted with a straight line. The slope of the line corresponds to the friction coefficient µ, which is plotted in (**B**) for various scan velocities for measurements in 154mM NaCl (grey) and Sinovial® (blue). (**C**) Comparison of the friction coefficient µ for sheep (grey circles) and lamb (grey triangles) in 154mM NaCl. (**D**) Comparison of the friction coefficient µ for sheep (blue circles) and lamb (blue triangles) in Sinovial®. The dotted lines serve as a guide to the eye and correspond to the average friction coefficient for all velocities. The measurements on lamb were performed by Lorenz Wiegleb during his master thesis which was supervised by the author of this work.

One has to note, however, that the samples obtained from sheep often appeared more yellowish and less smooth, which indicated an aging process in the tissue. It was also more difficult to obtain reliable and reproducible results with samples from sheep. Especially the samples used for measurements in Sinovial® did show first indications of aging. In Figure 42 consequently only measurements on healthy looking cartilage of sheep were taken into account. On the other hand, experiments on aging cartilage samples resulted in increased friction coefficients. If these results were combined with the results from healthy looking sheep then the friction coefficient is higher compared to lambs (green circles, Figure 43).

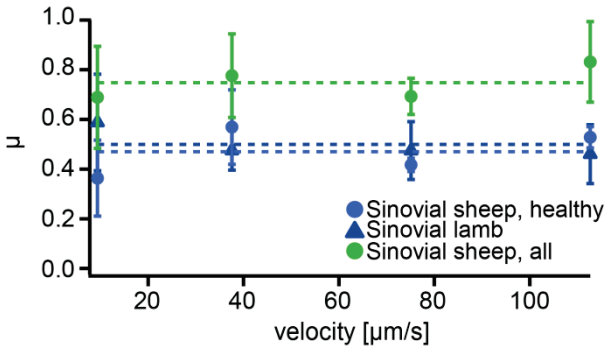

Figure 43. Friction coefficient for measurements in Sinovial® on lamb (blue triangles), healthy looking cartilage of sheep (blue circles) and on all cartilage samples from sheep even if they appeared not healthy (green circles). The dotted lines serve as a guide to the eye and correspond to the average friction coefficient for all velocities.

Although Sinovial® was developed to improve the lubrication behavior of aging cartilage, it did not reduce the friction coefficient in AFM measurements on sheep with indications of aging. For NaCl, the samples did not differ in the visual appearance and also not in the friction coefficient. Here it would be interesting to perform additional experiments on aging cartilage.

To summarize, the viscosupplement Sinovial® did not improve the frictional properties during boundary lubrication compared to a physiological NaCl solution on healthy cartilage tissue of sheep and lambs. Furthermore cartilage from sheep with first indications of aging showed an enhanced friction coefficient compared to healthy looking cartilage of sheep and lambs.

7.2. Viscosupplementation and a migrating contact regime

The next step was then to compare the influence of the two lubricants NaCl and Sinovial® on the friction coefficient with a linear tribometer. Here, two different setups were chosen: In the first setup, the friction between a polystyrene sphere (diameter 750µm) and cartilage from sheep was probed. In the second setup, both the probe and the surface consisted of cartilage samples from sheep with a diameter of 5mm and 10mm, respectively. Only samples from healthy looking sheep were measured. With both setups the migrating contact regime and therefore the effect of the interstitial fluid pressurization on the friction coefficient can be probed (see chapter 2.5.2). In contrast to AFM measurements where only boundary lubrication was probed, in a tribometer measurement the contact migrates fast enough to allow the recovery of the interstitial fluid pressure.
The measurement procedure was as follows: the probe was brought into contact with the surface until a defined normal load was applied. Then a line was scanned with a constant normal load and a constant sliding velocity. During the measurement, the lateral deflection of the probe was recorded and converted into the friction coefficient µ. This was repeated for several normal loads and velocities. A typical friction loop obtained during a tribometer measurement with a polystyrene sphere sliding over the cartilage surface can be seen in Figure 16B. Similar to AFM measurements, the friction coefficient did not change with measurement time (Figure 16D). Therefore, the values obtained during one scan were averaged (without stiction) and the standard deviation was used as an error.

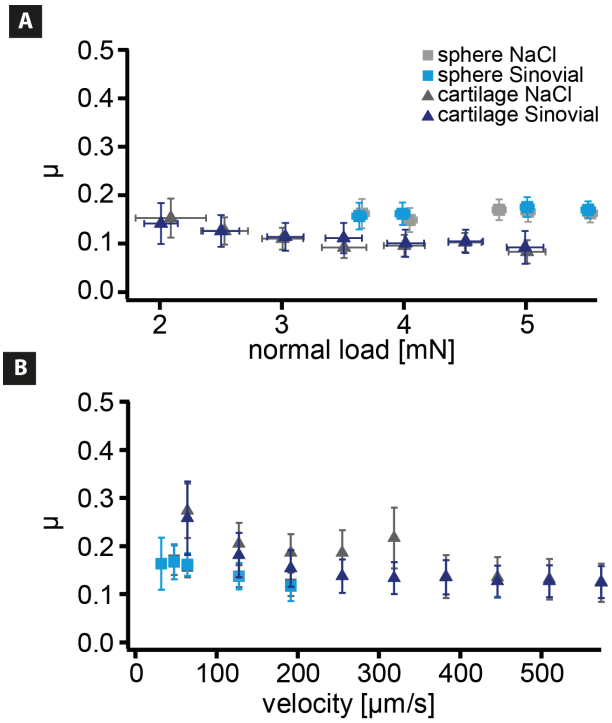

Figure 44. Comparison of the friction coefficient μ for measurements with a polystyrene sphere (squares) and a second cartilage sample as a probe (triangles) in dependence of (**A**) the load and (**B**) the velocity for NaCl (grey) and Sinovial® (blue). The cartilage samples were obtained from sheep.

The results from measurements with the polystyrene sphere as a probe can be seen in Figure 44 as squares. Figure 44A and B show the dependence of the friction coefficient on normal load and velocity for 154mM NaCl (blue squares) and Sinovial® (grey squares). The friction coefficient μ is not affected by a change in normal load. With increasing velocity a decrease in the friction coefficient was observed, but the differences were only marginal. Most importantly, no difference between NaCl and Sinovial® was observed. Similar to results obtained with the AFM during boundary lubrication, the lubricant did not influence the friction coefficient in the migrating contact regime.

The results obtained from measurements with a second cartilage sample as a probe instead of a polystyrene sphere were also plotted in Figure 44 as triangles. Consistent with the previous results, no significant difference between the two lubricants was observed. The friction coefficient decreased with increasing normal load and increasing velocity. However, like for measurements with a polystyrene sphere, the changes are only minor.
It is of note that although the loads are in the same range for measurements with both, the polystyrene sphere and cartilage against cartilage, the pressures differ considerable due to the different contact areas. For measurements with the polystyrene sphere, the pressures reached 200kPa, whereas the pressures for sliding cartilage against cartilage are due to the higher contact area lower than 1kPa. Still, the observed friction coefficients are in the same range and show a similar load and velocity dependence. For comparison, the pressures applied while measuring with the AFM were in the range of a few hundred Pa. Here the friction coefficients were about a factor of two higher compared to tribometer measurements and also compared to previously published results from AFM measurements [42]. One reason might be the calibration of the lateral sensitivity. It was reported that the lateral sensitivity obtained with the DLFC method was higher compared to other calibration

methods, which would at least partially explain the higher friction coefficients. Nonetheless, with all considered measurement devices and setups, no effect of the lubricant on the friction coefficient was observed.

In addition to the kinetic friction coefficient, the tribometer measurements also revealed information about stiction at the beginning of each scan (Figure 16B). Stiction reflects the adhesion that has to be overcome before the probe can start sliding over the surface (see chapter 2.4 for details). The results for measured stiction for cartilage sliding over another cartilage surface and for using a polystyrene sphere as a probe are summarized in Table 3. Not for all normal loads measurements were obtained, thus some entries are empty.

Load [mN]	2.5	3.0	3.5	4.0	5.0	5.5
cartilage NaCl	0.33±0.17	0.44±0.26	0.42±0.25	0.42±0.29	0.40±0.29	-
cartilage Sinovial®	0.51±0.36	0.50±0.37	0.54±0.44	0.47±0.35	0.44±0.35	-
PS sphere NaCl	-	-	0.44±0.01	-	0.33±0.16	0.35±0.02
PS sphere Sinovial®	-	-	0.48±0.07	-	0.48±0.20	0.35±0.07

Table 3. The dependence of stiction on normal load measured with a polystyrene (PS) sphere or a cartilage surface sliding over cartilage in 154mM NaCl and in Sinovial®. Not all normal loads were probed in all experiments, therefore some entries are empty.

The values for stiction measured in Sinovial® were consistently slightly higher compared to NaCl. The differences, however, were only marginal and the errors were especially for measurements with a second cartilage sample as a probe quite high.

In summary, no significant difference between NaCl and Sinovial® was observed during tribometer measurements in the migrating contact regime. Stiction is slightly increased in Sinovial®. This holds true for using a polystyrene sphere, but also a second cartilage sample as a probe.

7.3. Summary and conclusion

The influence of a viscosupplement on the frictional behavior during boundary lubrication (AFM) and lubrication facilitated by the interstitial fluid pressurization in the migrating contact regime (tribometer) was probed. Sinovial® was not favorable for the lubrication of cartilage in comparison to a physiological sodium chloride solution. The measured friction coefficients were similar for both lubricants in all setups.

These results, however, implicate the question, why viscosupplementation is helpful for some patients [104] and why hyaluronic acid is present in natural synovial fluid when not for its lubrication properties.
One hypothesis is that hyaluronic acid protects the cartilage tissue from wear, but is not very effective in providing low friction. Lee et al. [21] showed that after the enzymatic digestion of hyaluronic acid in cartilage, the friction force increased only slightly (up to a factor of two) whereas the induced wear increased significantly. These results, together with previous ones on the lubrication and wear properties of physisorbed and grafted hyaluronic acid on mica [107], lead to the conclusion that hyaluronic acid maintains the wear resistance of cartilage. This was especially apparent while measuring under high loading conditions. During loading hyaluronic acid is trapped, due to its high molecular weight (up to 20MDa), in the porous collagen network. There, it forms complexes with PRG4 and shields the surface from

wear. With advanced years [108] and at the onset of osteoarthritis, a decreased molecular mass of hyaluronic acid was observed [101]. Due to the lower weight it might not be trapped as efficient in the collagen network anymore and a wearing out of the cartilage tissue can be observed.
In Sinovial®, however, the molecular weight of hyaluronic acid is only around 1MDa [104] and therefore much lower than the molecular weight in healthy tissue. This could be one reason, why the friction coefficient is not affected by the viscosupplement. Sinovial®, or to be more specific the hyaluronic acid contained in Sinovial®, cannot be trapped in the collagen network and is simply squeezed out of the contact area during sliding. To test this hypotheses it would be interesting to measure with other viscosupplements with a higher molecular weight of hyaluronic acid. Additionally, experiments under higher loading conditions might be helpful, as the wear should be more prominent there. After the measurements, induced wear on the surfaces could be determined and related to the lubricant used.

To summarize, although no significant difference in friction force between NaCl and Sinovial® was observed, the wear resistance might be altered. Sliding with higher loads and a quantification of the induced wear can help to further understand the benefit of Sinovial® and hyaluronic acid. Furthermore it can be concluded that low friction does not always imply a good resistance against wear.

8. Response of cartilage tissue to changes in salt concentration

As pointed out above, cartilage is a triphasic material with a solid collagen network, proteoglycans and a fluid phase containing electrolytes like sodium (Na^+) and chloride (Cl^-). Cartilage is highly negatively charged due to the presence of high amounts of GAG chains in the proteoglycans. These negative charges draw water into the tissue and cause the cartilage to swell. Changing the salt concentration alters the electrostatic shielding of these charges and therefore the swelling behavior of the complete tissue. Sinovial® and the NaCl solution used above did have the same physiological concentration, namely 154mM. There, no difference in friction force was observed. It was previously shown that with decreasing sodium chloride concentration, the water content and the thickness of cartilage increased [109-111]. An increase in water content can also be observed during the development of osteoarthritis, as more interstitial space is available and can be filled with fluid. For the friction coefficient, different salt dependent behaviors were reported. Sliding cartilage against glass revealed decreasing initial and equilibrium friction coefficients with increasing NaCl concentration [109]. The opposite behavior was observed for a cartilage-on-cartilage setup where both the initial and the equilibrium friction coefficient increased with salt concentration [112]. To our knowledge, however, no atomic force microscopy based study on the salt dependence of the friction coefficient has been published yet.
Here a combination of imaging and friction force microscopy with the atomic force microscope is used to characterize the effect of salt concentration on both the structure of the collagen network and the measured friction coefficient. A part of this work was performed by Lorenz Wiegleb during his master thesis which was supervised by the author of this work. Therefore contact mode images of cartilage in different solutions, namely water (hypotonic concentration), 154mM NaCl (physiological concentration) and 2M NaCl (hypertonic concentration) were performed. The images were recorded with a scan velocity of 1Hz and with soft cantilevers (MLCT, Bruker AFM Probes, Camarillo, USA) to avoid any damage to the network. In contrast to friction force microscopy experiments, cantilevers with a sharp tip were chosen instead of a sphere to achieve a higher spatial resolution. In contrast to a sphere diameter of 10µm the nominal tip radius of the sharp tip was 20nm. Three typical images can be seen in Figure 45.

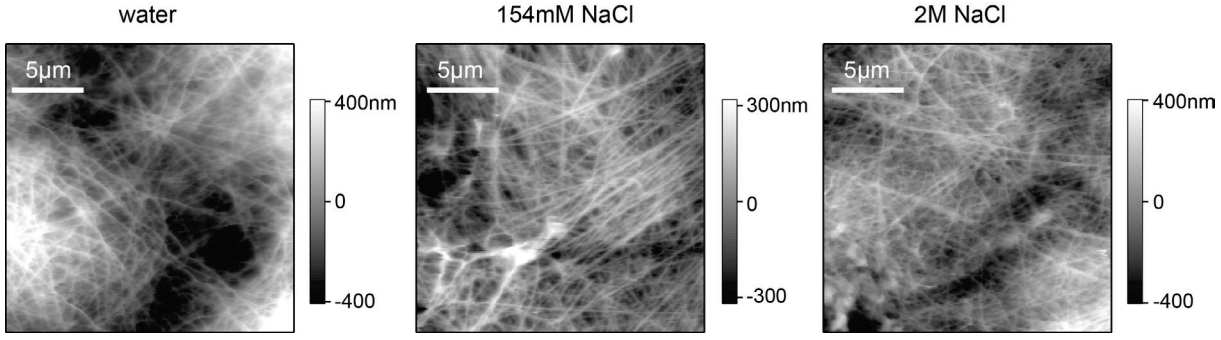

Figure 45. Contact mode images of three different cartilage samples in different lubricants (water, 154mM NaCl and 2M NaCl).

In all three solutions, the collagen network is clearly visible. In 2M NaCl (right) the network appears to be denser. This is also reflected in the average roughness (Table 4).

	water	154mM NaCl	2M NaCl
roughness	195 ± 47 nm	145 ± 66 nm	139 ± 50 nm

Table 4. Averaged roughness obtained from contact mode images on cartilage in three different solutions together with the standard deviation.

Although the standard deviations are quite high (which is attributed to cartilage being a biological material, where not the whole surface has the exact same structure), it can be seen that the roughness decreased with increasing salt concentration. This can be explained by a decrease in cartilage thickness with increasing salt concentration. More salt enhances the electrostatic shielding of the negative charges of the proteoglycans and the water content in the tissue decreases [109]. The network shrinks and appears denser and consequently the roughness decreases.

The next step was then to investigate if the altered appearance of the network was mirrored in the friction coefficient. Therefore the friction coefficient was measured with the AFM in the three solutions for different scan velocities. Here, a cantilever with a polystyrene sphere was chosen for the experiments. The obtained friction coefficients were plotted together in one graph (Figure 46).

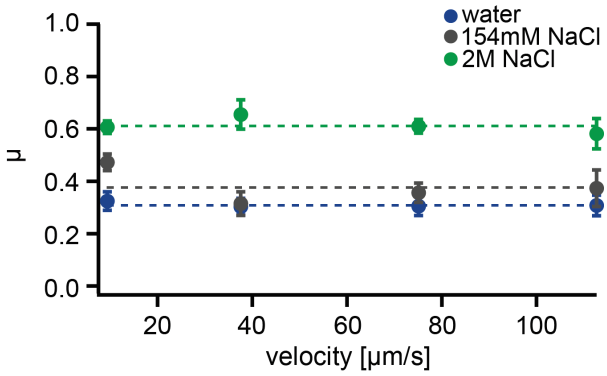

Figure 46. Averaged friction coefficient μ for measurements in water (blue), in 154mM NaCl (grey) and in 2M NaCl (green) for different velocities. The samples were prepared from young lambs. The dotted lines serve as a guide to the eye and correspond to the average friction coefficient for all velocities.

The average friction coefficients measured in water (blue) and in a physiological NaCl solution (grey) did not reveal a significant difference. Only at the slowest scan velocity, the friction coefficient measured in 154mM NaCl was significantly higher compared to water. Measurements in 2M NaCl (green), however, did show an increase of the friction coefficient. As noted above, the boundary lubrication regime is probed during an AFM measurement. This means that the interactions with the solid network are responsible for the measured friction force. With increasing salt concentration, the cartilage shrinks and the network becomes denser. More interaction between the polystyrene sphere and the cartilage surface can take place and the friction coefficient is consequently higher in 2M NaCl compared to water and 154mM NaCl. Although the surface roughness in 154mM NaCl already decreased compared to water, no significant effect on the average friction coefficient was observed. Only at the slowest velocity, the friction coefficient for measurements in water was significantly lower. Some individual measurements resulted in an overall lower friction

coefficient for water compared to 154mM NaCl, but on average the differences cancel each other out. Here additional measurements are needed to clarify if the friction coefficient measured in 154mM NaCl really changes compared to water.

In summary, a higher salt concentration leads to a reduced cartilage thickness, a decreased surface roughness and a denser network. This dense network results then in an increased friction coefficient.

9. Recovery after de- and rehydration of articular cartilage

As already stated, cartilage is a triphasic material with two solid and a liquid phase, whereas the liquid phase represents 70-80% of the total volume. Therefore, it is interesting to see if and how the dehydration and following rehydration of cartilage affects its properties. These extreme conditions could help to understand more about the mechanical properties of articular cartilage. The question of de- and rehydration of cartilage is also relevant for physicians. Two different surgical procedures are widely used to operate on knee joints: arthroscopy or open surgery. Arthroscopy means that a fiberoptic camera (arthroscope) and surgical instruments are inserted in the knee joint through a small incision. This is a minimally invasive surgery and can reduce the recovery time and the trauma caused by the surgery to other connective tissue. In some cases, however, an open knee surgery is still inevitable so the treating physician can really look at the inside of the joint in an unimpaired way. Here, the knee is opened and the tissue is exposed to air. To prevent drying out of the cartilage, cloths which are saturated with liquid are draped around the joint. However, dehydration of the tissue can still occur. This dehydration was also observed with samples used for AFM or tribometer measurements. When exposed to air, dehydration especially at the edges of the sample occurs almost immediately. Therefore, the samples were always kept hydrated by wrapping them in meat and storing them in a refrigerator until the measurements were performed.

In the following it is investigated with an AFM-based approach, if the functional properties of cartilage are altered by de- and subsequent rehydration and if thus an avoidance of cartilage dehydration is essential. Therefore fresh, de- and rehydrated samples were imaged in contact mode and the friction coefficients of fresh and rehydrated cartilage samples were determined by AFM-based friction force microscopy and compared. Again the viscosupplement Sinovial® and water based solutions with different salt concentrations were used. A part of this work was performed by Lorenz Wiegleb during his master thesis and Frank Kramer during his bachelor thesis which were both supervised by the author of this work.
The experiments were performed as follows: After the preparation of the samples, the friction force was measured and the surface was imaged. As lubricants either Sinovial®, water, 154mM NaCl or 2M NaCl were chosen. For each lubricant a different cartilage sample was used, so the tissues were only exposed to one solution. In Sinovial® imaging of the surface was not possible due to the high viscosity of the fluid. After the measurements were completed, the lubricants were removed with a pipette and the samples were allowed to dry at room temperature over night. The next day, the samples were rehydrated for at least one hour in the lubricant they have been bathed in the day before. Afterwards, the friction coefficient was measured and the surface was again imaged in contact mode.

9.1. Rehydration at different salt concentrations

As a first step, the visual appearance of fresh, dehydrated and rehydrated cartilage samples from young lambs was compared. Photographs from fresh and rehydrated samples were taken immediately after the removal of the lubricant and for the dehydrated sample after

drying over night (Figure 47 top). No difference between the fresh and the rehydrated sample is visible. The color of the dehydrated sample changed to dark red due to the bone which is underneath the shrunk cartilage tissue shining through (Figure 47).

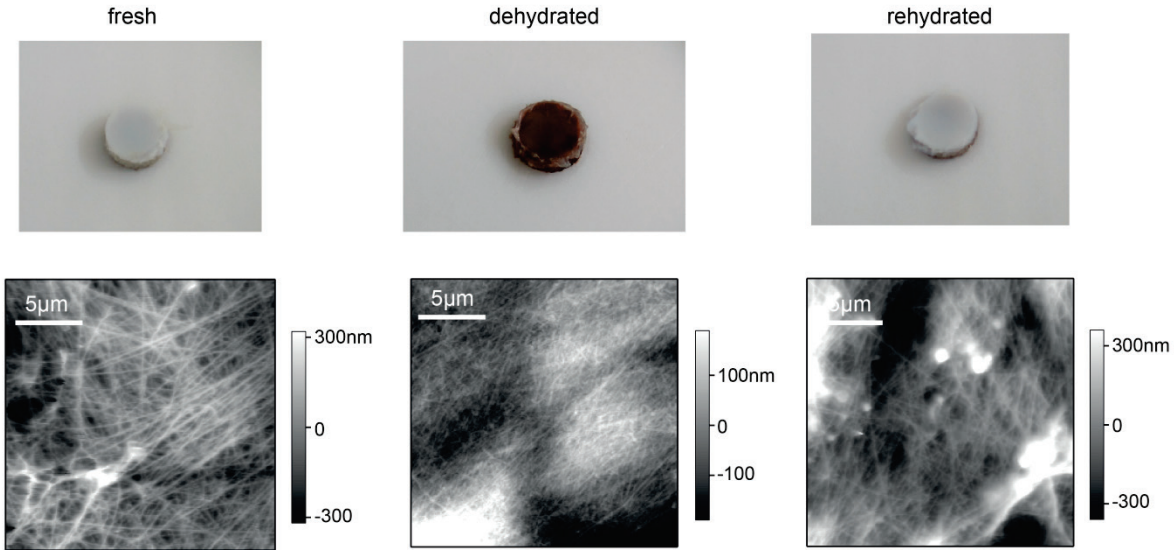

Figure 47. Photographs and AFM images of fresh, dehydrated and rehydrated cartilage samples from young lambs. The fresh and rehydrated samples were imaged in 154mM NaCl and the dehydrated ones in air. The photographs are courtesy of Lorenz Wiegleb.

Additionally the samples were imaged in contact mode with the AFM to observe if the network changed due to drying and rehydration (Figure 47 bottom). Fresh and rehydrated samples were imaged in 154mM NaCl and the dehydrated sample in air. The collagen network is clearly visible in all stages. After dehydration the network appears very dense, which is attributed to the shrinking of the sample due to the loss of water. A similar behavior was observed at high salt concentrations (chapter 8).The network of the rehydrated samples seems to be, at least partially, restored. However, the surface is more irregular and possible aggregates or depositions (bright spots) are visible.

Additional contact mode images were performed in water and in 2M NaCl on fresh and rehydrated samples to investigate how a change in salt concentration affects the rehydration behavior. For a better comparison, the results are shown together with the images recorded in 154mM NaCl in Figure 48.

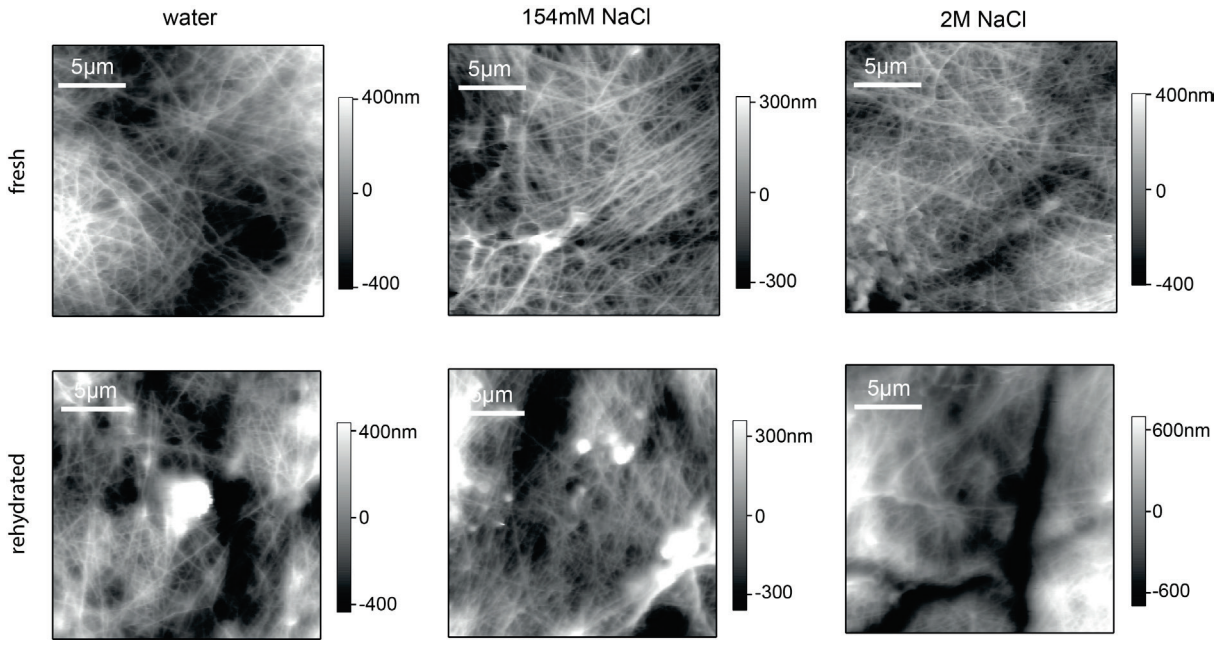

Figure 48. Contact mode images of fresh (upper row) and rehydrated (lower row) lamb cartilage samples recorded in water (left column), 154mM NaCl (mid column) and 2M NaCl (right column).

In all three solutions, the network of the fresh cartilage samples is clearly visible (upper row). Like observed after rehydration in 154mM NaCl, the network is not completely restored after rehydration in water and 2M NaCl and only partially visible (lower row). Especially in the image obtained in 2M NaCl after rehydration, the surface appeared to be very irregular with deep valleys. This effect can also be quantified by comparing the roughness of fresh and rehydrated samples (Table 5). Like shown before, the roughness of the fresh samples decreased with increasing salt concentration due to a denser network (chapter 8). After rehydration, the roughness in water was almost not affected while the roughness for samples which were rehydrated in 154mM NaCl increased (15%). For rehydration in 2M NaCl the increase was even more pronounced (51%).

	water	154mM NaCl	2M NaCl
roughness fresh	195 ± 47 nm	145 ± 66 nm	139 ± 50 nm
roughness rehydrated	197 ± 53 nm	170 ± 57 nm	285 ± 100 nm

Table 5. Averaged roughness obtained from fresh and rehydrated cartilage from lamb in three different solutions together with the standard deviation.

In addition, the friction coefficients for fresh and rehydrated cartilage samples were compared in the different solutions. The measurement procedure was the same as described above. The results can be seen in Figure 49. Here only measurements were taken into account were both the fresh sample and the rehydrated one could be probed. Therefore the values for the friction coefficient for fresh cartilage differ slightly from those shown in Figure 46.

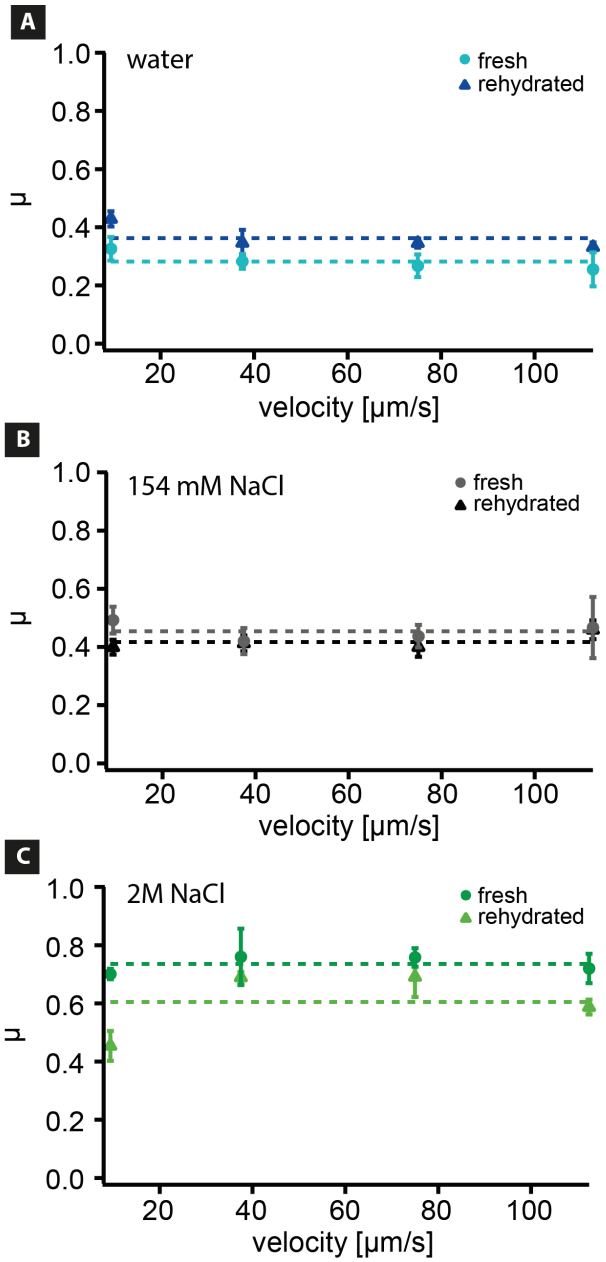

Figure 49. Friction coefficient μ for fresh (circles) and rehydrated (triangle) cartilage from lamb in (**A**) water, (**B**) 154mM NaCl and (**C**) 2M NaCl. The dotted lines serve as a guide to the eye and correspond to the average friction coefficient for all velocities.

The dependence of the friction coefficient for fresh samples on salt concentration was already discussed in the previous chapter. There, a higher friction coefficient for 2M NaCl was measured compared to water and 154mM NaCl due to a denser network (chapter 8). In contrast, the values shown here before dehydration indicate an increase of the friction coefficient with increasing salt concentration also for lower salt concentrations. As already pointed out before, additional measurements are needed to verify if the friction coefficient measured in 154mM NaCl really changes compared to water.
After rehydration the measured friction coefficients were not significantly changed compared to fresh samples. This holds true for all solutions. For water, this is consistent with AFM imaging where the roughness also did not change. For 154mM NaCl the changes in roughness as well as in the friction coefficient were only minor. For the cartilage samples which were rehydrated in 2M NaCl, however, the surface appeared to be less smooth and

more inhomogeneous with a significantly increased roughness, whereas the friction coefficient was not affected.

9.2. Rehydration in a viscosupplement

Finally, the friction coefficient was compared for fresh (red) and rehydrated (black) samples in 154mM NaCl and in Sinovial® (Figure 50).

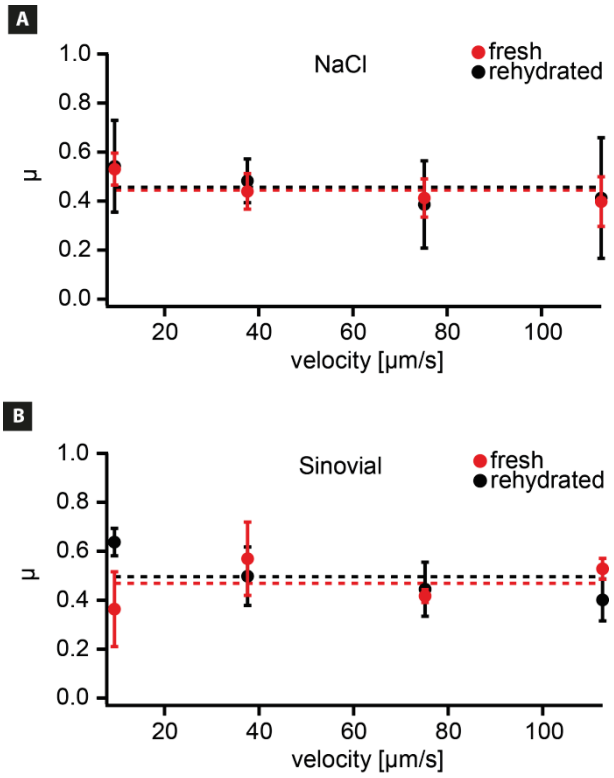

Figure 50. Friction coefficient μ for fresh (red) and rehydrated (black) cartilage from sheep in both (**A**) 154mM NaCl and (**B**) Sinovial®. The dotted lines serve as a guide to the eye and correspond to the average friction coefficient for all velocities.

Here again the measurements were performed with sheep cartilage. The results for the fresh samples were already shown and discussed in chapter 7.1. The friction coefficient measured in 154mM NaCl is not affected by de- and rehydration and its value is also similar to the friction coefficients measured on fresh and rehydrated cartilage in Sinovial®, which again is not affected by de- and rehydration. Thus similar to fresh samples, the lubricant did not change the friction coefficient and the frictional properties were completely restored after rehydration.

9.3. Conclusion

Rehydration in water, 154mM NaCl, 2M NaCl and also in Sinovial® had no significant effect on the friction coefficient, i.e. for fresh and for rehydrated samples the friction coefficient is almost identical. Especially after rehydration in 2M NaCl, however, the cartilage surface appeared less homogenous and rougher. This means that the cartilage network was not completely restored after rehydration. Surprisingly, this altered appearance of the network is not visible in the frictional properties of the cartilage samples.
A related effect was already observed when comparing the frictional properties of fresh

cartilage samples in 154mM NaCl and in Sinovial®. There, the friction coefficient did also not change, but first studies indicate a different wear protection.

This means, that although the measured friction coefficient seems to remain constant when measuring with a viscosupplement or after rehydration, the properties of the tissue like the recovery of the network and the wear protection might be altered. Low friction can therefore not always be related to low wear and a healthy tissue.

10. Outlook

The development of novel methods for detection and treatment of age-related diseases like Osteoarthritis and Alzheimer's disease can be supported by understanding the underlying molecular mechanism. Here, a combination of experiments with single polymers and microscopic lubrication measurements has been utilized to gain insight into the molecular mechanisms of adhesion and friction on both synthetic and biological surfaces. This can help to understand complex processes in biological tissue on a molecular level.

Measuring the interaction of a single polysaccharide, namely aggrecan, with an articular cartilage surface revealed promising first insights into the interaction of a single polymer with a biological surface. This approach can be pursued in the future by measuring not only the interaction of aggrecan with the cartilage surface, but also of other components of articular cartilage. It is also conceivable to couple not a single polymer to the tip, but to cover the whole tip with a layer of polymers or a mixture of different polymers. This could then be used as a "bottom-up" approach where the composition of the polymers on the tip is tuned to get closer to the real composition of cartilage.

This "bottom-up" approach could also be applied to microscopic friction force measurements. In the second part of the thesis microscopic friction was measured on articular cartilage with the atomic force microscope and a tribometer. The results show that a low and constant friction coefficient of articular cartilage is not always synonymous to properties like the structure of the network and the wear resistance being unaltered. This was revealed by comparing a viscosupplement to a physiological sodium chloride solution, by altering the salt content in the solution and finally by de- and rehydration of the cartilage tissue.
With the "bottom-up" approach one could now build an artificial cartilage surface and compare the results to those obtained with articular cartilage. There, one can start with a basic collagen network and add more and more constituents, which occur naturally in cartilage. Friction force, but also wear or rheology, can be probed. With this it might be possible to identify the components essential to the mechanical properties of cartilage. Also the opposite approach is possible: using cartilage samples in combination with enzymatic digestion to learn more about the individual constituents. This approach was already used before and has proven to provide interesting insights into cartilage mechanics [21, 37, 38].

In future work not only the friction coefficient alone should be investigated but in combination with other properties. One important and also very interesting challenge will be to visualize the induced wear on the cartilage surface after friction force experiments. Therefore, tribometer experiments with higher loads (as the wear should then be more prominent) are going to be performed. After the friction measurements are completed, the induced wear on the cartilage surface will be analyzed. The effect of different lubricants and especially of viscosupplements like Sinovial® on wear protection can then be investigated.

Until now, all the experiments with articular cartilage were performed at room temperature. In the body, however, cartilage needs to function properly at a physiological temperature of

37°C. Given that it is possible to control the temperature of the solution during an AFM experiment, AFM-based friction force microscopy and also imaging can be used to determine the temperature dependence of cartilage structure and lubrication.

Appendix

A1. Synthesis of polymers

Synthesis and characterization of PI and PI-g-PS

The protocol was developed and the synthesis conducted by Markus Gallei and Matthias Rehahn, TU Darmstadt.

All the chemicals and solvents were purchased from Acros, Aldrich or Strem chemical companies. To purify isoprene, styrene and propylene sulfide a 3-fold distillation over calcium hydride was used. Before using the monomers, they were freshly distilled from those solutions. After titration with *n*-butyllithium (*n*-BuLi), 1,1-Diphenylethylene (DPE) was freshly distilled from the deeply red solution. Methyldichlorosilane was degassed and distilled over calcium hydride. Tetrahydrofuran (THF), toluene and cyclohexane (CH) were dried and deoxygenated using standard procedures. The deuterated solvents were purchased from Deutero GmbH, Kastellaun, Germany.

The synthesis were performed under an atmosphere of purified nitrogen or argon, using Schlenk technique or a glove box equipped with a Coldwell apparatus. With a Bruker ARX 300 NMR spectrometer working at 300 MHz (^{1}H NMR) the NMR spectra were recorded. Standard size exclusion chromatography (SEC) was performed at 30°C on a Mixed Gel column set from PL (PL Mixed Gel B, PL Mixed Gel C, PL Mixed Gel D) or an SDV column set from PSS (SDV 1000, SDV 100000, SDV 1000000) with THF as the mobile phase (flow rate 1ml/min). Calibration was done with polystyrene calibration standards (PS; from Polymer Standard Service (PSS), Mainz).

(End)functionalized poly(isoprene-b-propylene sulfide): 1.85g neat isoprene was dissolved in 45ml dry THF in an ampoule in a glove box. Afterward 11µl of a 1.42M *sec*-BuLi solution was added quickly via a syringe at room temperature. To ensure complete conversion the mixture was stirred for 24h at room temperature. Before cooling the solution to -18°C a sample was taken for SEC measurements. 180mg of freshly distilled propylene sulfide was added and the solution was stirred for 30min. To terminate the reaction degassed methanol was added. The polymer sample was then precipitated in methanol, filtered and dried *in vacuo*. The polymer solution was dried *in vacuo*. The polymer was stored at -15°C under argon atmosphere in a refrigerator. Using ^{1}H NMR spectroscopy the content of 1,2-poly(isoprene) was determined to be 22%. SEC measurements reveal that M_n = 119 200 g/mol and M_w = 135 700 g/mol with a polydispersity index (PDI) of 1.13.

Hydrosilylation of poly(isoprene-b-propylene sulfide): The previously synthesized block copolymer was then dissolved in dry toluene (30ml) in an ampoule in a glove box. After the addition of 227µl methyldichlorosilane, a 250µl of a Karstedt catalyst solution (2wt% in xylene) was added via a syringe at room temperature. The mixture was stirred for 72h at room temperature. By using high vacuum for 48h the solvents and possible residual silane were evaporated.

Synthesis of Poly((isoprene-block- propylene sulfide)-graft-styrene): By anionic polymerization of styrene in cyclohexane living poly(styryl) carbanions were prepared. *Sec*-butyl lithium (1.42 M) was used as a initiator [56]. PS(3 kDa) (Mn=3 000 g/mol, Mw=3300 g/mol, PDI=1.1), PS(14 kDa) (Mn=14 300 g/mol, Mw= 14 500 g/mol, PDI=1.01) and PS(88 kDa) (Mn=87 800 g/mol, Mw= 88 900 g/mol, PDI=1.01) were prepared.
The chlorosilane-functionalized PI was treated with the active PS macro anions PS(3), PS(14) and PS(88) and stirred for 48h inside the glove box. The polymer solutions were precipitated in methanol, filtered and dried *in vacuo*. For all samples, no RI signal in SEC measurements for the PI precursor was detected. The molar masses of the grafted polymers were:

- for PI-*g*-PS(3): M_n=552 600 g/mol, M_w=887 100 g/mol and PDI=1.60
- for PI-*g*-PS(14): M_n=1 009 200 g/mol, M_w= 1 595 600 g/mol and PDI=1.58
- and for PI-*g*-PS(88): M_n=1 101 000 g/mol, M_w= 1 188 700 g/mol with a PDI=1.07

Synthesis of the dendronized polymer
The synthesis was performed by Hao Yu, Baozhong Zhang and A. Dieter Schlüter, ETH Zurich.

First, the polymer *de***PG4** (DP_n~500, PDI~2, coverage~99%) and the active ester **4** were synthesized according to literature (Figure 51) [113, 114].
Active ester **4** (260mg, 0.96mmol) was added at room temperature to a solution of *de***PG4** (113mg, 0.020mmol), triethylamine (64mg, 0.6mmol) and DMAP (12mg) in DMF (3ml). The mixture was stirred for 10d. Then more active ester **4** (87mg, 0.32mmol) was added and the mixture was stirred for another 10d. Afterward a final portion of active ester **4** (87mg, 0.32mmol) was added and the stirring was continued for another 10d. The solvent was removed *in vacuo* and the residue was purified by column chromatography (SiO_2, CH_2Cl_2). The product was lyophilized from 1,4-dioxane to yield **1** as a white powder (81mg, 64%). ^{1}H NMR (500MHz, 353K, DMSO-d_6): 1.26 (br, 144 H, ^{t}Bu), 1.73 (br, 47 H, $OCH_2CH_2CH_2NH$), 2.30 (br, 60 H, $COCH_2CH_2CO$), 3.12 (br, 35 H, $NHCH_2$), 3.84 (br, 39 H, OCH_2), 6.44 (br, 12 H, PhCONH), 6.87 (br, 22 H, Ph), 7.50 (br, 17 H, CH_2CONH). GPC: M_n~3.3×10^6, M_w~7.0×10^6, PDI~2.1.

Deprotection and basification: To the powder-like product of dendronized polymer **1** (6mg, 0.001mmol) trifluoroacetic acid (2ml) was added dropwise during stirring at 0°C. The reaction mixture was warmed to room temperature and stirred for another 18h. Methanol (4ml) was used to quench the reaction and a precipitation was formed. This precipitate was collected by centrifugation, washed with water (3×10ml) and dried under vacuum to yield an off-white powder of dendronized polymer **2** (4mg, 80%). This dendronized polymer **2** was then dissolved in 10% ammonia (1ml). The solvent was removed by lyophilization and the white powder of the dendronized polymer **3** (4mg, 100%) was collected. ^{1}H NMR (500MHz, 353K, D_2O: DMSO-d_6 (1:1)): 1.69 (br, 47 H, $OCH_2CH_2CH_2NH$), 2.27 (br, 29 H, $COCH_2CH_2CO$), 3.04 (br, 55 H, $NHCH_2$), 6.38 (br, 69 H, NH), 6.74 (br, 60 H, Ph).

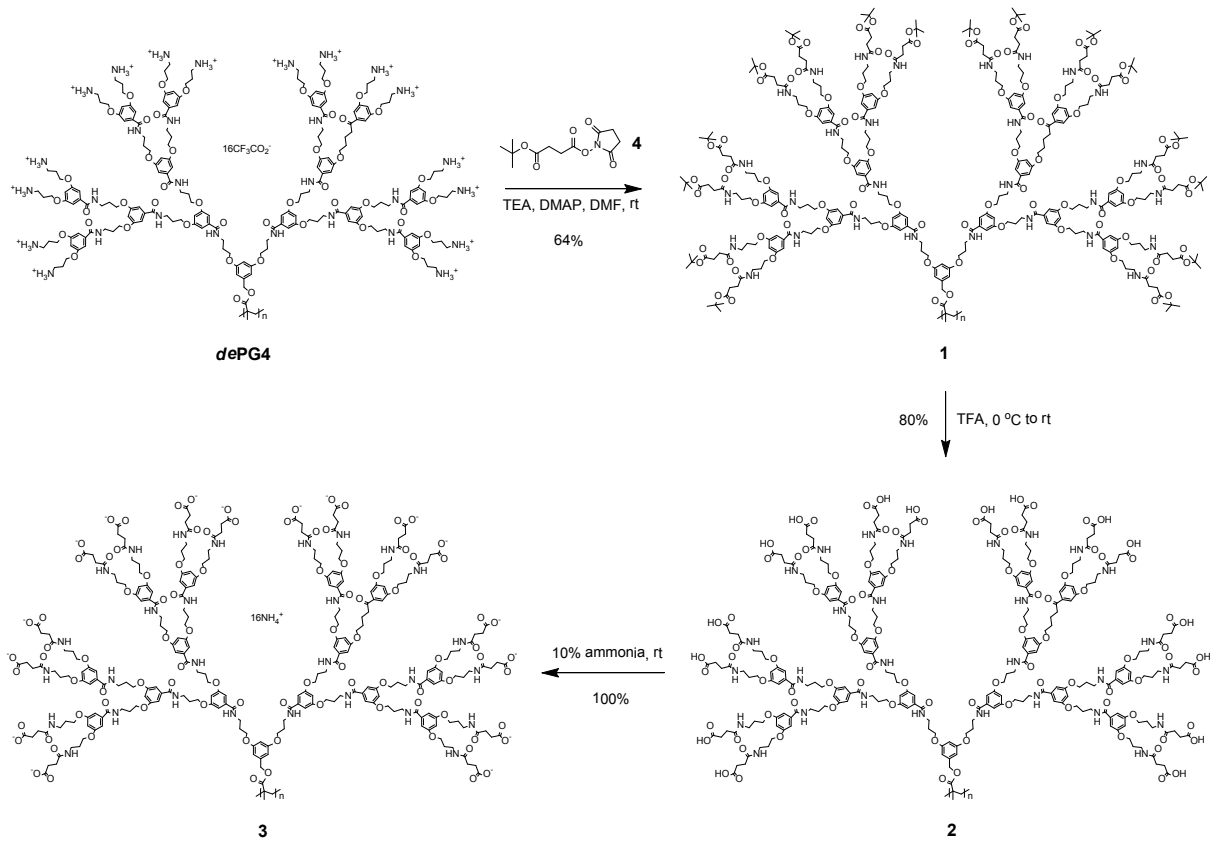

Figure 51. Schematics of the synthesis of the dendronized polymer **1**, **2** and **3** with the active ester **4**.

A2. Functionalization of the AFM tip

Before performing a single molecule force spectroscopy (SMFS) experiment or a single molecule friction force microscopy (SM-FFM) experiment, the polymer of interest has to be coupled covalently to the AFM tip. A schematic of the coupling process can be seen in Figure 11. Either polymers with an amino, a thiol or a carboxyl end group are used.

- Polymers with an amino end group:
  - Poly-L-lysine (PLL, 70-150 kDa, Sigma-Aldrich, Germany)
  - Poly-D-tyrosine (PDT, 40-100kDa, Sigma-Aldrich, Germany)
  - Aggrecan (from bovine articular cartilage, Sigma-Aldrich, Germany)
- Polymers with a thiol end group:
  - Polyisoprene (PI, synthesis is described above)
  - Polyisoprene (PI) grafted with polystyrene (PS) side chains of different molecular weight (PI-*g*-PS(3), PI-*g*-PS(14), PI-*g*-PS(88), the value in brackets corresponds to the molecular weight of PS, synthesis is described above)
  - DNA (synthesis is described in A3)
- Polymers with a carboxyl group:
  - Chondroitin sulfate sodium salt (from shark cartilage, Sigma-Aldrich, Germany)
  - Dendronized polymer (synthesis is described above)

The functionalization of the different polymers is conducted using the following protocol:

- Activation of the cantilevers (MLCT, Bruker Probe, Camarillo, CA) in a plasma chamber (Femto, Diener, Germany) with oxygen (0.26mbar, 20% power) for 15min
- Rinsing the cantilevers in acetone (anhydrous, ≥ 99.8%, VWR)
- Incubation for about 10min in a mixture of 5ml acetone and 100µl Vectabond™ (Axxora, Lörrach, Germany)

The following part of the protocol is adjusted due to the available binding sites of the different polymers.

Coupling via an amino group:

- During the incubation in Vectabond™:
  Preparation of a 1:1500 mixture of CH_3O-PEG-NHS (5kDa, Rapp Polymere, Tübingen, Germany) and PEG-α-ω-Di-NHS (6kDa, Rapp Polymere, Tübingen, Germany). Both solvated in chloroform (anhydrous, ≥99%, Sigma Aldrich).
- Rinsing in acetone and chloroform
- Incubating for 45min in the PEG solution.
- During the incubation in PEG:
  Preparation of the polymer solution:
  - Poly-L-lysine: solvated with a concentration of about 2mg/ml in borate buffer (1:19 mixture of 50mM boric acid and 50mM borax, pH 8-8.5)
  - Poly-D-tyrosine: solvated with a concentration of about 2mg/ml in 1M sodium hydroxide before exchanging the solvent with Zeba™ Desalt Spin Columns (Thermo Fisher Scientific Inc., Rockford, USA) to borate buffer
  - Aggrecan: solvated with a concentration of about 2mg/ml in borate buffer (1:19 mixture of 50mM boric acid and 50mM borax, pH 8-8.5)
- Rinsing in chloroform, in ethanol (absolute, >99.9%, Merck) and in borate buffer
- Incubation for at least 1h in the polymer solution
- Rinsing in borate buffer and ultrapure water (Biochrom, Germany) and in case of aggrecan in PBS (phosphate buffered saline, Sigma-Aldrich, Germany)
- For PLL and PDT: Collection of the excessive amount of fluid on the cantilever with a wipe and storing the cantilevers until usage in air in a clean petri dish
- For aggrecan: storing the cantilevers until usage in PBS in a clean petri dish

Coupling via a thiol group:

- During the incubation in Vectabond™:
  Preparation of a 1:1500 mixture of CH_3O-PEG-NHS (5kDa, Rapp Polymere, Tübingen, Germany) and α-Maleinimidohexanoic-ω-NHS-PEG (5kDa, Rapp Polymere, Tübingen, Germany). Both solvated in chloroform (anhydrous, ≥99%, Sigma Aldrich).
- Rinsing in acetone and chloroform
- Incubating for 45min in the PEG solution.
- During the incubation in PEG:
  Preparation of the polymer solution:

  - Polyisoprene: solvated with a concentration of about 2mg/ml in chloroform
  - PI-*g*-PS: solvated with a concentration of about 2-8mg/ml in chloroform
  - DNA: solvated with a concentration of several nM in borate buffer (1:19 mixture of 50mM boric acid and 50mM borax, pH 8-8.5)
- Rinsing in chloroform and in case of DNA also in ethanol and in borate buffer
- Incubation for at least 1h in the polymer solution
- Rinsing in chloroform or in case of DNA with borate buffer and ultrapure water (Biochrom, Germany),
- Storing the cantilevers until usage in chloroform (PI and PI-*g*-PS) or ultrapure water (DNA) in a clean petri dish

Coupling via a carboxyl group:

- During the incubation in Vectabond™:
  - Dissolving the polymers with a concentration of about 0.5-2mg/ml dependent on the solubility in either PBS (chondroitin sulfate) or methanol (anhydrous, 99.8%, Sigma-Aldrich, Germany, dendronized polymer)
  - Addition of 50µM 1-Ethyl-3-[3-dimethylaminopropyl]carbodiimide hydrochloride (EDC, Thermo Scientific, Rockford, Illinois) and 150µM *N*-hydroxysulfosuccinimide (Sulfo-NHS, Thermo Scientific, Rockford, Illinois)
- Incubation in the polymer solution for at least 1h
- Rinsing with PBS (chondroitin sulfate) or methanol (dendronized polymer)
- Storing the cantilevers until usage in PBS (chondroitin sulfate) or methanol (dendronized polymer) in a clean petri dish

For all steps described here, either autoclaved Eppendorf tubes or glass bowls are used. The glass is cleaned prior to the functionalization process using the following protocol:

- 1h in 2% Hellmanex (Hellma GmbH und Co. KG, Germany) in an ultrasonic bath
- Changing the solution to purified water and sonicate twice for 1h
- Rinsing with purified water
- 20min at 70°C in RCA (5:1:1 mixture of H_2O, H_2O_2, NH_3)
- Rinsing with purified water
- Drying in the oven

A3. Distribution of the detachment lengths

Most of the experiments on single polymer desorption focused on the evaluation of the plateau force and not the detachment length. The main reason is the broad distribution of detachment lengths during one set of experiments. Distributions measured with for example graft polymers are shown in Figure 34B. Although the same cantilever was used within an experimental set, a polymer which is attached to the tip is often lost and another one, with a different length, interacts with the surface. This makes it difficult to identify variations in the detachment length caused by for example a temperature or solvent change.
Polymers like poly-L-lysine (PLL) and poly-D-tyrosine (PDT) were bought from Sigma-

Aldrich. This is very convenient, but the drawback is the broad size distribution, namely 70-150kDa for PLL and 40-100kDa for PDT. This could then also lead to a broad distribution of detachment lengths as several polymers with different molecular weights could be bound to one AFM tip and interact in an alternate manner with the surface.
One approach to get rid of this problem was to use polymers with a well defined contour length. Therefore double-stranded DNA (Lambda DNA *Bst*E II Digest) was purchased from Sigma-Aldrich. To couple the DNA to the cantilever and to get a narrow size distribution a thiol group was introduced by performing a polymerase chain reaction (PCR). The PCR was performed using the following procedure:

First, the following mixture was prepared:

- 1µl *Taq* DNA Polymerase (M0267X, New England BioLabs® Inc., Massachusetts, USA)
- 1µl Deoxynucleotide (dNTP) Solution Mix (N0447S, New England BioLabs® Inc., Massachusetts, USA)
- 2µl forward Primer (dissolved in ultrapure water at a concentration of 100µmol, 5'-modified with NH_2, Sequence: (NH_2)CAA ATC CTT CCA GAC CCA ACC, IBA GmbH, Göttingen, Germany)
- 1µl rev-Primer (dissolved in ultrapure water at a concentration of 100µmol, 5'-modified with Thiol, Sequence: (THIOL)TAC CGT CCA GCG ACA TTC TTC, IBA GmbH, Göttingen, Germany)
- 5µl ThermoPol® Buffer (M0267X, New England BioLabs® Inc., Massachusetts, USA))
- 39µl ultrapure water (Biochrom, Germany)
- 1µl Target DNA (Lambda DNA, N3013S, New England BioLabs® Inc., Massachusetts, USA))

Afterward the PCR was performed using a thermal cycler (ICycler, Bio-Rad, California, USA) and the following protocol:

- 4 min at 95°C
- 0.5min at 95°C −
- 1min at 60°C | > loop:30x
- 3min at 68°C −
- 5min at 68°C

This results in dsDNA with a thiol group as a functional group and 1098 bp. By adjusting the pH of the solution during the functionalization process, the dsDNA should only couple via the thiol group and not via e.g. amino groups to the AFM tip. Therefore, all strands attached should have the same free length.
A total of 1098 bp means that the dsDNA had a contour length of 373nm, as the rise per base pair is 0.34nm [115]. Force-distance curves with dsDNA resulted in B-S-transitions [116] and not in plateaus of constant force (Figure 52A). Therefore the cantilevers were treated (after the attachment of dsDNA) with 7M Urea at 50°C. Urea, together with temperature, causes dsDNA to melt. As only one of the two strands was covalently attached to the tip, the other one could be removed with this process. This was proved by performing force-distance curves: no B-S-transitions occurred anymore, but plateaus of constant force (Figure 52B). The contour length of the now single-stranded DNA is not as straight forward to calculate as for

dsDNA, because for the distance between two bases different values were reported. Bockelmann et al. did single molecule force experiments and reported a value of 0.475nm [117], whereas recently Chi et al. referred to a value of 0.676nm [118]. Using both values for the ssDNA used here with 1098bp leads to a contour length between 520nm and 740nm. In Figure 52C the distribution of the detachment lengths for ssDNA obtained from experiments with several cantilevers is plotted in grey.

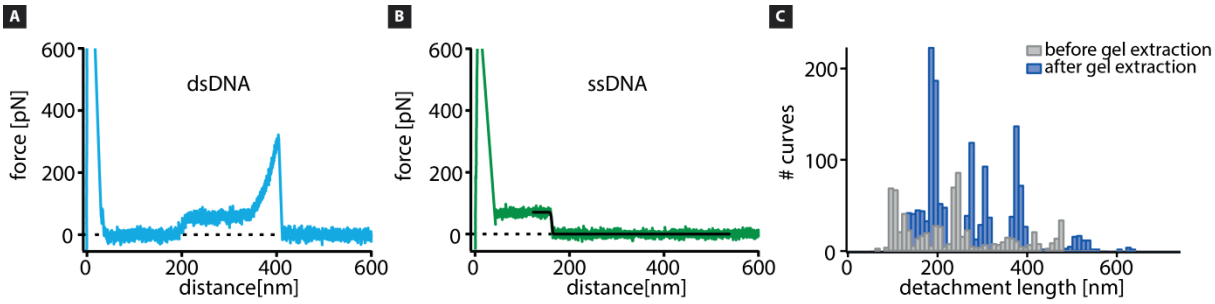

Figure 52. Typical force-distance curve obtained with (**A**) dsDNA on gold in PBS and with (**B**) ssDNA on hydrogenated diamond in water. The black solid line corresponds to a sigmoidal fit. (**C**) Distribution of the detachment lengths for ssDNA on hydrogenated diamond in water before (grey) and after gel extraction (blue).

What can nicely be seen is that the maximal detachment length is, as expected, smaller than the contour length. But still the distribution is very broad. To further narrow the weight distribution of the DNA, a sample of dsDNA was extracted from a polyacrylamide gel with the QIAquick Gel Extraction Kit (QIAGEN, Venlo, Netherlands) whereat the band visible at around 1000bp was cut out. Afterward the dsDNA was covalently attached to the cantilever tip and the cantilevers were again treated with 7M Urea at 50°C to receive ssDNA.
The distribution of the detachment lengths obtained from experiments after the gel extraction are plotted together with the detachment lengths before extraction in Figure 52C. Still, the maximal detachment length is smaller than the contour length, but the distribution could not be improved and is still very broad, although all ssDNA chains were attached at the same position of the chain to the tip and should therefore have the same free contour length.

To test that the contour length of DNA is not altered during the functionalization process or the treatment with urea, dsDNA was imaged in tapping mode in air on mica. Figure 53 shows a typical image together with the histogram of the contour lengths.

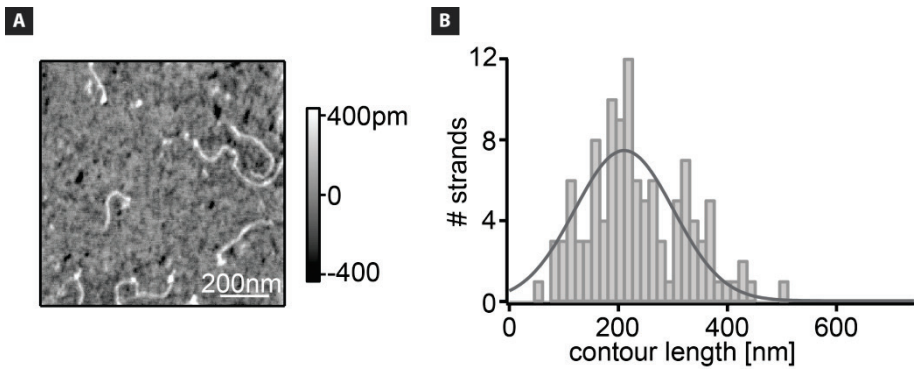

Figure 53. (**A**) Tapping mode image of dsDNA in air on mica together with (**B**) the distribution of the contour length evaluated from several images.

Here again the distribution is very broad and the majority of the strands is smaller than the contour length of 370nm. Although the DNA used for both the desorption experiments and imaging should have a very narrow size distribution, the distribution of the detachment lengths was still very large. The same was observed in measurements with polyisoprene. The polydispersity index (PDI) was determined to be 1.13. This, together with a molecular mass of 119kDa, leads to a contour length of around 650nm. The measured detachment lengths differed significantly from this value (Figure 34B). Here again the attachment to the tip is only possible via one single functional end group, namely the thiol group.
Even though it was published recently that the maximal detachment length should be on the order of 70-90% of the contour length [12], the much larger deviations observed here could not yet be explained.

A4. Influence of the dwell time on the surface

Furthermore, the influence of the dwell time on the surface was varied for measurements with ssDNA on hydrogenated diamond in water. Both, the plateau force and the detachment length were fitted with a sigmoidal curve and plotted in histograms (Figure 54).

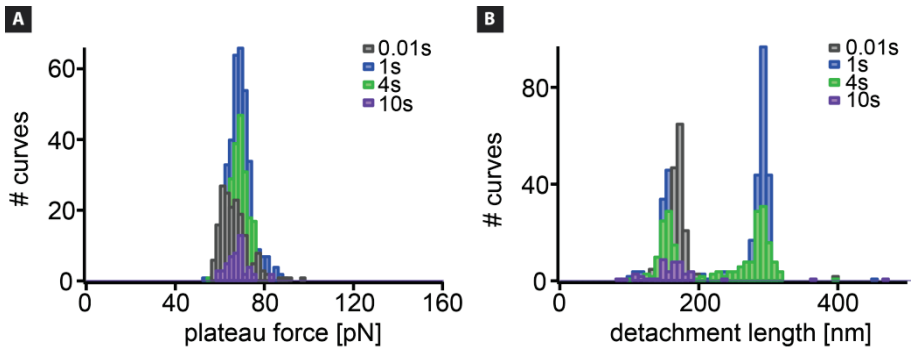

Figure 54. Dependence of (**A**) the plateau force and (**B**) the detachment length on dwell time at the surface for ssDNA on hydrogenated diamond in water.

Similar to previous results, the dwell time did neither influence the force nor the detachment length. The same behavior was observed with graft polymers (Figure 35B).

A5. Behavior of DNA during lateral movement

In addition, ssDNA was pulled laterally over different surfaces with different hydrophobicities. On a hydrophobic, hydrogenated diamond the main motif observed was desorption stick (Figure 55A, Table 6).

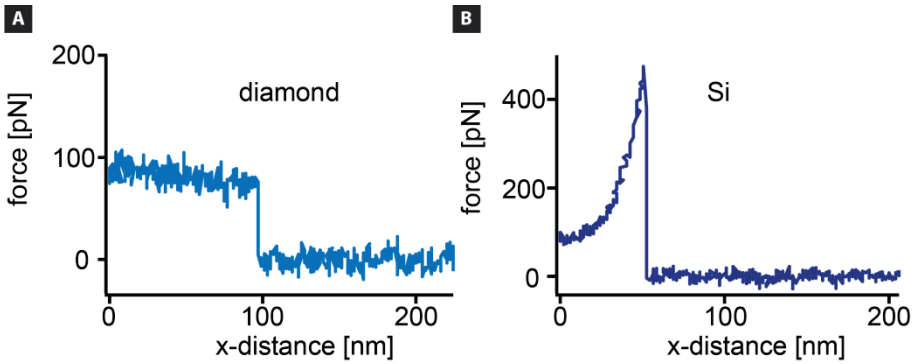

Figure 55. Motifs observed during the lateral movement of ssDNA in water. (**A**) Desorption stick occurred predominantly while measuring on hydrogenated diamond (71%), whereas (**B**) cooperative stick was the main motif observed on Si (54%).

ssDNA was not mobile on the surface, but could be desorbed in z-direction due to high internal chain dynamics. The same behavior was observed for polyisoprene and polyisoprene based graft polymers. On Si, a more hydrophilic surface, the majority of the curves resulted in cooperative stick. Less desorption stick and sliding was observed (Figure 55B, Table 6). The DNA was still immobile on the surface, but now the internal chain dynamics were lowered. Detachment from the surface was most of the time only possible by rupturing the bonds between the surface and the polymer. This is caused by the formation of strong directional hydrogen bonds between the hydrophilic surface and the ssDNA [57].

	contact angle	sliding	desorption stick	cooperative stick
diamond	75°	14%	71%	15%
Si	61°	8%	37%	54%

Table 6. Contact angle of the surface together with the occurrence of sliding, desorption stick and cooperative stick during the lateral movement of ssDNA in water on hydrogenated diamond and Si.

A6. Temperature dependent single polymer friction

Another interesting question is if the solution temperature affects the behavior of a polymer during lateral movement across a surface. As already described in chapter 4, vertical pulling is not influenced by a temperature change. This is due to a leveling off of the different contributions (polymer, water, surface) to the free energy [19]. Here, PI-*g*-PS(3), PI-*g*-PS(14) and ssDNA were chosen as polymers. The surface was a hydrogenated diamond with water as a solvent. In Figure 56 the plateau forces obtained from vertical pulling as well as the detachment forces for lateral pulling experiments are plotted for different temperatures for measurements with the graft polymers. The detachment force corresponds to the force at the x-distance where the polymer detached from the surface.

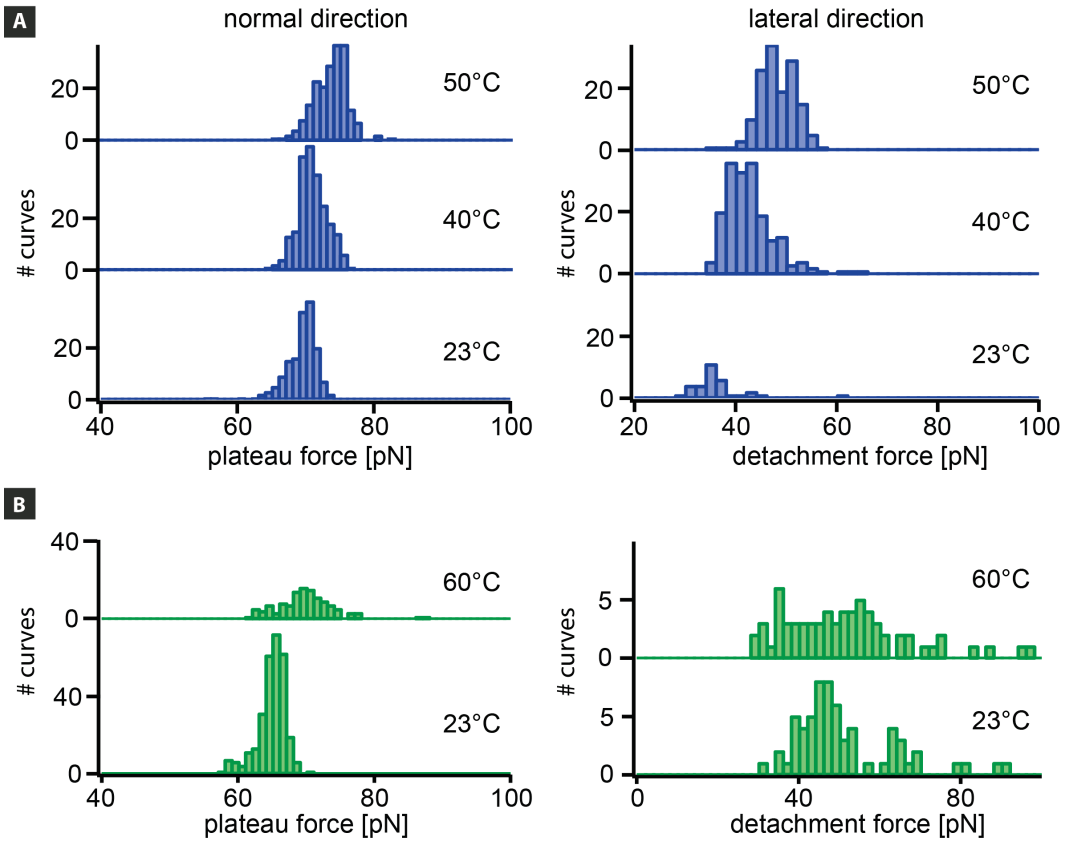

Figure 56. Temperature dependent desorption in normal and lateral direction for (**A**) PI-*g*-PS(3) and (**B**) PI-*g*-PS(14). Histograms of the plateau forces are shown for desorption in the vertical direction and histograms of the force at the point of detachment (detachment force) for pulling the polymer laterally over the surface.

For PI-*g*-PS(3) (Figure 56A) the plateau force remained constant whereas the detachment force increased. For PI-*g*-PS(14) (Figure 56B) no dependence of both the plateau and the detachment force on temperature was visible. The same holds true for ssDNA. This needs further investigation to clarify the temperature dependence of the detachment force. During the lateral movement of the polymers desorption stick is the dominating motif at all temperatures (Table 7).

	temperature	sliding	desorption stick	cooperative stick
PI-*g*-PS(3)	23°C	16.1%	67.1%	16.8%
	40°C	2.6%	96.9%	0.5%
	50°C	2.0%	98.0%	0.0%
PI-*g*-PS(14)	23°C	12.1%	83.3%	1.6%
	60°C	5.8%	91.3%	2.9%
ssDNA	23°C	20.6%	79.4%	0.0%
	40°C	17.6%	82.4%	0.0%

Table 7. Occurrence of sliding, desorption stick and cooperative stick at different temperatures for the graft polymers PI-*g*-PS(3) and PI-*g*-PS(14) and for ssDNA. The measurements were performed on hydrogenated diamond in water.

With increasing temperature the fraction of desorption stick was further increased, while sliding occurred less frequent. This means that the polymers were less mobile on the surface with increasing temperature. At the same time, however, the internal chain dynamics increased.

A7. Dependence of aggrecan adhesion on salt concentration

Aggrecan is highly negatively charged at physiological conditions due to the large amount of GAGs as side chains [61]. Therefore, the salt concentration was changed to see if the interaction with the surface was altered. As surfaces a hydrogenated diamond and a cartilage sample were chosen. Diamond is not charged, whereas cartilage is negatively charged. These two surfaces allow to investigate how salt concentration affects the interaction of aggrecan with an uncharged surface, but also how changing the salt concentration influences the interaction of a charged bottle-brush with a equally charged surface. The results can be seen in Figure 57.

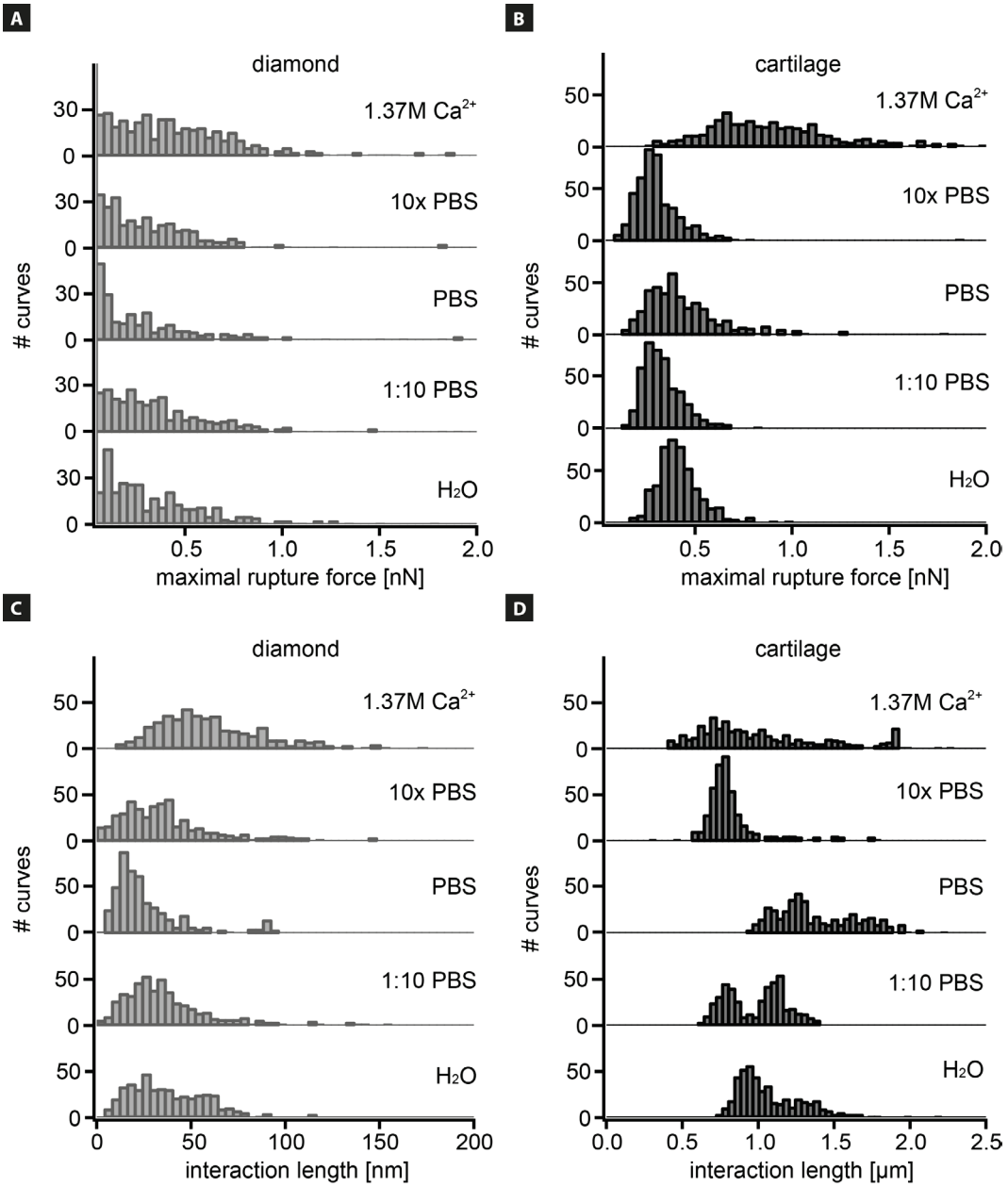

Figure 57. Dependence of the maximal rupture force for desorption measurements with aggrecan in different salt concentrations (**A**) on hydrogenated diamond and (**B**) on cartilage. The interaction length was determined for different salt concentrations (**C**) on both diamond and (**D**) on cartilage. All measurements were performed with the same cantilever.

No clear dependence on salt concentration for the maximal rupture force and the interaction length was observed. For measurements on diamond, the maximal rupture force and the interaction length are almost similar for all concentrations. For cartilage, there are slight deviations in between the measurements, but they could, especially for divalent ions like Ca^{2+}, not be reproduced reliably. Here, more experiments are needed to resolve the details of the salt dependent interactions.

A8. Persistence length of polymers with different architecture

Measuring with chondroitin sulfate, aggrecan or dendronized polymers resulted mostly in rupture events. In chapter 5 the focus is on the dependence of the maximal rupture force on the addition of side chains and their architecture. It is also possible to extract further information by fitting the rupture peaks with a worm-like chain (WLC) model [11]. The fit parameters are the persistence length p and the contour length L. Typical force-distance curves for chondroitin sulfate, aggrecan and the dendronized polymer are plotted together with the WLC-fit (black) in Figure 58.

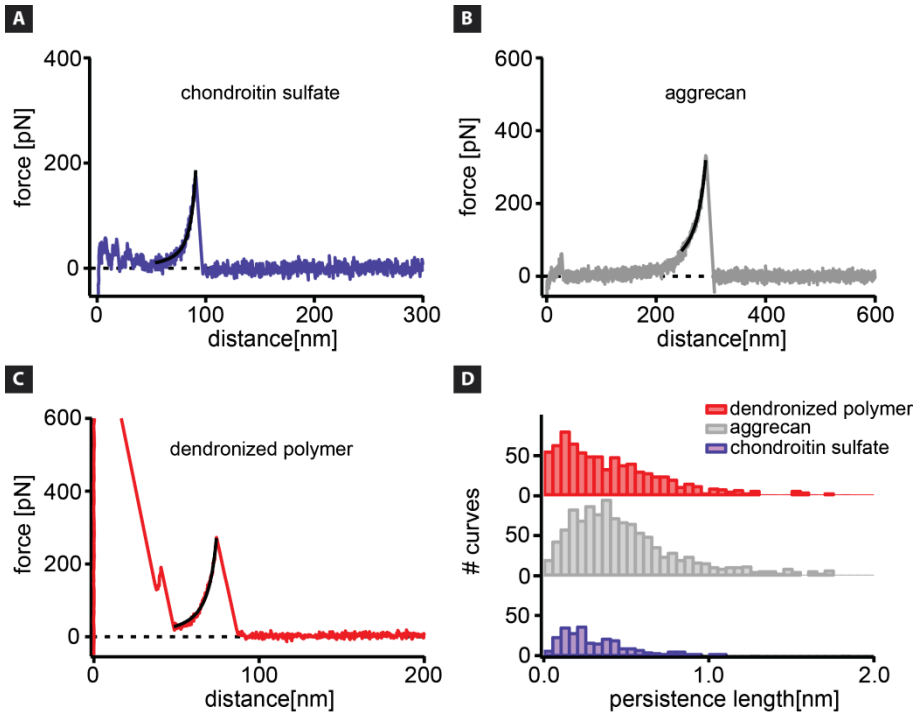

Figure 58. Typical force-distance curve with a rupture event and the corresponding WLC-fit in black for (**A**) chondroitin sulfate (p=5.7Å), (**B**) aggrecan (p=2.7Å) and (**C**) dendronized polymer (p=2.5Å). (**D**) The fitted persistence lengths p were plotted in a histogram. For the dendronized polymer 785 peaks were evaluated, for aggrecan 1095 peaks and for chondroitin sulfate 263 peaks.

The results for the persistence length are plotted in histograms (Figure 58D). The values for the dendronized polymer fit quite well with values from literature on dendronized polymers of generation four with amino end groups (4Å at low ionic strength) [119]. For aggrecan different values were reported. The evaluation of AFM images of aggrecan and chondroitin sulfate led to much larger values ranging between 82 and 110nm and 14 and 21nm for aggrecan and chondroitin sulfate, respectively [120]. The persistence length of aggrecan was

also determined from force-distance curves with aggrecan being both the probe and the surface to be 3.1Å [121]. These values are close to the ones reported here. For chondroitin sulfate no additional published values could be found.

A9. Dendronized polymers in a good solvent

As water is not a good solvent for dendronized polymers, different amounts of methanol were added to the solution and the maximal rupture force and the persistence length were determined (Figure 59).

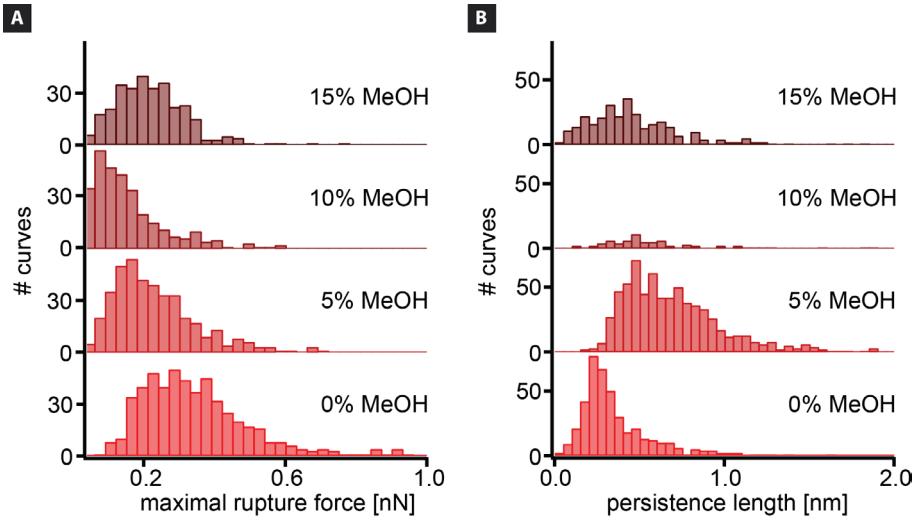

Figure 59. (**A**) Maximal rupture force and (**B**) fitted persistence length for measurements with a dendronized polymer on hydrogenated diamond in different concentrations of methanol (MeOH).

Measuring in 5% methanol slightly shifts the maximal rupture force to lower values. Higher amounts of methanol had no additional effect on the force. The same holds true for the persistence length. The persistence lengths for measurements in methanol, no matter how high the concentration was, increased slightly to higher values compared to measurements in water. This might be attributed to a lower solvation energy of the dendronized polymer in methanol compared to just water. Detachment of the polymer from the surface was facilitated by the addition of methanol to the solution and consequently the maximal rupture force decreased.

Bibliography

1. Arias, E., *United States life tables, 2007.* National vital statistics reports : from the Centers for Disease Control and Prevention, National Center for Health Statistics, National Vital Statistics System, 2011. **59**(9): p. 1-60.
2. Hayflick, L., *The future of ageing.* Nature, 2000. **408**(6809): p. 267-269.
3. Reynaud, E., *Protein Misfolding and Degenerative Diseases.* Nature Education, 2010. **3**(9).
4. Athanasiou, K.A., et al., *Articular Cartilage*. first ed2013: CRC Press.
5. Israelachvili, J., *Intermolecular and Surface Forces*. third ed2011: Elsevier.
6. Kauzmann, W., *Some factors in the interpretation of protein denaturation.* Advances in protein chemistry, 1959. **14**: p. 1-63.
7. Scherer A., et al., *Intermolecular Interaction of Polymer Molecules Determined by Single-molecule force spectroscopy.* Macromolecules, 2005. **38**(23): p. 9821-9825.
8. Schwaderer, P., et al., *Single-molecule measurement of the strength of a siloxane bond.* Langmuir : the ACS journal of surfaces and colloids, 2008. **24**(4): p. 1343-1349.
9. Strunz, T., et al., *Dynamic force spectroscopy of single DNA molecules.* Proceedings of the National Academy of Sciences of the United States of America, 1999. **96**(20): p. 11277-11282.
10. Rubinstein, M. and R.H. Colby, *Polymer Physics*2012, New York: Oxford University Press Inc.
11. Marko, J.F. and E.D. Siggia, *Stretching DNA.* Macromolecules, 1995. **28**(26): p. 8759-8770.
12. Krysiak, S., et al., *Peptide Desorption Kinetics from Single Molecule Force Spectroscopy Studies.* Journal of the American Chemical Society, 2014. **136**(2): p. 688-697.
13. Kienle, S., et al., *Measuring the interaction between ions, biopolymers and interfaces – one polymer at a time* Faraday Discussions, 2013. **160**(0): p. 329-340.
14. Pirzer, T. and T. Hugel, *Adsorption mechanism of polypeptides and their location at hydrophobic interfaces.* Chemphyschem : a European journal of chemical physics and physical chemistry, 2009. **10**(16): p. 2795-2799.
15. Schwierz, N., et al., *On the Relationship between Peptide Adsorption Resistance and Surface Contact Angle: A Combined Experimental and Simulation Single-Molecule Study.* Journal of the American Chemical Society, 2012. **134**(48): p. 19628-19638.
16. Geisler, M., R.R. Netz, and T. Hugel, *Pulling a single polymer molecule off a substrate reveals the binding thermodynamics of cosolutes.* Angewandte Chemie, 2010. **49**(28): p. 4730-4733.
17. Pirzer, T., et al., *Single molecule force measurements delineate salt, pH and surface effects on biopolymer adhesion.* Physical biology, 2009. **6**(2): p. 025004.
18. Horinek, D., et al., *Peptide adsorption on a hydrophobic surface results from an interplay of solvation, surface, and intrapeptide forces.* Proceedings of the National Academy of Sciences of the United States of America, 2008. **105**(8): p. 2842-2847.
19. Kienle, S., et al., *The Effect of Temperature on Single-Polypeptide Adsorption.* Chemphyschem : a European journal of chemical physics and physical chemistry, 2012. **13**(4): p. 982-989.
20. Zeng, H., ed. *Polymer Adhesion, Friction, and Lubrication*. 2013, John Wiley & Sons, Inc.
21. Lee, D.W., X. Banquy, and J.N. Israelachvili, *Stick-slip friction and wear of articular joints.* Proceedings of the National Academy of Sciences of the United States of America, 2013. **110**(7): p. E567-E574.
22. Berman, A.D., W.A. Ducker, and J.N. Israelachvili, *Origin and characterization of different stick-slip friction mechanisms.* Langmuir : the ACS journal of surfaces and colloids, 1996. **12**(19): p. 4559-4563.
23. Thompson, P.A. and M.O. Robbins, *Origin of stick-slip motion in boundary lubrication.* Science, 1990. **250**(4982): p. 792-794.
24. Raviv, U., et al., *Lubrication by charged polymers.* Nature, 2003. **425**(6954): p. 163-165.

25. Koo, S. and T.P. Andriacchi, *A comparison of the influence of global functional loads vs. local contact anatomy on articular cartilage thickness at the knee.* Journal of biomechanics, 2007. **40**(13): p. 2961-2966.
26. Mow, V.C., A. Ratcliffe, and A.R. Poole, *Cartilage and Diarthrodial Joints as Paradigms for Hierarchical Materials and Structures.* Biomaterials, 1992. **13**(2): p. 67-97.
27. Youn, I., et al., *Zonal variations in the three-dimensional morphology of the chondron measured in situ using confocal microscopy.* Osteoarthritis and Cartilage, 2006. **14**(9): p. 889-897.
28. Darling, E.M., S. Zauscher, and F. Guilak, *Viscoelastic properties of zonal articular chondrocytes measured by atomic force microscopy.* Osteoarthritis and Cartilage, 2006. **14**(6): p. 571-579.
29. Grodzinsky, A.J., et al., *Cartilage tissue remodeling in response to mechanical forces.* Annual review of biomedical engineering, 2000. **2**: p. 691-713.
30. Hulmes, D.J. and A. Miller, *Quasi-hexagonal molecular packing in collagen fibrils.* Nature, 1979. **282**(5741): p. 878-880.
31. Jeffery, A.K., et al., *Three-dimensional collagen architecture in bovine articular cartilage.* The Journal of bone and joint surgery. British volume, 1991. **73**(5): p. 795-801.
32. O'Hara, B.P., J.P. Urban, and A. Maroudas, *Influence of cyclic loading on the nutrition of articular cartilage.* Annals of the rheumatic diseases, 1990. **49**(7): p. 536-539.
33. Neu, C.P., K. Komvopoulos, and A.H. Reddi, *The interface of functional biotribology and regenerative medicine in synovial joints.* Tissue engineering. Part B, Reviews, 2008. **14**(3): p. 235-247.
34. Hills, B.A., *Boundary lubrication in vivo.* Proceedings of the Institution of Mechanical Engineers. Part H, Journal of engineering in medicine, 2000. **214**(1): p. 83-94.
35. Bonnevie, E.D., et al., *In-situ studies of cartilage microtribology: roles of speed and contact area.* Tribology Letters, 2011. **41**(1): p. 83-95.
36. Ateshian, G.A., *The role of interstitial fluid pressurization in articular cartilage lubrication.* Journal of biomechanics, 2009. **42**(9): p. 1163-1176.
37. Basalo, I.M., et al., *Chondroitin sulfate reduces the friction coefficient of articular cartilage.* Journal of biomechanics, 2007. **40**(8): p. 1847-1854.
38. Kumar, P., et al., *Role of uppermost superficial surface layer of articular cartilage in the lubrication mechanism of joints.* Journal of anatomy, 2001. **199**(Pt 3): p. 241-250.
39. Caligaris, M. and G.A. Ateshian, *Effects of sustained interstitial fluid pressurization under migrating contact area, and boundary lubrication by synovial fluid, on cartilage friction.* Osteoarthritis and cartilage, 2008. **16**(10): p. 1220-1227.
40. Soltz, M.A. and G.A. Ateshian, *Experimental verification and theoretical prediction of cartilage interstitial fluid pressurization at an impermeable contact interface in confined compression.* Journal of biomechanics, 1998. **31**(10): p. 927-934.
41. Mow, V.C., M.H. Holmes, and W.M. Lai, *Fluid transport and mechanical properties of articular cartilage: a review.* Journal of biomechanics, 1984. **17**(5): p. 377-394.
42. Park, S., K.D. Costa, and G.A. Ateshian, *Microscale frictional response of bovine articular cartilage from atomic force microscopy.* Journal of biomechanics, 2004. **37**(11): p. 1679-1687.
43. Mow, V.C., et al., *Biphasic creep and stress relaxation of articular cartilage in compression? Theory and experiments.* Journal of biomechanical engineering, 1980. **102**(1): p. 73-84.
44. Chan, S.M., et al., *Atomic force microscope investigation of the boundary-lubricant layer in articular cartilage.* Osteoarthritis and cartilage, 2010. **18**(7): p. 956-963.
45. Waller, K.A., et al., *Role of lubricin and boundary lubrication in the prevention of chondrocyte apoptosis.* Proceedings of the National Academy of Sciences of the United States of America, 2013. **110**(15): p. 5852-5857.
46. Klein, J., *Molecular mechanisms of synovial joint lubrication.* Proceedings of the Institution of Mechanical Engineers, Part J: Journal of Engineering Tribology, 2006. **220**(8): p. 691-710.
47. Schmidt, T.A., et al., *Boundary lubrication of articular cartilage: role of synovial fluid constituents.* Arthritis and Rheumatism, 2007. **56**(3): p. 882-891.
48. Schiavinato, A. and R.A. Whiteside, *Effective lubrication of articular cartilage by an amphiphilic hyaluronic acid derivative.* Clinical biomechanics, 2012. **27**(5): p. 515-519.

49. Forster, H. and J. Fisher, *The influence of loading time and lubricant on the friction of articular cartilage.* Proceedings of the Institution of Mechanical Engineers. Part H, Journal of engineering in medicine, 1996. **210**(2): p. 109-119.
50. Naka, M.H., Y. Morita, and K. Ikeuchi, *Influence of proteoglycan contents and of tissue hydration on the frictional characteristics of articular cartilage.* Proceedings of the Institution of Mechanical Engineers. Part H, Journal of engineering in medicine, 2005. **219**(3): p. 175-182.
51. Marshall, K.W., *Intra-articular hyaluronan therapy.* Current Opinion in Rheumatology, 2000. **12**(5): p. 468-474.
52. Lapčík, L., et al., *Hyaluronan: Preparation, Structure, Properties, and Applications.* Chemical Reviews, 1998. **98**(8): p. 2663-2684.
53. Pirzer, T. and T. Hugel, *Atomic force microscopy spring constant determination in viscous liquids.* The Review of scientific instruments, 2009. **80**(3): p. 035110.
54. Sader, J.E., et al., *Method for the Calibration of Atomic-Force Microscope Cantilevers.* Review of Scientific Instruments, 1995. **66**(7): p. 3789-3798.
55. Friedsam, C., et al., *Adsorption of polyacrylic acid on self-assembled monolayers investigated by single-molecule force spectroscopy.* New Journal of Physics, 2004. **6**: p. 9.
56. Balzer, B.N., et al., *Nanoscale friction mechanisms at solid-liquid interfaces.* Angewandte Chemie, 2013. **52**(25): p. 6541-6544.
57. Balzer, B.N., *Single Polymer Friction - Desorption Stick Meets Geometrical Interlock.*, in *Physik Department* 2014, Technische Universität München.
58. Li, Q., K.S. Kim, and A. Rydberg, *Lateral force calibration of an atomic force microscope with a diamagnetic levitation spring system.* Review of Scientific Instruments, 2006. **77**(6).
59. Wiegleb, L., *Kalibration eines Rasterkraftmikroskops für Reibungsmessungen*, in *Physik Department* 2011, Technical University München.
60. Roughley, P.J., *The structure and function of cartilage proteoglycans.* European cells & materials, 2006. **12**: p. 92-101.
61. Kiani, C., et al., *Structure and function of aggrecan.* Cell research, 2002. **12**(1): p. 19-32.
62. Grebikova, L., et al., *Interactions between Individual Charged Dendronized Polymers and Surfaces.* Macromolecules, 2013. **46**(9): p. 3603-3610.
63. Dankerl, M., et al., *Diamond Transistor Array for Extracellular Recording From Electrogenic Cells.* Advanced Functional Materials, 2009. **19**(18): p. 2915-2923.
64. Stalder, A.F., et al., *A snake-based approach to accurate determination of both contact points and contact angles.* Colloids and Surfaces A: Physicochemical and Engineering Aspects, 2006. **286**(1-3): p. 92-103.
65. Anfinsen, C.B., *Principles That Govern Folding of Protein Chains.* Science, 1973. **181**(4096): p. 223-230.
66. Schlierf, M. and M. Rief, *Temperature Softening of a Protein in Single-molecule Experiments.* Journal of Molecular Biology, 2005. **354**(2): p. 497-503.
67. Huang, D.M. and D. Chandler, *Temperature and length scale dependence of hydrophobic effects and their possible implications for protein folding.* Proceedings of the National Academy of Sciences of the United States of America, 2000. **97**(15): p. 8324-8327.
68. Gutin, A., et al., *Temperature dependence of the folding rate in a simple protein model: Search for a "glass" transition.* Journal of Chemical Physics, 1998. **108**(15): p. 6466-6483.
69. Oliveberg, M., Y.J. Tan, and A.R. Fersht, *Negative Activation Enthalpies in the Kinetics of Protein-Folding.* Proceedings of the National Academy of Sciences of the United States of America, 1995. **92**(19): p. 8926-8929.
70. Vugmeyster, L. and D. Ostrovsky, *Temperature dependence of fast carbonyl backbone dynamics in chicken villin headpiece subdomain.* Journal of Biomolecular Nmr, 2011. **50**(2): p. 119-127.
71. Privalov, P.L., *Cold denaturation of proteins.* Critical reviews in biochemistry and molecular biology, 1990. **25**(4): p. 281-305.
72. Dill, K.A., *Dominant forces in protein folding.* Biochemistry, 1990. **29**(31): p. 7133-7155.
73. Hummer, G., et al., *The pressure dependence of hydrophobic interactions is consistent with the observed pressure denaturation of proteins.* Proceedings of the National Academy of Sciences of the United States of America, 1998. **95**(4): p. 1552-1555.

74. Sedlmeier, F., D. Horinek, and R.R. Netz, *Entropy and enthalpy convergence of hydrophobic solvation beyond the hard-sphere limit.* The Journal of chemical physics, 2011. **134**(5): p. 055105.
75. Privalov, P.L. and N.N. Khechinashvili, *A thermodynamic approach to the problem of stabilization of globular protein structure: A calorimetric study.* Journal of Molecular Biology, 1974. **86**(3): p. 665-684.
76. Netz, R.R., *Charge regulation of weak polyelectrolytes at low- and high-dielectric-constant substrates.* Journal of Physics-Condensed Matter, 2003. **15**(1): p. S239-S244.
77. Kienle, S., et al., *Effect of Molecular Architecture on Single Polymer Adhesion.* Langmuir : the ACS journal of surfaces and colloids, 2014. **30**(15): p. 4351-4357.
78. Lee, H., et al., *Mussel-inspired surface chemistry for multifunctional coatings.* Science, 2007. **318**(5849): p. 426-430.
79. Yebra, D.M., S. Kiil, and K. Dam-Johansen, *Antifouling technology - past, present and future steps towards efficient and environmentally friendly antifouling coatings.* Progress in Organic Coatings, 2004. **50**(2): p. 75-104.
80. Lewis, A.L., *Phosphorylcholine-based polymers and their use in the prevention of biofouling.* Colloids and Surfaces B-Biointerfaces, 2000. **18**(3-4): p. 261-275.
81. Halperin, A., *Polymer brushes that resist adsorption of model proteins: Design parameters.* Langmuir : the ACS journal of surfaces and colloids, 1999. **15**(7): p. 2525-2533.
82. Balzer, B.N., et al., *Adhesion property profiles of supported thin polymer films.* ACS applied materials & interfaces, 2013. **5**(13): p. 6300-6306.
83. Banerjee, I., R.C. Pangule, and R.S. Kane, *Antifouling Coatings: Recent Developments in the Design of Surfaces That Prevent Fouling by Proteins, Bacteria, and Marine Organisms.* Advanced Materials, 2011. **23**(6): p. 690-718.
84. Müller, M., et al., *The influence of molecular architecture on the macroscopic lubrication properties of the brush-like co-polyelectrolyte poly(L-lysine)-g-poly(ethylene glycol) (PLL-g-PEG) adsorbed on oxide surfaces.* Tribology Letters, 2003. **15**(4): p. 395-405.
85. Dalsin, J.L., et al., *Protein resistance of titanium oxide surfaces modified by biologically inspired mPEG-DOPA.* Langmuir : the ACS journal of surfaces and colloids, 2005. **21**(2): p. 640-646.
86. Tomalia, D.A., A.M. Naylor, and W.A. Goddard, *Starburst Dendrimers - Molecular-Level Control of Size, Shape, Surface-Chemistry, Topology, and Flexibility from Atoms to Macroscopic Matter.* Angewandte Chemie-International Edition in English, 1990. **29**(2): p. 138-175.
87. Matsumoto, E., T. Fukuda, and Y. Miura, *Bioinert surface to protein adsorption with higher generation of dendrimer SAMs.* Colloids and surfaces. B, Biointerfaces, 2011. **84**(1): p. 280-284.
88. Benhabbour, S.R., H. Sheardown, and A. Adronov, *Protein resistance of PEG-functionalized dendronized surfaces: Effect of PEG molecular weight and dendron generation.* Macromolecules, 2008. **41**(13): p. 4817-4823.
89. Schlüter, A.D. and J.P. Rabe, *Dendronized Polymers: Synthesis, Characterization, Assembly at Interfaces, and Manipulation.* Angewandte Chemie, 2000. **39**(5): p. 864-883.
90. Geisler, M., et al., *Hydrophobic and Hofmeister effects on the adhesion of spider silk proteins onto solid substrates: An AFM-based single-molecule study.* Langmuir : the ACS journal of surfaces and colloids, 2008. **24**(4): p. 1350-1355.
91. Geisler, M., B.N. Balzer, and T. Hugel, *Polymer Adhesion at the Solid-Liquid Interface Probed by a Single-Molecule Force Sensor.* Small, 2009. **5**(24): p. 2864-2869.
92. Fetters, L.J., et al., *Packing length influence in linear polymer melts on the entanglement, critical, and reptation molecular weights.* Macromolecules, 1999. **32**(20): p. 6847-6851.
93. Sharpe, L.H., *The Interphase in Adhesion.* The Journal of Adhesion, 1972. **4**(1): p. 51-64.
94. Seifert, U., *Rupture of multiple parallel molecular bonds under dynamic loading.* Physical review letters, 2000. **84**(12): p. 2750-2753.
95. Ng, L., et al., *Individual cartilage aggrecan macromolecules and their constituent glycosaminoglycans visualized via atomic force microscopy.* Journal of Structural Biology, 2003. **143**(3): p. 242-257.

96. Han, L., et al., *Cartilage aggrecan can undergo self-adhesion.* Biophysical journal, 2008. **95**(10): p. 4862-4870.
97. Andriacchi, T.P., S. Koo, and S.F. Scanlan, *Gait mechanics influence healthy cartilage morphology and osteoarthritis of the knee.* The Journal of bone and joint surgery. American volume, 2009. **91 Suppl 1**: p. 95-101.
98. Malemud, C.J., *Changes in proteoglycans in osteoarthritis: biochemistry, ultrastructure and biosynthetic processing.* The Journal of rheumatology. Supplement, 1991. **27**: p. 60-2.
99. Setton, L.A., D.M. Elliott, and V.C. Mow, *Altered mechanics of cartilage with osteoarthritis: human osteoarthritis and an experimental model of joint degeneration.* Osteoarthritis and cartilage, 1999. **7**(1): p. 2-14.
100. Goldring, M.B., *The role of the chondrocyte in osteoarthritis.* Arthritis and Rheumatism, 2000. **43**(9): p. 1916-1926.
101. Dahl, L.B., et al., *Concentration and molecular weight of sodium hyaluronate in synovial fluid from patients with rheumatoid arthritis and other arthropathies.* Annals of the rheumatic diseases, 1985. **44**(12): p. 817-822.
102. Pelletier, J.P., J. Martel-Pelletier, and S.B. Abramson, *Osteoarthritis, an inflammatory disease: potential implication for the selection of new therapeutic targets.* Arthritis and Rheumatism, 2001. **44**(6): p. 1237-1247.
103. Felson, D.T., et al., *Osteoarthritis: new insights. Part 2: treatment approaches.* Annals of internal medicine, 2000. **133**(9): p. 726-737.
104. Gigante, A. and L. Callegari, *The role of intra-articular hyaluronan (Sinovial) in the treatment of osteoarthritis.* Rheumatology international, 2011. **31**(4): p. 427-444.
105. Lo, G.H., et al., *Intra-articular hyaluronic acid in treatment of knee osteoarthritis: a meta-analysis.* JAMA : the journal of the American Medical Association, 2003. **290**(23): p. 3115-3121.
106. Miller, L.E. and J.E. Block, *US-Approved Intra-Articular Hyaluronic Acid Injections are Safe and Effective in Patients with Knee Osteoarthritis: Systematic Review and Meta-Analysis of Randomized, Saline-Controlled Trials.* Clinical medicine insights. Arthritis and musculoskeletal disorders, 2013. **6**: p. 57-63.
107. Benz, M., N. Chen, and J. Israelachvili, *Lubrication and wear properties of grafted polyelectrolytes, hyaluronan and hylan, measured in the surface forces apparatus.* Journal of biomedical materials research. Part A, 2004. **71**(1): p. 6-15.
108. Holmes, M.W., M.T. Bayliss, and H. Muir, *Hyaluronic acid in human articular cartilage. Age-related changes in content and size.* The Biochemical journal, 1988. **250**(2): p. 435-441.
109. Ateshian, G.A., et al., *The Role of Osmotic Pressure and Tension-Compression Nonlinearity in the Frictional Response of Articular Cartilage.* Transport in Porous Media, 2003. **50**(1-2): p. 5-33.
110. Parsons, J.R. and J. Black, *Mechanical behavior of articular cartilage: Quantitative changes with alteration of ionic environment.* Journal of biomechanics, 1979. **12**(10): p. 765-773.
111. Eisenberg, S.R. and A.J. Grodzinsky, *Swelling of articular cartilage and other connective tissues: electromechanochemical forces.* Journal of orthopaedic research : official publication of the Orthopaedic Research Society, 1985. **3**(2): p. 148-159.
112. Merkher, Y., et al., *A rational human joint friction test using a human cartilage-on-cartilage arrangement.* Tribology Letters, 2006. **22**(1): p. 29-36.
113. Yu, H., A.D. Schluter, and B.Z. Zhang, *Synthesis of Dendronized Polymers by a "n+2" Approach.* Macromolecules, 2012. **45**(21): p. 8555-8560.
114. Colombo, R., et al., *Synthesis and Biological Evaluation (in Vitro and in Vivo) of Cyclic Arginine-Glycine-Aspartate (RGD) Peptidomimetic-Paclitaxel Conjugates Targeting lntegrin alpha(v)beta(3).* Journal of Medicinal Chemistry, 2012. **55**(23): p. 10460-10474.
115. Bloomfield, V.A., D.M. Crothers, and I. Tinoco JR, *Nucleic Acids - Structures, Properties, and Functions.* 2000: University Science Books.
116. Rief, M., H. Clausen-Schaumann, and H.E. Gaub, *Sequence-dependent mechanics of single DNA molecules.* Nature structural biology, 1999. **6**(4): p. 346-349.
117. Bockelmann, U., B. Essevaz-Roulet, and F. Heslot, *DNA strand separation studied by single molecule force measurements.* Physical Review E, 1998. **58**(2): p. 2386-2394.

118. Chi, Q., G. Wang, and J. Jiang, *The persistence length and length per base of single-stranded DNA obtained from fluorescence correlation spectroscopy measurements using mean field theory.* Physica A: Statistical Mechanics and its Applications, 2013. **392**(5): p. 1072-1079.
119. Popa, I., et al., *Large mechanical response of single dendronized polymers induced by ionic strength.* Angewandte Chemie, 2010. **49**(25): p. 4250-4253.
120. Ng, L., et al., *Persistence Length of Cartilage Aggrecan Macromolecules Measured via Atomic Force Microscopy.* Macromolecular Symposia, 2004. **214**(1): p. 1-4.
121. Harder, A., et al., *Single-molecule force spectroscopy of cartilage aggrecan self-adhesion.* Biophysical journal, 2010. **99**(10): p. 3498-3504.

List of publications

- Kienle S., Liese S., Schwierz N., Netz R.R. and Hugel T., *The Effect of Temperature on Single-Polypeptide Adsorption.* Chemphyschem : a European journal of chemical physics and physical chemistry, 2012. **13**(4): p. 982-989.

- Kienle S., Pirzer T., Krysiak S., Geisler M. and Hugel T., *Measuring the interaction between ions, biopolymers and interfaces – one polymer at a time.* Faraday Discussions, 2013. **160**(0): p. 329-340.

- Elbert J., Krohm F., Rüttiger C., Kienle S., Didzoleit H., Balzer B.N., Hugel T., Stühn B., Gallei M. and Brunsen A., *Polymer-Modified Mesoporous Silica Thin Films For Redox-Mediated Selective Membrane Gating*. Advanced Functional Materials, 2013. doi: 10.1002/adfm.201302304

- Kienle S., Gallei M., Yu H., Zhang B., Krysiak S., Balzer B.N., Rehahn M., Schlüter A.D. and Hugel T., *Effect of Molecular Architecture on Single Polymer Adhesion.* Langmuir, 2014. **30**(15): p. 4351-4357.

- Balzer B.N., Kienle S., Gallei M., v. Klitzing R., Rehahn M. and Hugel T., *Stick-Slip Mechanism at the Nanoscale.* submitted

- Kienle S., Böttcher K., Wiegleb L., Burgkart R., Lieleg O. and Hugel T., *From nano- to macroscopic cartilage lubrication.* in preparation

- Böttcher K., Kienle S., Wiegleb L., Winkler U., Kramer F., Burgkart R., Hugel T. and Lieleg O., *Recovery after Rehydration.* in preparation

- Balzer B.N., Geisler M., Kienle S., Krysiak S., Stetter F. and Hugel T. *AFM-based single polymer adhesion and friction sensors*. in preparation

Acknowledgements

Zu allererst möchte ich meinem Doktorvater Prof. Thorsten Hugel für die Betreuung und Unterstützung während meiner Doktorarbeit danken. Er gab mir stets die Möglichkeit meine eigenen Ideen zu verwirklichen und gab mir großen Freiraum in der Durchführung der Experimente. Gespräche mit ihm führten oft zu neuen Ideen und Anregungen. Ich bedanke mich auch für die Möglichkeit meine Arbeit auf internationalen Konferenzen vorzustellen.

Ich möchte mich aber auch bei Priv.-Doz. Dr. med. Rainer Burgkart für die Übernahme der Zweitkorrektur bedanken, für die Anleitung zur Präparation der Knorpelproben und auch für Anregungen zum LURACs-Projekt aus der Sicht eines Mediziners.

Diese Arbeit wäre ohne die gute Zusammenarbeit mit weiteren Kooperationspartner nicht möglich gewesen.
Bei Susanne Liese und Prof. Roland Netz möchte ich mich für die Durchführung der MD Simulationen bedanken.
Für die Synthese der Graft Polymere bedanke ich mich bei Dr. Markus Gallei und Prof. Matthias Rehahn von der TU Darmstadt.
Auch für die Synthese der Dendronized Polymers möchte ich mich bedanken. Sie wurde durchgeführt von Hao Yu, Dr. Baozhong Zhang und Prof. A. Dieter Schlüter von der ETH Zürich.
Andreas Reitinger danke ich für die Behandlung der Diamanten.
Ich möchte mich auch ganz herzlich bei den Kooperationspartner im LURACs Projekt bedanken: Kathrin Böttcher und Prof. Oliver Lieleg für die gute Zusammenarbeit hier am IMETUM.

Ich bedanke mich auch bei meinen anderen Kollegen hier am IMETUM (vor allem Vera) und der Gruppe E22a und hierbei besonders bei meinen Bürokolleginnen Bettina und Steffi! Vielen Dank auch für das Korrekturlesen! Aber auch meine ehemaligen Kollegen Bizan, Frank und Tobias sollen nicht unerwähnt bleiben. Ich bedanke mich auch bei meinen ehemaligen Studenten Franz Kramer und Lorenz Wiegleb für die tolle Zusammenarbeit am Knorpelprojekt.

Ich möchte mich bei meiner Familie bedanken, ohne die ich nie so weit gekommen wäre und die mich immer unterstützt haben.

Zu allerletzt möchte ich mich bei meinem Freund Harry für einfach alles bedanken. In letzter Zeit aber besonders für den Rückhalt, das Korrekturlesen und die Graphikdesign-Skills ;-)